UNIVERSITY OF OKLAHOMA

GRADUATE COLLEGE

A POLARIMETRIC AND MICROPHYSICAL INVESTIGATION OF WINTER STORMS

A DISSERTATION

SUBMITTED TO THE GRADUATE FACULTY

in partial fulfillment of the requirements for the

Degree of

DOCTOR OF PHILOSOPHY

By

ERICA MICHELLE GRIFFIN

Norman, Oklahoma

2018

A POLARIMETRIC AND MICROPHYSICAL INVESTIGATION OF WINTER STORMS

A DISSERTATION APPROVED FOR THE
SCHOOL OF METEOROLOGY

BY

Dr. Phillip Chilson, Chair

Dr. Terry Schuur

Dr. Michael Biggerstaff

Dr. Guifu Zhang

Dr. Michael Engel

Dedication

To my parents, Sherman and Karen Griffin. This dissertation is a reflection of your selfless love, commitment, and unwavering support. I never would have made it to this point without you.

Acknowledgments

I first want to express my gratitude to my advisor, Dr. Terry Schuur, who has guided me with knowledgeable advice and patience throughout my years in graduate school. I have learned so much from his exemplary leadership and am thankful for his kindness and enthusiasm and for always being available for countless meetings and insightful discussions. His encouragement and mentorship have helped me to grow as a scientist and become more independent in my thought and more confident in my oral and written communication. There are no words to fully express how truly grateful I am for the investment he has made in my life and how much I look up to him as a scientist.

I also want to thank Dr. Alexander Ryzhkov for his mentorship and support throughout the work on this dissertation. His advice and constructive feedback have been invaluable and his scientific expertise on radar polarimetry and ice microphysics has been an inspiration to me. I am truly grateful for his encouraging words and investment in my research. My committee members have also been key supporters in the completion of my doctorate: Dr. Phillip Chilson, Dr. Michael Biggerstaff, Dr. Guifu Zhang, and outside committee members Dr. Fred Shelley (prior to his recent retirement) and Dr. Michael Engel. Thank you to Dr. Chilson for his willingness to serve as the SoM chair of this committee and thank you all for providing insightful and constructive conversations, encouragement, and valuable advice throughout the years. I have learned so much from each of you and am so grateful for everything you have taught me.

I will always be thankful to Dr. Peter Lamb, who sadly passed away before culmination of this work, for believing in me and providing me the opportunity to pursue

this degree. I also thank Dr. Kelvin Droegemeier and Dr. Daphne LaDue for their valuable mentorship and advice throughout the years extending back to my senior year in high school. John Krause and Dr. Pengfei Zhang greatly contributed to the success of this dissertation through providing code and valuable assistance for generating the QVP images presented in this book. Thank you both for the enjoyable and helpful discussions and thank you to John for teaching me how to process polarimetric radar data. I am also deeply grateful to Dr. Don MacGorman and the late Dr. David Rust for their mentorship, thoughtful advice, and investment in my career. Robert Coggins, Will Agent, Jeff Horn, Steve Fletcher, and Sterling Butler are greatly appreciated for their technical support that greatly contributed to the success of this work.

Thank you to the following colleagues for their support, enjoyable discussions, collaboration, and advice: Dr. Heather Reeves, Joey Picca, Dr. Kim Elmore, Dr. Petar Bukovčić, Dr. Alex Fierro, Dr. Dušan Zrnić, Jeff Peters, Dr. Matthew Kumjian, Dr. Jacob Carlin, Dr. Katie Wilson, SaiSai Ding, Elizabeth DiGangi, Kiel Ortega, Dr. Kristin Calhoun, Dr. Pam Heinselman, Dr. Jeff Snyder, Dr. Vincent Wood, Dr. John Snow, Dr. Brian Fiedler, Dr. Petra Klein, Dr. Alan Shapiro, Dr. David Parsons, Dr. Fredrick Carr, Dr. Susan Postawko, and Dr. Mark Morrisey. I am grateful to Tracy Reinke, Dr. Greg McFarquhar, Dr. Randy Peppler, Tonia Rollins, Linda McGuckin, LeAnne Salle, Linda Crank, Christie Upchurch, Jamie Foucher, Tanya Riley, and all of the faculty and staff members throughout the building who have been extremely encouraging and supportive of me throughout the years.

Funding for this work was provided by the NOAA/Office of Oceanic and Atmospheric Research under NOAA–University of Oklahoma Cooperative Agreement NA11OAR4320072, the U.S. Department of Commerce, and by the U.S. National Weather Service, Federal Aviation Administration, and Department of Defense program for modernization of NEXRAD. Additional funding came from the National Science Foundation Grant 1143948 and the Department of Energy Grant DE-SC0008811. Total lightning data are courtesy of Earth Networks. Thank you to Dr. Stephen Cocks, Dr. Matthew Kumjian, and Dr. Valery Melnikov for providing reviews and helpful comments and suggestions for improving content in this dissertation.

I want to express my gratefulness for the prayers and tremendous loving support of my grandparents, James Kenneth and Thelma Griffin and William and Jenna Garrett, and also of my father- and mother-in- laws Drs. Michael Ross and Susan Elliott, Dr. Daniel and Sally Elliott, and of all my dear family and friends.

My parents, Sherman and Karen Griffin, have always done everything they could to support me in fulfilling my life-long dream of studying the weather. From supporting my early love for math by enrolling me in the advanced math classes I wanted to be in, to buying me weather books and instruments, to arranging my high school volunteer work at the NSSL. I am grateful for their selfless love and words of encouragement and motivation that have kept me steadfast in achieving my doctorate. My sisters, Cerissa and Krissy, have always been by my side, cheering me on, and helping me to keep sight of my goals. I thank all of them for bearing with me through each and every step of the way, for

always believing in me, and for making the journey an enjoyable one. I never would have made it to this point without them.

My husband, Matthew Elliott, has been a "rock" for me and has believed in me from day one, extending back to our undergraduate meteorology courses. He has always been there for me and provided constructive help, feedback, and advice on my work throughout the years. He has celebrated with me during the highs and encouraged and motivated me during the lows and I never would have made it to this point without him. There are no words to fully express how grateful I am for his unwavering love and support.

Above all, I thank God, the Lord and Savior Jesus Christ, who has carried me through every step of the way. When I was overwhelmed or lacked confidence, he was my strength and helped me through. Getting to this point was filled with many hills and valleys, but I have seen the faithfulness of God through it all.

"On the mountains, I will bow my life to the one who set me there. In the valley, I will lift my eyes to the one who sees me there. When I'm standing on the mountain, I didn't get there on my own. When I'm walking through the valley, I know I am not alone (Tauren Wells)."

Table of Contents

List of Tables

List of Figures

Abstract

The U.S. WSR-88D network has been upgraded to polarimetric capabilities, providing dual-polarization data for regions of the country never before sampled by polarimetric radar and allowing for an unprecedented view into the ice microphysical processes within winter precipitation. As the polarimetric data became available, a database was compiled, consisting of thousands of hours of polarimetric observations in a wide variety of winter precipitation events and exhibiting several intriguing and repetitive polarimetric signatures. Understanding what these polarimetric signatures reveal about different microphysical processes is crucial for improving their representation in numerical weather prediction models and quantitative precipitation estimation algorithms, as well as for better understanding precipitation formation and evolution throughout the depth of a cloud, ultimately improving winter weather forecasting.

This study first investigates the evolution and nature of intriguing and previously undocumented polarimetric signatures observed during the historic 8-9 February 2013 Northeast blizzard, and examines them in light of the thermodynamic environment within which they developed and the apparent microphysical processes that were active when they appeared. A more climatological and quantitative analysis is then conducted using a new quasi-vertical profile (QVP) methodology to investigate the microphysical evolution and significance of polarimetric signatures and their statistical correlations in the dendritic growth layer (DGL), at the tops of clouds, and near and within the melting layer (ML) in a selection of winter events. A statistical polarimetric model of the ML is introduced and a

new method to estimate K_{DP} in the ML is used to present the first reliable QVP statistics of K_{DP} in the ML at S band.

Chapter 1: Introduction

Winter precipitation events, particularly transitional storms and heavy snow, are difficult to accurately forecast and nowcast, largely because of poor parameterization of ice microphysical processes in numerical weather prediction (NWP) models. Transitions between precipitation types at the surface (e.g., rain, snow, and mixed-phased precipitation such as ice pellets and freezing rain) can present disruptive minor or hazardous social and economic impacts, depending on the type of precipitation reaching the ground. For example, light snow and ice pellets can produce havoc on transportation and commerce, while freezing rain and heavy snow often result in more dangerous and significant impacts including billions of dollars in property damage, devastating effects on agriculture, and injuries and fatalities (e.g., Forbes et al. 1987; Martner et al. 1992; Stewart 1992; Cortinas 2000; Changnon 2003; Cortinas et al. 2004). Therefore, providing the public and emergency managers with accurate and timely weather information can be critical to public safety and property protection. To help operational meteorologists output optimal short-term forecasts and improve the accuracy of real-time warnings of hazardous winter weather conditions (especially mixed-phase precipitation and heavy snowfall), a deeper understanding of winter precipitation physics and their temporal evolution is necessary.

Since polarimetric radars are able to distinguish precipitation types, there is great potential for future improvements in nowcasting of winter weather events (Schuur et al. 2012). Given that snow properties (e.g., aspect ratios and bulk densities) vary significantly both temporally and spatially within clouds and also that ice particles are nonspherical, polarimetry is a valuable means to estimate bulk properties of snowstorms (Ryzhkov et al.

1998). Dual-polarization U.S. Weather Surveillance Radar-1988 Doppler (WSR-88D) radars simultaneously transmit and receive horizontally- and vertically-polarized electromagnetic waves, providing an abundance of information on the physical characteristics of hydrometeors in clouds and precipitation. In addition to collecting conventional radar variables such as radar reflectivity factor at horizontal polarization (Z_H) and Doppler velocity (V_r), polarimetric radars collect differential reflectivity (Z_{DR}), the correlation coefficient (ρ_{hv}) between two co-polar radar signals, and differential propagation phase shift (Φ_{DP}). Specific differential phase (K_{DP}), which is one-half of the range derivative of Φ_{DP}, is computed from Φ_{DP}. A review of these polarimetric radar variables can be found in Kumjian (2013a) while further information on the theory and applications of weather radar polarimetry can be found in Balakrishnan and Zrnić (1990), Herzegh and Jameson (1992), Doviak and Zrnić (1993), Vivekanandan et al. (1999), Zrnić and Ryzhkov (1999), Straka et al. (2000), Schuur et al. (2003), Bringi and Chandrasekar (2001), Scharfenberg et al. (2005), and Kumjian and Ryzhkov (2008).

Since the advent of dual-polarization weather radar, many studies have demonstrated the ability of polarimetric radars to identify microphysical properties within convective storms, as well as to provide detailed information on storm structure and development. Prior to this dissertation, the majority of polarimetric radar studies focused on warm-season and severe convection analyses (e.g., Herzegh and Jameson 1992; Doviak and Zrnić 1993; Zrnić and Ryzhkov 1999; Straka et al. 2000; Ryzhkov et al. 2005; Kumjian and Ryzhkov 2008; Kumjian et al. 2010), while comparatively few studies (e.g., Hogan et al. 2002; Field et al. 2004; Kennedy and Rutledge 2011; Ryzhkov et al. 2011;

Kumjian et al. 2011; Schuur et al. 2012; Andrić et al. 2013; Bechini et al. 2013; Kumjian et al. 2013, 2014) documented polarimetric investigations of the microphysical properties of winter precipitation. With the completion of the polarimetric upgrade to the WSR-88D network in 2013, dual-polarization data are now available for observing the microphysical properties of winter precipitation in regions of the country previously un-sampled by polarimetric radar. Furthermore, since polarimetric observations of precipitation provide valuable information on the size, shape, orientation, and phase of hydrometeors (e.g., Herzegh and Jameson 1992; Doviak and Zrnić 1993; Zrnić and Ryzhkov 1999; Straka et al. 2000; Kumjian 2013a,b,c), a thorough analysis of data from the WSR-88D network promise to advance the understanding of microphysical processes and the life cycle of ice particles as they nucleate, evolve, and fall through a cloud. In turn, this will facilitate improvements in the representation of ice crystal properties including size, shape, density, and temperature dependence in future cloud microphysical models. This is important since ice crystal habits are particularly sensitive to even slight changes in thermodynamic conditions and ice supersaturation (e.g., Bailey and Hallett 2009), which can influence precipitation rates at the surface. Since understanding what polarimetric signatures reveal about different microphysical processes is crucial for improving their representation in NWP models, this dissertation focuses on investigating the temporal evolution of vertical profiles of polarimetric signatures (alongside thermodynamic output from numerical prediction models) to investigate what they indicate about the microphysics occurring throughout the depth of the cloud. The results from this analysis are also useful for improving quantitative precipitation estimation (QPE) estimates, particularly in regions

where the rainfall estimates are contaminated by mixed-phase precipitation such as when the radar's beam passes through the melting layer (ML).

As new polarimetric data became available in 2013, the author began compiling a database that consists of hundreds of events and thousands of hours of polarimetric observations in a wide variety of winter precipitation events that exhibit several intriguing and repetitive polarimetric signatures. Specifically, the database includes the following attributes: radar location, date, time period, states affected, polarimetric signatures observed [i.e., refreezing, rain-snow transition zones, downward excursions of the ML to the surface, dendritic growth layers (DGLs), depolarization streaks, ice crystals near the top of the cloud, wet snow, dry snow, and "snow flares" (Griffin et al. 2014)], as well as the type of winter system (i.e., lake-effect snow, convective, or stratiform) and whether or not lightning was associated with the event. The degree of distinctness of each of the signatures was also recorded in order to distinguish between their intensity, notability, and potential usefulness for future study. Surface precipitation type reports from Meteorological Phenomena Identification Near the Ground (mPING), National Weather Service (NWS) observers, and personal observations were also included. The analysis of these observational datasets will provide valuable insight in to the importance of polarimetry in progressing understanding of winter precipitation physics and will ultimately provide operational and research meteorologists with reliable radar indicators of winter weather that can only be observed with dual-polarization radar.

This dissertation is organized as follows: Chapter 2 presents an investigation of the historic 8-9 February 2013 Northeast Blizzard through an analysis of the polarimetric

signatures that are presented alongside thermodynamic conditions derived from numerical model output and mPING surface precipitation type observations. The study, which is the first published investigation of polarimetric and microphysical characteristics of a northeastern coastal winter storm, provides a better understanding of the fundamental microphysical processes within Northeastern winter storm systems. The signatures observed in this unusually intense event also provide motivation for the more detailed statistical examinations of the DGL and ML addressed by the remainder of the dissertation. Chapter 3 implements a new quasi-vertical profile (QVP) methodology to investigate the microphysical evolution of the DGL by examining statistical correlations between the polarimetric signatures in the DGL and cloud top temperatures for a selection of winter storms. An interpretation of the ice microphysical processes is provided. Chapter 4 presents a polarimetric technique to define the top and bottom of the ML and uses QVPs to document the polarimetric characteristics of the ML in cold-season storms. Statistical relationships are then developed to gain insight into the evolution of microphysical processes above, within, and below the ML, leading to a statistical polarimetric model of the ML. The first reliable QVP statistics of K_{DP} in MLs at S band are also presented. Lastly, Chapter 5 summarizes the findings of this dissertation, provides discussion of the overall results, and presents an outlook for future research opportunities. Note that Chapters 2 and 3 are derived from already published manuscripts and Chapter 4 is derived from a manuscript recently submitted for publication. Therefore, these chapters are formatted to include their own abstract, introduction, methodology, and summary and conclusion sections.

Chapter 2: A Polarimetric and Microphysical Investigation of the Northeast Blizzard of 8-9 February 2013

Material in this chapter is from Griffin et al. (2014).

Abstract

On 8–9 February 2013, the northeastern United States experienced a historic winter weather event ranking among the top five worst blizzards in the region. Heavy snowfall and blizzard conditions occurred from northern New Jersey, inland to New York, and northward through Maine. Storm-total snow accumulations of 30–61 cm were common, with maximum accumulations up to 102 cm and snowfall rates exceeding 15 cm h^{-1}. Dual-polarization radar measurements collected for this winter event provide valuable insights into storm microphysical processes. In this study, polarimetric data from the Weather Surveillance Radar-1988 Doppler (WSR-88D) in Upton, New York (KOKX), are investigated alongside thermodynamic analyses from the 13-km Rapid Refresh model and surface precipitation type observations from both Meteorological Phenomena Identification Near the Ground (mPING) and the National Weather Service (NWS) Forecast Office in Upton, New York, for interpretation of polarimetric signatures. The storm exhibited unique polarimetric signatures, some of which have never before been documented for a winter system. Reflectivity values were unusually large, reaching magnitudes >50 dBZ in shallow regions of heavy wet snow near the surface. The 0°C transition line was exceptionally distinct in the polarimetric imagery, providing detail that was often unmatched by the numerical model output. Other features include differential attenuation of magnitudes typical of melting hail, depolarization streaks that provide evidence of electrification,

nonuniform beamfilling, a “snow flare” signature, and localized downward excursions of the melting-layer bright band collocated with observed transitions in surface precipitation types. In agreement with previous studies, widespread elevated depositional growth layers, located at temperatures near the model-predicted -15°C isotherm, appear to be correlated with increased snowfall and large reflectivity factors Z_H near the surface.

1. Introduction

On 8–9 February 2013, a nor’easter moved up the North Atlantic coast of the United States, resulting in copious snowfall and high winds over much of the region. This historic winter weather event exhibited several distinctive polarimetric radar signatures, including exceptionally high reflectivities, differential attenuation, downward excursions of the melting layer to the surface, depositional growth layers, depolarization streaks, nonuniform beamfilling, and a “snow flare” signature. These observed polarimetric features provide valuable insights into the system’s ongoing microphysical processes. With the recent polarimetric upgrade to the U.S. Weather Surveillance Radar-1988 Doppler (WSR-88D) network, dual-polarization data are now available for locations throughout the country, thereby allowing for observations of the microphysical properties of precipitation in regions of the country never before sampled by polarimetric radar. Several fascinating polarimetric signatures in winter storms have recently been discovered. One of the more interesting signatures is an elevated region of enhanced specific differential phase K_{DP} and differential reflectivity Z_{DR}, and reduced copolar correlation coefficient ρ_{hv}. Kennedy and Rutledge (2011) reported on S-band measurements of an elevated layer of K_{DP} in four

Colorado winter storms that had local maxima of ~0.15°–0.4° km^{-1} near the -15°C isotherm. They further showed that the passage of these regions was associated with an increase in surface precipitation. Calculations using an electromagnetic scattering model indicated that highly oblate spheroidal particles with diameters between ~0.8 and 1.2 mm in range and moderate ice densities produced K_{DP} values that were consistent with radar observations. Their calculations were unable to reproduce Z_{DR}. They further concluded that the persistent collocation of this signature with the -15°C isotherm was an indication that rapidly growing dendrites likely played a significant role in producing the elevated K_{DP} signature. In another study of winter storms, Andrić et al. (2013) reported on isolated pockets of enhanced K_{DP} and Z_{DR} that were collocated with reduced ρ_{hv}. These signatures were also found to be located at temperatures between -10° and -15°C, and were coincident with a zone of large radar reflectivity vertical gradient, with the reflectivity factor Z_H increasing toward the ground. Using a simple kinematical, one-dimensional, two-moment bulk microphysical model that was coupled with an electromagnetic scattering model, Andrić et al. (2013) were able to approximately reproduce the correct profile shape and magnitude of Z_H and ρ_{hv} and the correct shape (but not magnitude) of Z_{DR} and K_{DP}. They concluded that their inability to reproduce the correct profiles and magnitudes of all of the signatures indicated that microphysical processes not included in the model, such as secondary ice production, were likely important factors in producing the observed signature. Bechini et al. (2013) also documented enhanced Z_{DR} and K_{DP} values near the model-indicated -15°C isotherm in the ice region of precipitating clouds, using C- and X-band radars in northwestern Italy. They found that these regions of enhancement (K_{DP}

values peaked around 2.0° km^{-1} at C band) were likely associated with dendritic growth and were correlated with the Z_H below.

Ryzhkov et al. (2011) and Kumjian et al. (2011) presented preliminary examinations of distinct and recurring polarimetric signatures in winter storms, including the aforementioned elevated features, providing useful groundwork for future winter weather polarimetric studies. As recognized by Hogan et al. (2002) and Field et al. (2004), plumes of enhanced Z_{DR} are associated with updrafts and the generation of supercooled liquid water in winter convective storms. According to Ryzhkov et al. (2011) and Kumjian et al. (2011), it is likely that some of these updrafts can produce enough graupel for charge separation sufficient to generate electric fields. These electrostatic fields can change the orientation of ice crystals atop these updrafts, which can cause the transmitted radar signal to become depolarized (Ryzhkov and Zrnić 2007; Hubbert et al. 2010a,b; Kumjian et al. 2011; Ryzhkov et al. 2011). The resulting polarimetric signatures reveal the depolarization through radial streaks of enhanced positive and/or negative Z_{DR}.

Other distinct polarimetric signatures presented by Ryzhkov et al. (2011) include downward excursions of the melting layer, characterized by reduced ρ_{hv} and locally maximized Z_H and Z_{DR} extending from the melting layer down to the surface. These excursions are usually associated with melting snowflakes extracting heat from the local environment, resulting in the cooling of ambient air temperatures (Kain et al. 2000). A gradual downward propagation of melting-induced cooling can produce a 0°C isothermal layer, allowing precipitation to fall farther toward the surface before melting entirely; if the melting layer is near the ground, frozen precipitation is more likely to reach the surface

(e.g., Findeisen 1940; Kain et al. 2000). Furthermore, this melting effect is strongest in locations of high precipitation rates (Kain et al. 2000). Downward excursions of the melting layer can also be associated with weak embedded convection, which facilitates the riming of snow above the freezing level (Ryzhkov et al. 2011). Rimed snowflakes have larger terminal velocities and their complete melting within the melting layer occurs at lower heights compared to unrimed snow. Polarimetric signatures of these melting-layer downward excursions to the surface have been associated with abrupt changes in precipitation type reaching the ground, which present a challenge to forecasters. Therefore, polarimetric radar observations of this phenomenon could prove useful in winter weather nowcasting.

The most recently documented winter polarimetric feature is the refreezing signature, which forms in the lower levels beneath the melting layer and is characterized by enhanced Z_{DR} and K_{DP}, and reduced Z_H and ρ_{hv}. Kumjian et al. (2013) documented this signature, and associated environmental conditions, for four winter storms over central Oklahoma, using the S-band polarimetric WSR-88D in Norman, Oklahoma (KOUN), and the University of Oklahoma's C-band Polarimetric Radar for Innovations in Meteorology and Engineering (OU-PRIME), which is also located in Norman. During the events, the refreezing signature occurred when ice pellets were reaching the surface (Kumjian et al. 2013). Possible microphysical mechanisms of the low-level Z_{DR} enhancement include preferential freezing of the smaller drops (so that the raindrop size spectrum becomes more skewed toward larger drops that may freeze later) and the possible local generation of anisotropic ice crystals in the subfreezing air (Kumjian et al. 2013). Further analysis is

needed to thoroughly understand the origin of the ice crystals, as well as to explain the microphysical processes responsible for the occurrence of this unique polarimetric feature. Nevertheless, the refreezing signature will be valuable in detecting transitions of precipitation from freezing rain to ice pellets (Ryzhkov et al. 2011; Kumjian et al. 2013).

This study investigates the evolution and nature of intriguing and previously undocumented polarimetric signatures observed during the 8–9 February blizzard, and examines them in light of the thermodynamic environment within which they developed and the apparent microphysical processes that were active when they appeared. We examine data from the polarimetric WSR-88D S-band radar in Upton, New York (Long Island; KOKX) and environmental thermodynamic analyses from the operational 13-km Rapid Refresh (RAP) model. The model output is used to interpret the polarimetric signatures of different types of ice crystal habits (e.g., needles, plates, stellars, and dendrites) that form in different temperature regimes and regions of ice supersaturation. Polarimetric signatures are also analyzed alongside surface precipitation type observations from Meteorological Phenomena Identification Near the Ground (mPING); the National Weather Service (NWS) Forecast Office in Upton, New York; and Stony Brook University in Stony Brook, New York [observations from Ganetis et al. (2013); approximately 284° azimuth and 23-km range from KOKX]. These data aid in the interpretation of the radar observations.

2. Storm overview

On 8 February 2013, two low pressure systems merged over the northeastern United States, producing a historic winter weather event that ranked among the top five worst blizzards in the region (NART 2014). Figure 2.1 illustrates the evolution of synoptic-scale weather patterns during the event using the 13-km RAP (Cifelli et al. 2005) model analyses. At 1200 UTC, a low was located just off the North Carolina coast, while a second low was located over the Midwest and the 0°C isotherm at 2 m above ground level was located just south of Long Island, New York (Fig. 2.1a). At this time, precipitation was primarily over the mid-Atlantic states. Over the next 12 h, the two systems merged off of the East Coast and the resultant low deepened and progressed northeastward, while the precipitation shield moved over the northeastern United States and New England (Figs. 2.1b,c). By 0000 UTC (9 February 2013), reflectivity values over Long Island were in excess of 50 dBZ. Between 0600 and 1200 UTC (9 February 2013), the surface low moved slowly eastward and precipitation continued to fall over New England (Figs. 2.1d,e). By 1800 UTC, precipitation was no longer falling over Long Island and Connecticut (Fig. 2.1f).

The 24-h accumulated liquid-equivalent precipitation, beginning at 1200 UTC, was in excess of 38 mm over south-central Connecticut and most of Long Island (Fig. 2.2a). Accumulations exceeded 50 mm over central and eastern Long Island and southeastern New Jersey. Precipitation type observations collected by the National Oceanic and Atmospheric Administration/National Severe Storms Laboratory's (NOAA/NSSL) mPING project (Elmore et al. 2014) show a transition of surface precipitation type between 1200

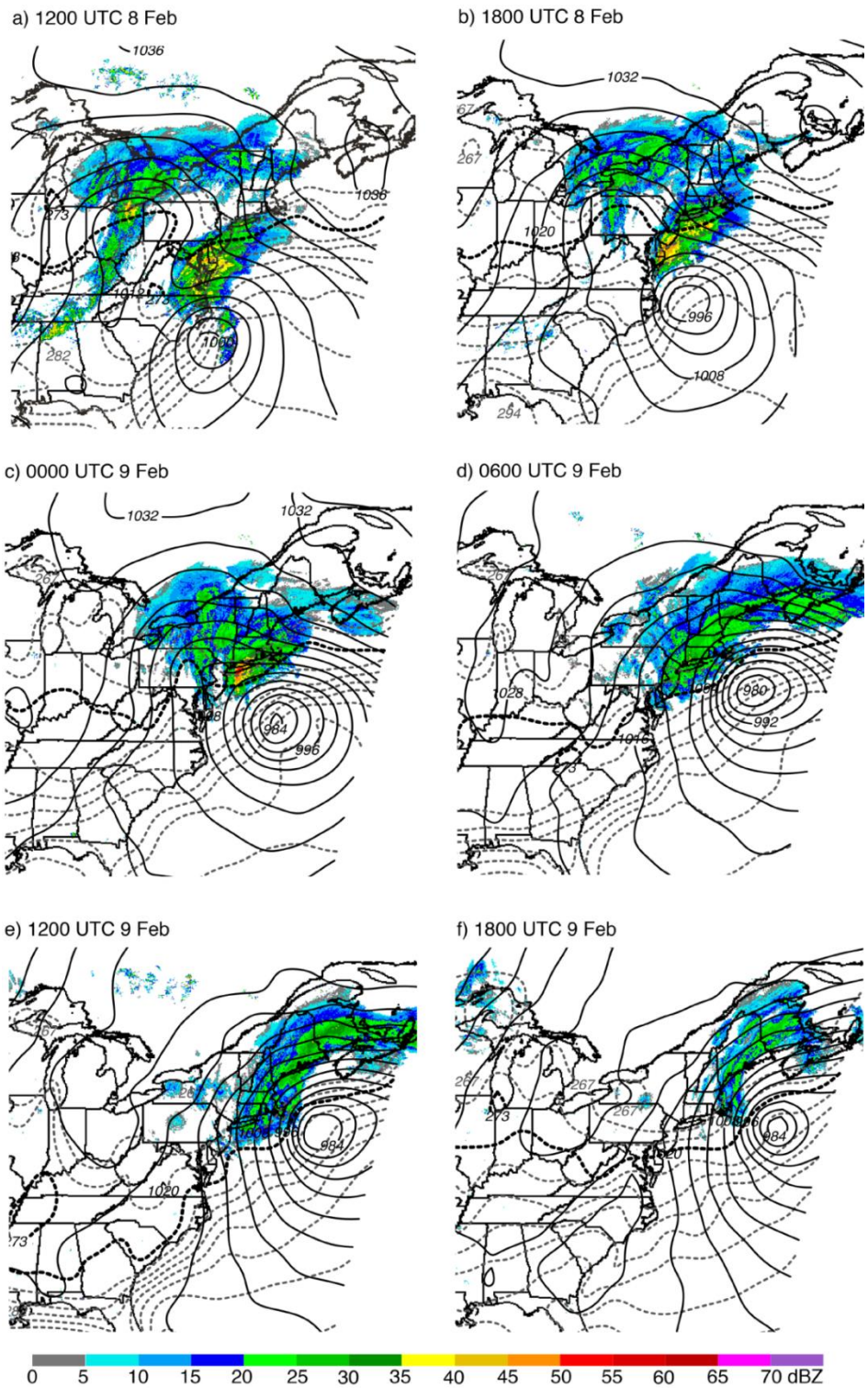

Fig. 2.1: The observed mosaic of composite reflectivity (shaded) and RAP model analyses of sea-level pressure (hPa; solid) and 2-m temperature (°C; dashed). The 273-K (0°C) isotherm is set in boldface.

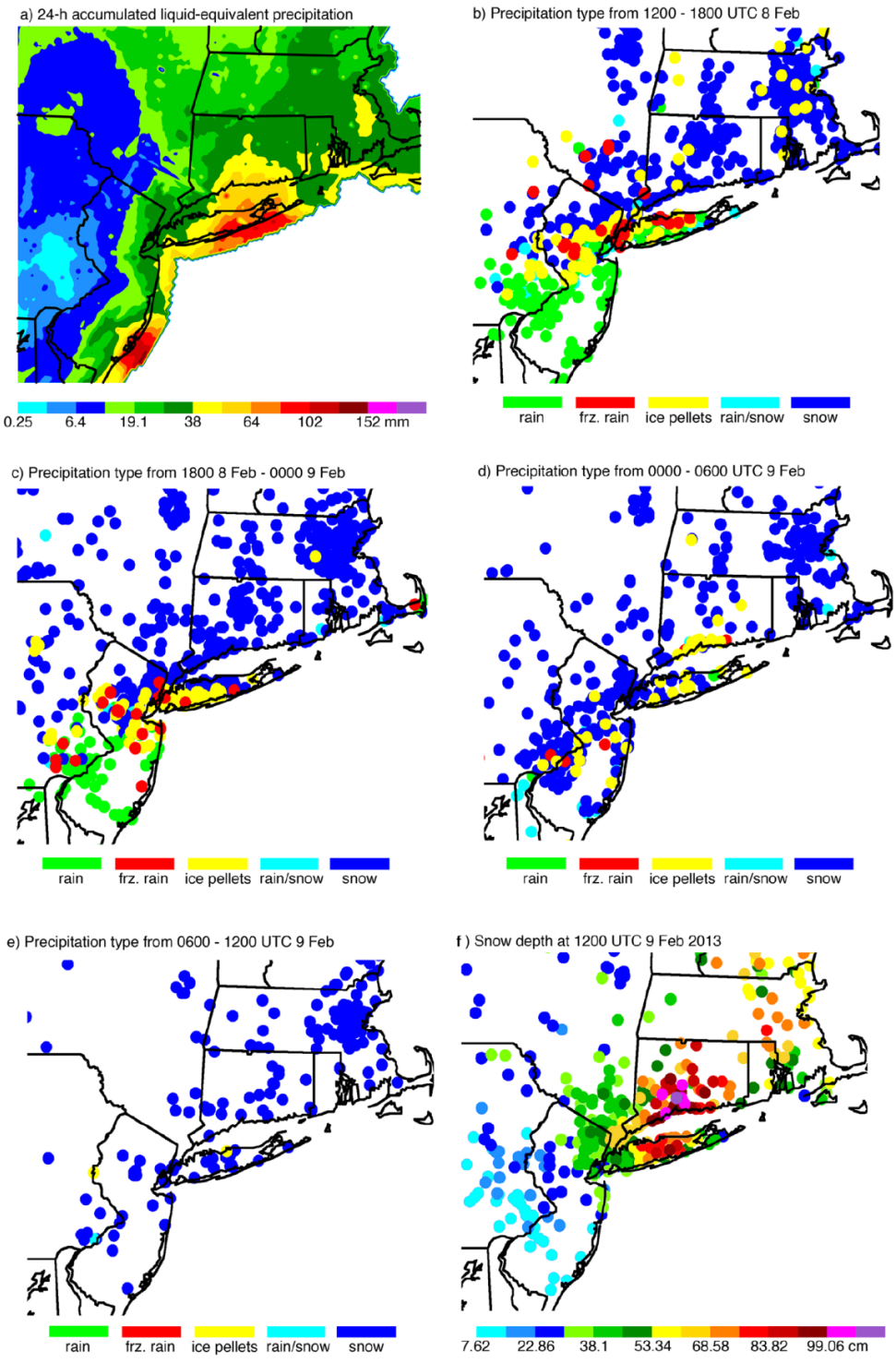

Fig. 2.2: (a) Stage IV analyzed liquid-equivalent 24-h accumulated precipitation beginning at 1200 UTC 8 Feb 2013, (b)-(e) observed precipitation type from mPING, and (f) snow depth from NWS observers and the Community Collaborative Rain, Hail & Snow Network (CoCoRaHS; Cifelli et al. 2005).

and 1800 UTC (Fig. 2.2b). Rain was falling over southern New Jersey, southeastern Pennsylvania, and along the southern coast of Long Island, while a narrow zone of freezing rain and ice pellets was positioned over central New Jersey and along northern Long Island. Snow was the predominant precipitation type over Connecticut, Rhode Island, Massachusetts, and most of New York State. As time progressed, the region of freezing rain and ice pellets shifted slightly southward (Figs. 2.2c,d) with most locations reporting snow by 1200 UTC 9 February (Fig. 2.2e).

By 1200 UTC (9 February 2013), total snow accumulations exceeded 50 cm over central Long Island, Connecticut, and Massachusetts (Fig. 2.2f). Heavy snowfall and blizzard conditions occurred from northern New Jersey, inland to New York, and northward through Maine (Fig. 2.3). Storm-total snow accumulations of 30–61 cm were common, with amounts surpassing 61 cm over a SW–NE-oriented band from Long Island to southern Maine. Maximum accumulations up to 102 cm, as well as snowfall rates exceeding 15 cm h^{-1}, were reported in parts of Connecticut. In addition to record-setting snow accumulations, significant coastal flooding and hurricane-force wind gusts were recorded along the coast (Picca et al. 2014). Impacts of the event included at least 18 fatalities, thousands of flight cancellations at major airports, travel bans, and hundreds of thousands of customers throughout the region left without electricity for several days (NWA 2014; Associated Press 2014).

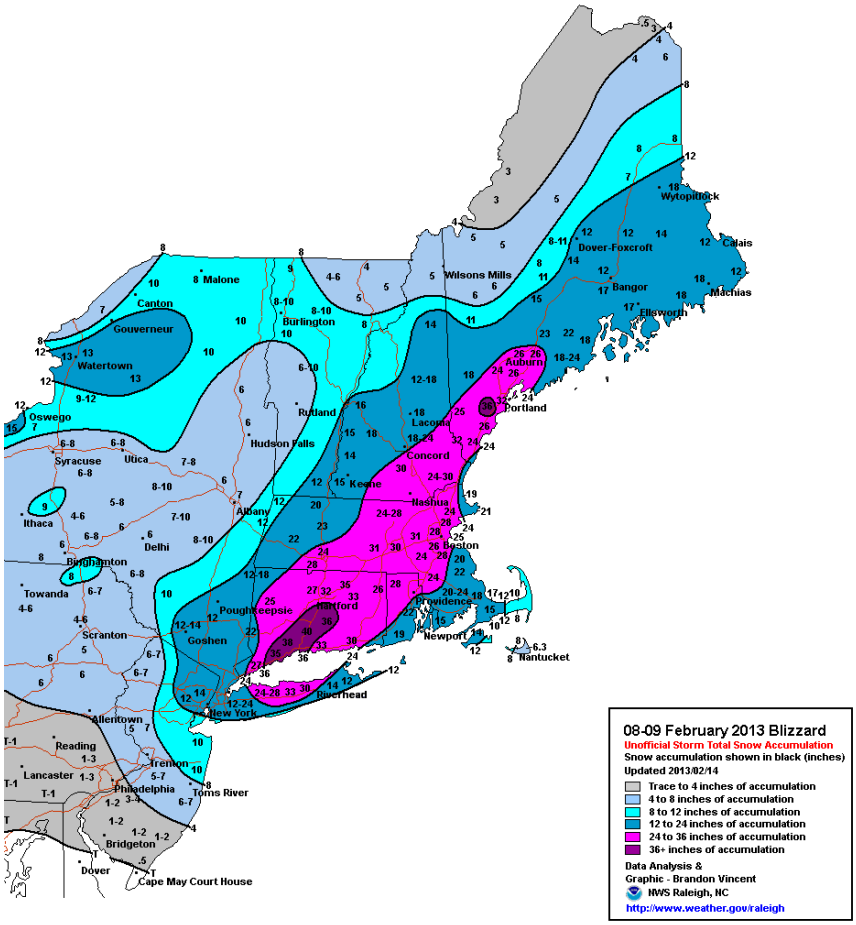

Fig. 2.3: Storm-total snow accumulation from the 8-9 Feb 2013 blizzard (Courtesy B. Vincent of the NWS Forecast Office in Raleigh, North Carolina.)

3. Observational analysis

Here, we present polarimetric radar observations of some of the intriguing features of the Northeast blizzard during the observational period from 1000 UTC 8 February through 0400 UTC 9 February 2013. This time period includes the onset and intensification phases of the system and the subsequent period during which the Midwest and mid-Atlantic surface low pressure centers merged, resulting in a strengthening of the

surface low, rapid cooling of the thermal profile, lower-density snow, and reduced Z_H across the region.

a. High Z_H near the surface

One of the more remarkable features of this storm was the extremely high Z_H observed near the surface (especially after 2100 UTC), which reached magnitudes greater than 50 dBZ in regions of wet snow. This is considerably higher than the ~40-dBZ maximum typically reported in previous studies (e.g., Ryzhkov and Zrnić 1998). Table 2.1 provides a summary of typical polarimetric values of cold-season precipitation types. Note that in the case of an anomalous event, it is possible to observe values outside of the ranges provided.

Table 2.1: Typical ranges of values of some polarimetric variables of cold-season precipitation types, at S band. [Adapted from Ryzhkov and Zrnić (1998), Straka et al. (2000), Park et al. (2009), Andrić et al. (2013), Kumjian et al. (2013, 2014), and Picca et al. (2014).]

Precipitation type	Z_H (dBZ)	Z_{DR} (dB)	ρ_{hv}
Dry aggregated snow	<35	0–0.5	>0.97
Wet aggregated snow	<45	0.5–3	0.90–0.97
Nondendritic pristine crystals	<20–25	−3–7	>0.98
Dendritic crystals	<30–35	0.5–3	<0.98
Rimed snow	<30–40	0–0.5	>0.98
Pure rain	<55	0–5	>0.97
Freezing rain	<35–40	0–1	>0.98
Ice pellets/sleet	<30	0–0.5	>0.98
Large graupel–small hail	35–60	Dry: −0.5–0.5	Dry: >0.95
		Wet: 0.5–4	Wet: 0.8–0.95

During the time period shown in Figs. 2.4a and 2.4d, the maximum Z_H near the surface (at 0.5° elevation, and below 1.5 km) remained >50 dBZ and the precipitation band appeared to pivot to a more north–south orientation as the low pressure center traversed northeastward. The type of precipitation at 2216 UTC, as inferred from the polarimetric observations, is indicated in Figs. 2.4a–c. Pure, dry snow exists north of the model-indicated 0°C wet-bulb temperature T_W isotherm (Z_H < 35 dBZ, Z_{DR} of 0–0.5 dB, and ρ_{hv} near 1). Wet snow, snow, and ice pellets are indicated south of the 0°C isotherm and in regions of Z_H ranging from 40 to 60 dBZ, Z_{DR} from 1.2 to 3.5 dB, and ρ_{hv} as low as 0.75. These precipitation types are in agreement with mPING observations and those taken by meteorologists and cooperative observers for the NWS Forecast Office in Upton, which indicate snow and a mixture of ice pellets, snow, and various snow mixtures to the north and south of the 0°C isotherm, respectively.

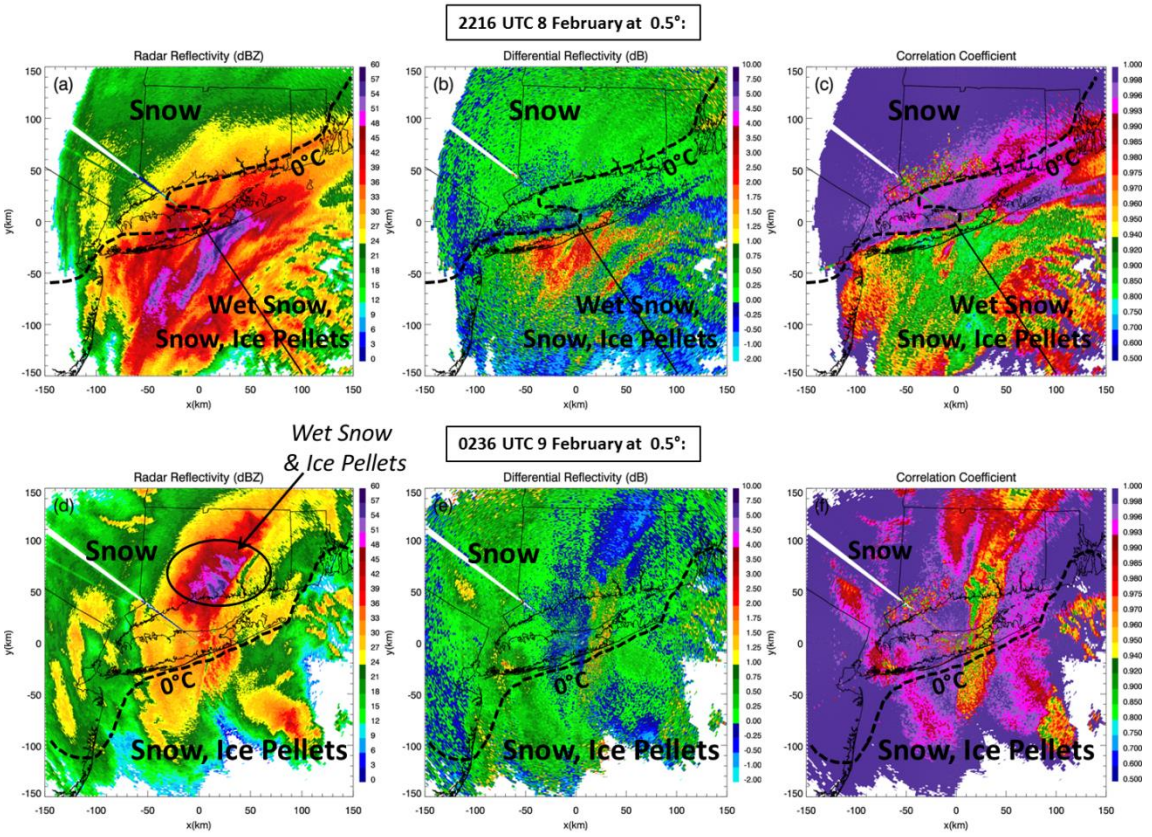

Fig. 2.4: PPI displays of the polarimetric variables at (a)-(c) 2216 UTC 8 Feb and (d)-(f) 0236 UTC 9 Feb 2013, at 0.5° elevation. The 0°C RAP model TW at the surface is overlaid (boldface, dashed). At 2216 UTC, pure dry snow was located within colder temperatures north of the 0°C isotherm, while wet snow and mixed-phase hydrometeors occurred within warmer temperatures south of the 0°C isotherm in (a)-(c). The solid black line indicates the location of the 144° azimuth RHI in Fig. 2.5. At 0236 UTC, dry snow was predominant, while wet snow and ice pellets were also observed within the max ZH region, within negative surface temperatures, north of the 0°C isotherm in (d)-(f).

Figure 2.5 depicts a reconstructed RHI through a high reflectivity band at 2216 UTC. Regions of exceptionally large Z_H (>50 dBZ) are confined to a shallow layer below 1.5 km throughout the entire observational period, while Z_H greater than 24 dBZ remains below approximately 6 km. According to Ganetis et al. (2013), these extremely high Z_H values near the surface may be partly attributed to frontogenesis. They found that, as the

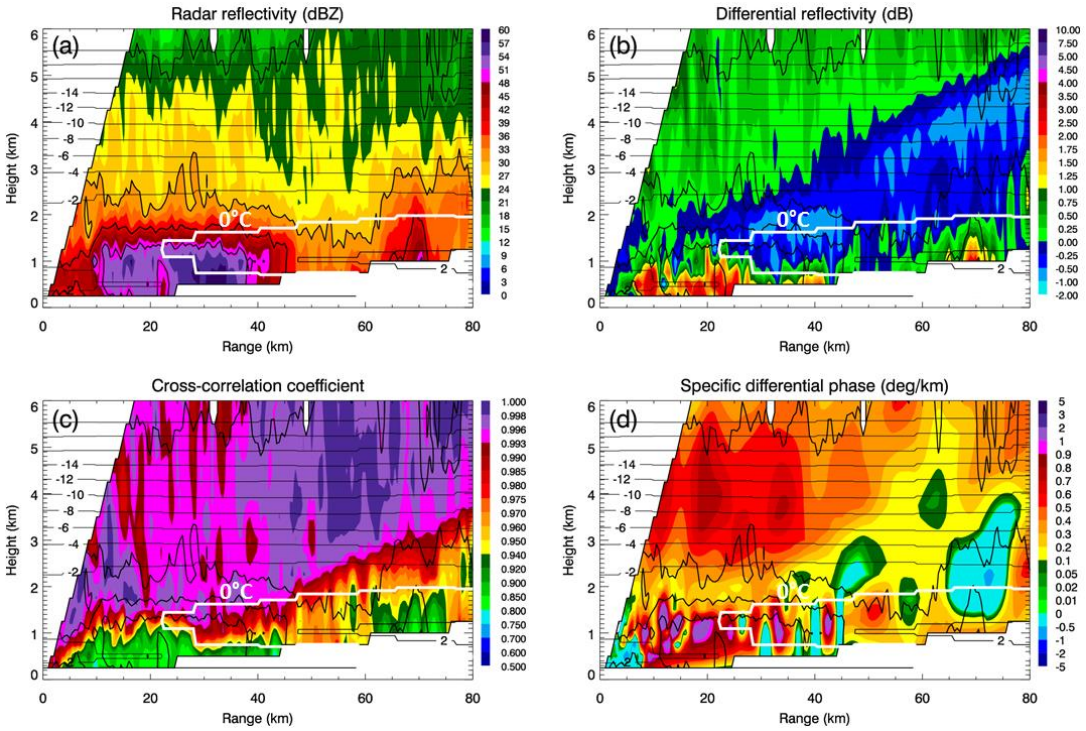

Fig. 2.5: RHIs at 2216 UTC 8 Feb 2013 of (a) ZH, (b) ZDR, (c) ρhv, and (d) KDP at 144° azimuth. In each RHI, ZH is contoured at 20, 30, 40, and 50 dBZ. Contours of RAP model TW are also overlaid (°C). The model-indicated 0°C isotherm is identified by the white contour.

system intensified, the environment became more unstable and convective as temperatures exceeded 0°C at approximately 850–800 hPa in the warm layer within the band, which was associated with the trough of warm air aloft as well as subsidence warming within the band circulation; these processes resulted in the production of sleetlike hydrometeors and the Z_H values >50 dBZ. After frontogenesis and subsidence warming decreased in magnitude, cold-air advection became dominant and led to a rapid transition (i.e., within an hour) to lower Z_H values (Ganetis et al. 2013). The corresponding Z_{DR} is high and ρ_{hv} is low in the shallow layer of extremely high Z_H, which testifies that large wet snowflakes or even melting ice hydrometeors (e.g., graupel and/or hail) are dominant scatterers there, despite

the model profile indicating that no melting would be expected. This illustrates an apparent inconsistency between the type of precipitation identified by the radar and the wet-bulb temperatures retrieved from the RAP model at distances closer than 20 km from the radar, where $T_W < 0°C$ in the whole depth of the atmosphere (where melting is not anticipated). The radar reflectivity is highest just below the "nose" of the melting layer, where the transition from dry hydrometeors with low Z_{DR} and high ρ_{hv} to melting precipitation with high Z_{DR} and low ρ_{hv} occurs at lower levels than in surrounding areas. This is an indication of larger-sized rimed snow and/or hail, which is melting at lower heights due to its higher terminal velocity. It is possible that ice crystals generated aloft descend into a layer of localized convection and abundant moisture along the front and start growing via riming, which results in rapid enhancement of Z_H in a relatively shallow surface layer. The pocket of low Z_{DR} above the high-Z_H region indicates the localized region where riming is occurring, leading to larger fall speeds of the hydrometeors and a lowering of the melting level. Another possible mechanism for the depressed melting level is localized cooling due to the melting of heavy precipitation and large aggregates (e.g., Stewart 1984; Stewart et al. 1984; Oraltay and Hallett 2005). This type of cooling can produce local near-0°C isothermal layers, allowing partially melted hydrometeors to reach the surface (e.g., Findeisen 1940; Wexler et al. 1954; Szeto et al. 1988; Ryzhkov et al. 2011). Figure 2.6 provides a conceptual model illustrating these two possible mechanisms.

Surface reports of a mixture of ice pellets (mPING) and "large sleet" resembling pea-sized hail (R. Hanrahan 2013, personal communication; Picca et al. 2014) confirmed that, in addition to contributions from melting snow in this region of maximum Z_H, there

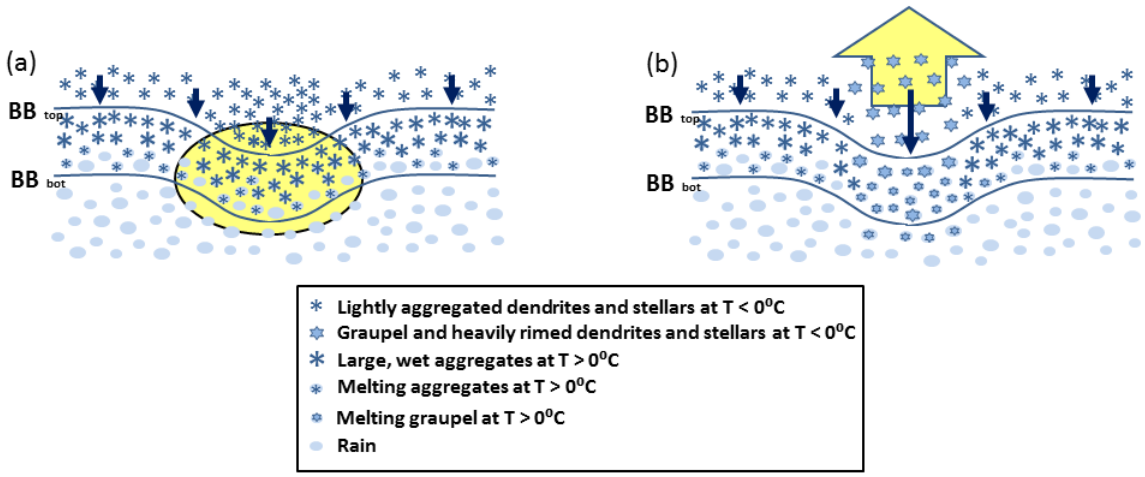

Fig. 2.6: Conceptual model showing two possible mechanisms for producing a downward excursion in the radar bright band: (a) a localized region of enhanced cooling due to evaporation and melting (indicated by the yellow-shaded oval) associated with heavier precipitation, and (b) a localized region of enhanced updraft (indicated by the yellow-shaded arrow) that produces rimed particles that have a larger fall speed than the surrounding hydrometeors. Solid arrows offer a comparison of the relative fall speeds between lightly aggregated stellars/dendrites and heavily rimed stellars/dendrites. When compared to (a), rimed particles in (b) would likely produce slightly enhanced Z_H and reduced Z_{DR} above the bright band and slightly enhanced Z_H and Z_{DR} below the bright band. Each process might be responsible for possible changes in surface precipitation type when occurring at sufficiently low altitudes.

may have also been contributions from wet growth and melting of refrozen hydrometeors. The presence of wet snow and melting graupel/hail beneath the melting layer, such as exists in this event, can serve to alert forecasters to the potential for localized convection and the associated riming of ice crystals aloft to locally alter the precipitation type at the surface. It is interesting to compare the location of the RAP 0°C isotherm with the apparent 0°C isotherm in the radar observations (given by the strong north-to-south gradients in Z_{DR} and ρ_{hv} along the northern shore of Long Island; Figs. 2.4b,c). The RAP 0°C isotherm is approximately 40 km north of this line. Without 2-m temperature observations over Long Island Sound, one cannot definitely state the RAP model is errant.

However, the comparison does highlight the advantage of using dual-polarization data over model data to distinguish where transitions in precipitation type exist.

By 0236 UTC (Figs. 2.4d–f), the region of maximum $Z_H > 50$ dBZ shifted north of KOKX (over Connecticut), and north of the model-indicated 0°C isotherm (e.g., Fig. 2.4d; 0236 UTC 9 February 2013), into colder temperatures. After the main snowband traversed north of the 0°C isotherm, polarimetric observations show that dry snow became the predominant precipitation type, while ice pellets were also observed at the surface (Figs. 2.4d–f; mPING). The polarimetric variables in Figs. 2.4e and 2.4f also depict a north–south transition line extending from central Long Island to the southern shore of Connecticut that is not reflected in the RAP analyzed 2-m temperature. Indeed, mPING observations reveal that the precipitation type to the west of this line is snow and to the east is ice pellets. Given that the height of the elevation angle is between 0.5 and 1.5 km above ground level in this region, the disagreement between the RAP analysis [and the RAP temperatures interpolated to the radar surface (not shown)] and the radar observations may indicate that the RAP model failed to capture the temperature field accurately at this time, again underscoring the value in using dual-polarization observations for inferring precipitation type transition zones. It is also important to note that the RAP data aloft at this time (not shown) exhibited no evidence of an elevated warm layer in this region, precluding the possibility of a warm layer causing the occurrence of the mixed-phase precipitation in this localized region.

b. Differential attenuation

Another prominent feature observed throughout the event was the remarkable differential attenuation manifested by large negative values of Z_{DR} down to -2 dB along the radar beams propagating through regions of heavy, wet snow (e.g., Figs. 2.5 and 2.7). To the authors' knowledge, the differential attenuation values presented in this manuscript are larger than previously reported for other winter storms. After a radar beam propagates through heavy wet snow and mixed-phase hydrometeors, the incident electromagnetic energy is absorbed and scattered, resulting in loss of power and reduction in echoes farther down the radial (Doviak and Zrnić 1993, p. 38). Given the occurrence of intense

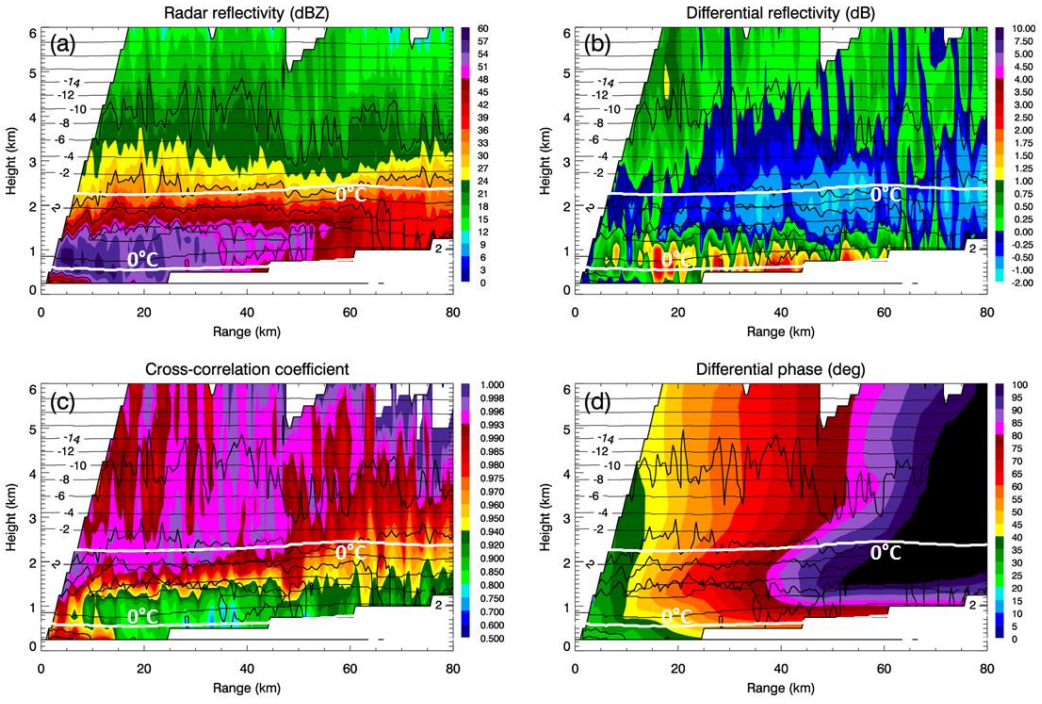

Fig. 2.7: RHIs at 2233 UTC 8 Feb 2013 of (a) Z_H, (b) Z_{DR}, (c) ρ_{hv}, and (d) Φ_{DP} at 216° azimuth. In each RHI, Z_H is contoured at 20, 30, 40, and 50 dBZ. Contours of the RAP model T_W are also overlaid (°C). The model-indicated 0°C isotherm is indicated by the white contour. The max T_W within the model-indicated warm layer was approximately 4°C.

(>50 dBZ) heavy wet snow at the surface, it is not surprising that attenuation and differential attenuation observations in this system reached magnitudes that appear to exceed those previously documented for S-band radar observations. It should be noted that all Z_{DR} values shown in this paper were corrected for differential attenuation using the standard correction for pure rain,

$$\Delta Z_{DR} = -\beta \phi_{DP}, \tag{2.1}$$

in which the correction factor β = 0.004 dB $(°)^{-1}$ (Ryzhkov and Zrnić 1995). Despite this correction, large regions of negative Z_{DR} are observed throughout most of the observational period, which suggests that differential attenuation in wet snow/graupel is significantly higher than in pure rain. This is clearly illustrated in the RHI plots in Figs. 2.5 and 2.7. The reduced negative Z_{DR} values are observed above the layer of enhanced Z_H (Figs. 2.5b and 2.7b). Differential phase Φ_{DP} rapidly accumulates down radial of the heavy wet snow region, exceeding 100° (Fig. 2.7d), confirming that the negative bias of Z_{DR} is attributed to differential attenuation.

Figure 2.8 displays line plots of Φ_{DP}, Z_{DR}, and ρ_{hv} as functions of range, at the 2.4°-elevation scan along the 2233 UTC 216° azimuth. It should be noted that Φ_{DP} has been smoothed, according to the preprocessing procedures detailed by Ryzhkov et al. (2005). Beginning at a range of ~10 km, there was a rapid increase in Φ_{DP}, with values reaching 125° at 100 km (Fig. 2.8a). In wet snow, Z_{DR} peaked at ~2.7 dB and then decreased and remained mostly negative (due to substantial differential attenuation) over a large range beyond approximately 30 km (Fig. 2.8b). At ranges between 10 and 35 km, ρ_{hv} was

reduced when the beam propagated through the wet snow and mixed-phase precipitation at the lower heights near the surface (Fig. 2.8c). Note that K_{DP} values in wet

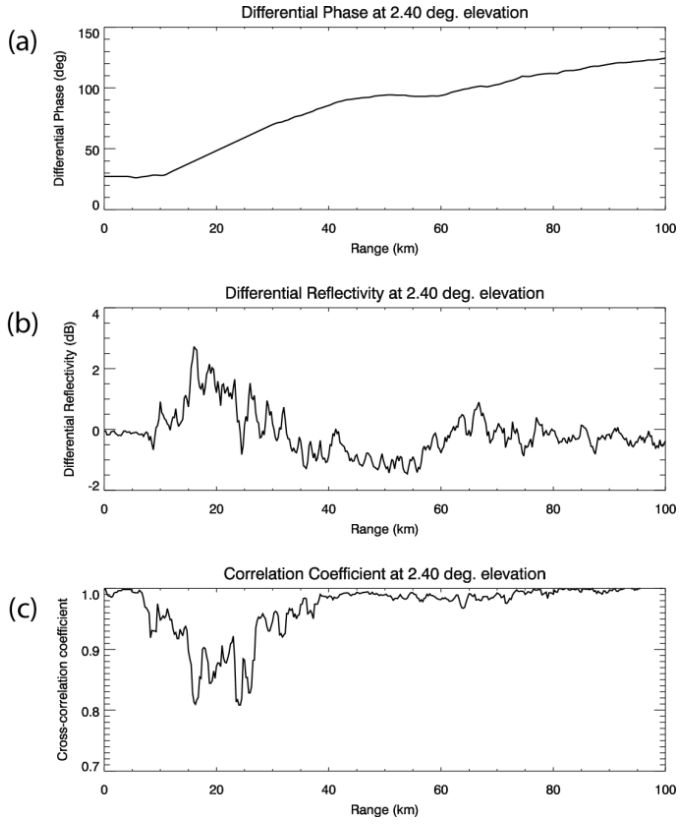

Fig. 2.8: Line plots at 2233 UTC 8 February 2013 of (a) Φ_{DP}, (b) Z_{DR}, and (c) ρ_{hv} as functions of range from KOKX, at 2.4° elevation, along the 216° azimuth. At this time, the 2.4°-elevation scan was sampling the heavy, wet snowband with Z_H up to 60 dBZ, located between ranges of approximately 10 and 55 km.

snow were approximately 1° km^{-1} (Fig. 2.5d), which is consistent with high K_{DP} values of ~1°–1.3° km^{-1} in melting snow documented by Ryzhkov and Zrnić (1998).

To better quantify the factor β in Eq. (2.1) in wet snow, the ratio of the negative Z_{DR} bias (i.e., ΔZ_{DR}) and the corresponding differential propagation phase (i.e., Φ_{DP}) has been estimated for several radials that exhibited substantial differential attenuation. An

analysis of several radials over the entire observational period yields an average factor β in the range from 0.015 to 0.025 dB $(°)^{-1}$. These β magnitudes are much larger than the ones expected at S band for pure rain and on the same order of magnitude as the corresponding factors reported in melting hail (Ryzhkov et al. 2013), likely due to the large melting aggregates mixed with ice hydrometeors including melting hail and/or melting graupel.

Differential attenuation occurred throughout the entire observational period, becoming more distinct as the event progressed. The 1.45° plan position indicator (PPI) Z_{DR} imagery at 0001 UTC 9 February 2013 (Fig. 2.9) depicts differential attenuation, indicated by Z_{DR} values from -2 to 0 dB to both the southwest and northeast of KOKX. These negative Z_{DR} values occur down radial of the region of Z_H > 55 dBZ, Z_{DR} > 1dB, and ρ_{hv} < 0.97 (Fig. 2.9) within a 50-km range of the radar. An analysis of the polarimetric observations at this time suggests the precipitation type in the region of greatest attenuation is wet snow. Special observations taken by observers at Stony Brook University with an ice microscope [presented in Ganetis et al. (2013) and Picca et al. (2014)] also indicate there was a mixture of different frozen habits, including a new variety of hydrometeor coined "asteroid ice." This type of hydrometeor had the appearance of small, irregular hail and exhibited a heavily rimed exterior with a diameter of approximately 1.5–2.5 mm, indicating a formation mechanism similar to that of hail: it is expected that ice crystals were generated aloft due to depositional growth, descended into the updraft, and then became heavily rimed due to abundant supercooled water within a warm, moist, and shallow region above the surface.

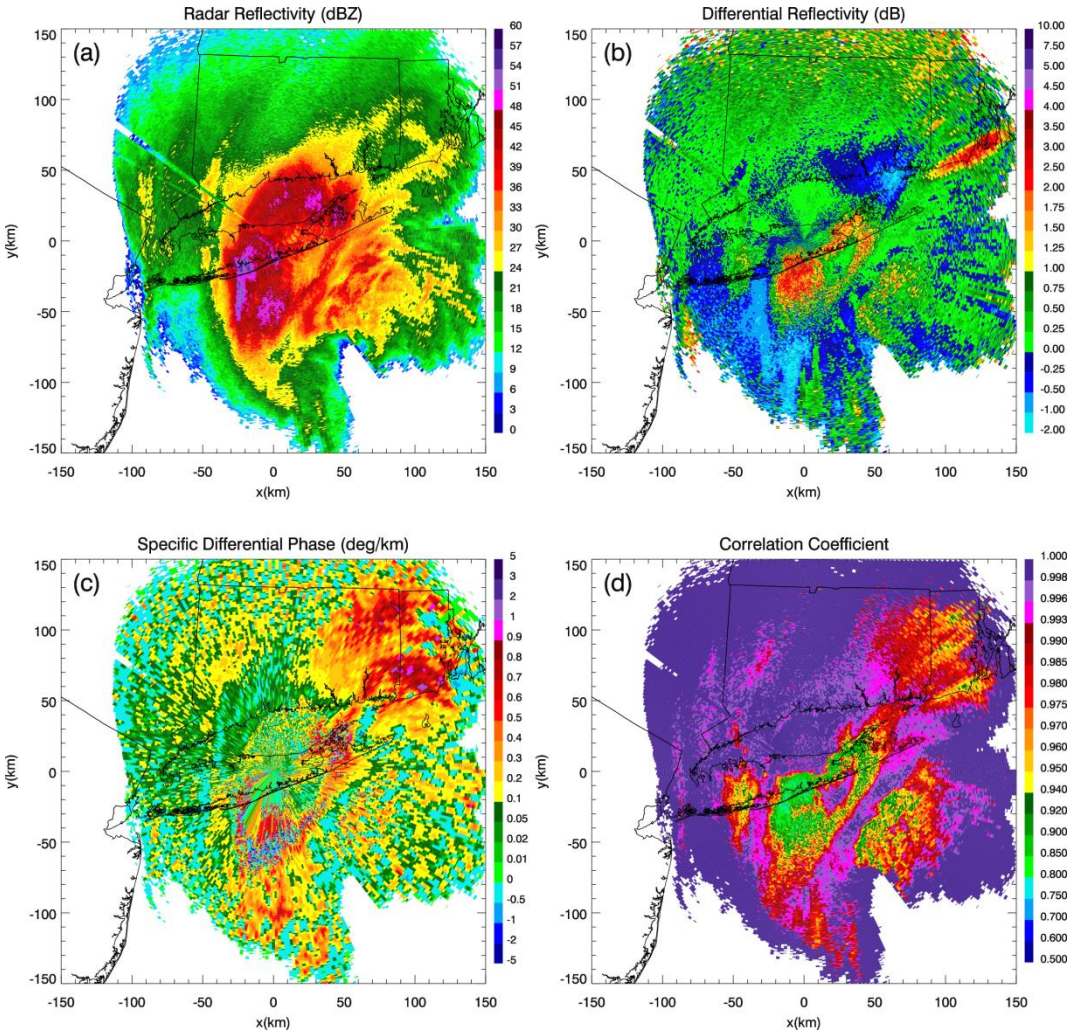

Fig. 2.9: PPIs at 0001 UTC 9 Feb 2013 of (a) Z_H, (b) Z_{DR}, (c) K_{DP}, and (d) ρ_{hv} at 1.45° elevation. Distances are relative to KOKX.

c. Downward excursion of the melting layer

A downward excursion of the melting-layer bright band (MLBB) became evident by 1300 UTC 8 February (e.g., 1354 UTC 8 February; Fig. 2.10). This feature is indicated by the north end of the semicircular region of low ρ_{hv}, moderate-to-high Z_{DR}, and low-to-moderate Z_H located along the southern shore of Long Island. During this time, mPING

observations show a corresponding transition from rain and ice pellets in the south to snow in the north (Figs. 2.2b and 2.10d). Figure 2.11 provides an RHI perspective of the

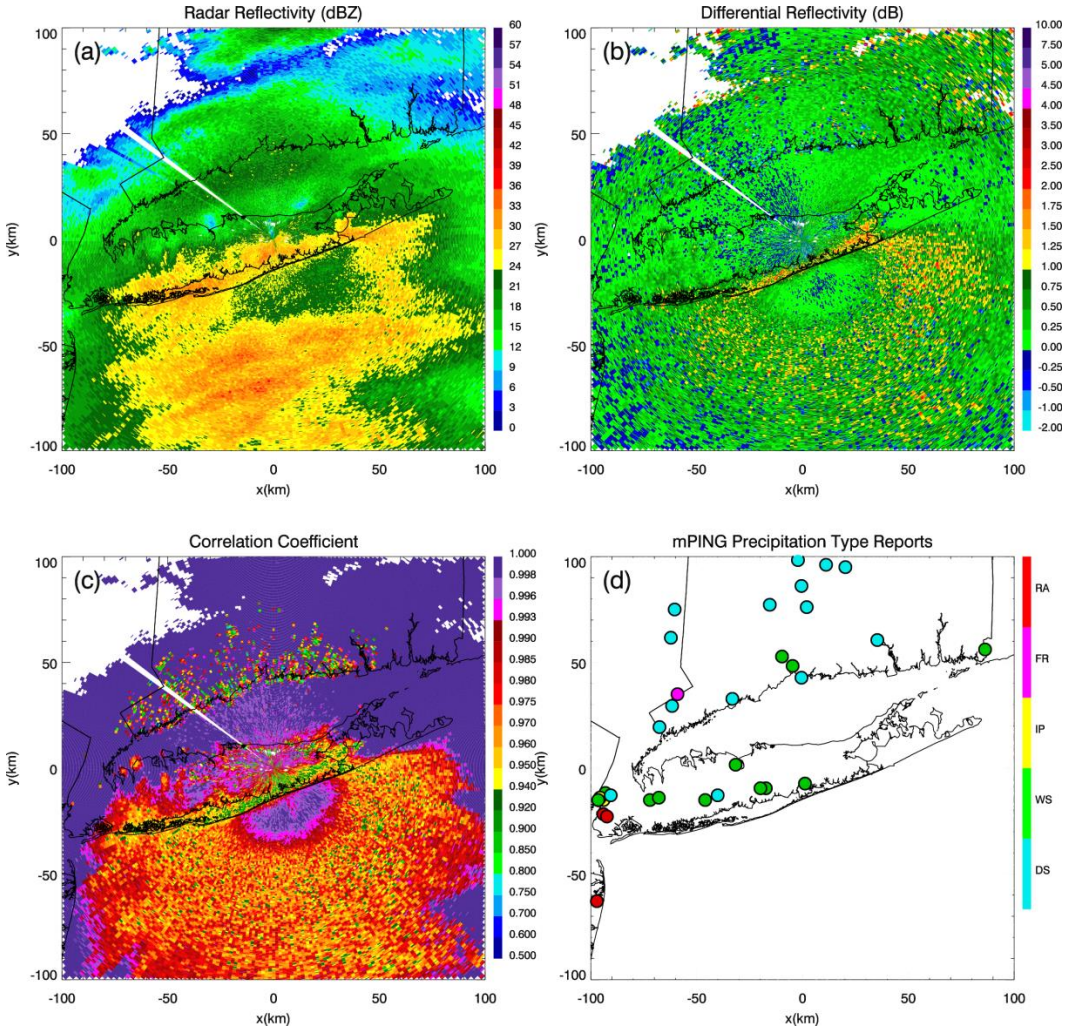

Fig. 2.10: PPIs at 1354 UTC 8 Feb 2013 of (a) Z_H, (b) Z_{DR}, and (c) ρ_{hv} at 0.5° elevation. (d) The mPING surface precipitation type reports for the 30 min centered at 1354 UTC (i.e., 1339 to 1409 UTC). The downward excursion of the MLBB to the surface (distinct in ρ_{hv} and Z_{DR}) was associated with an observed transition line of precipitation types at the surface.

downward excursion of the melting layer toward the surface, supplemented by a range-versus-height schematic to aid in the interpretation of this phenomenon. Areas where the

0.5° radar beam (with a 1° beamwidth) is at least partially contaminated by the MLBB (high Z_{DR} and low ρ_{hv}) are indicated by the yellow shading, and areas where the beam passes through pure rain (low Z_{DR} and high ρ_{hv}; center of the semicircle) are indicated by the green shading.

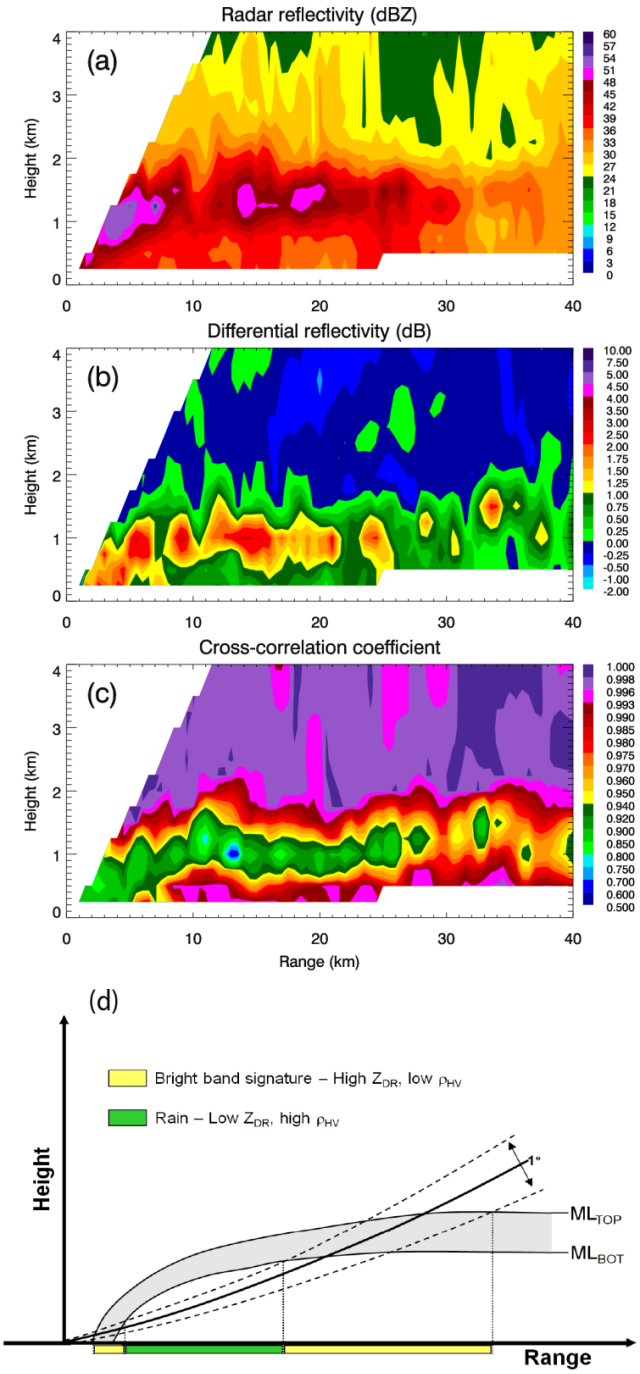

Fig. 2.11: RHIs at 2350 UTC 8 Feb 2013 of (a) Z_H, (b) Z_{DR}, and (c) ρ_{hv} at 143° azimuth, illustrating a downward excursion of the MLBB. (d) Range-vs-height schematic of the MLBB sloping downward toward the surface, with a hypothetical 0.5°-elevation scan (with a 1° beamwidth) overlaid. The radar beam increases in range and height from KOKX. Areas where the 1°-wide radar beam is contaminated by the bright band (high Z_{DR} and low ρ_{hv}) are indicated by the yellow shading, and areas where the beam passes through pure rain (low Z_{DR} and high ρ_{hv}) are indicated by the green shading.

As time progressed, a bubble-like feature became evident in the ρ_{hv} and Z_{DR} imagery, located slightly northeast of KOKX (i.e., centered at approximately x = 10 km, y = 20 km in Figs. 2.12b,c and x = 8 km, y = 35 km in Figs. 2.13b,c); it was initially attached to the north end of the MLBB semicircle and then curiously fluctuated in size and distance from it during approximately 3 h. The bubble was characterized by enhanced

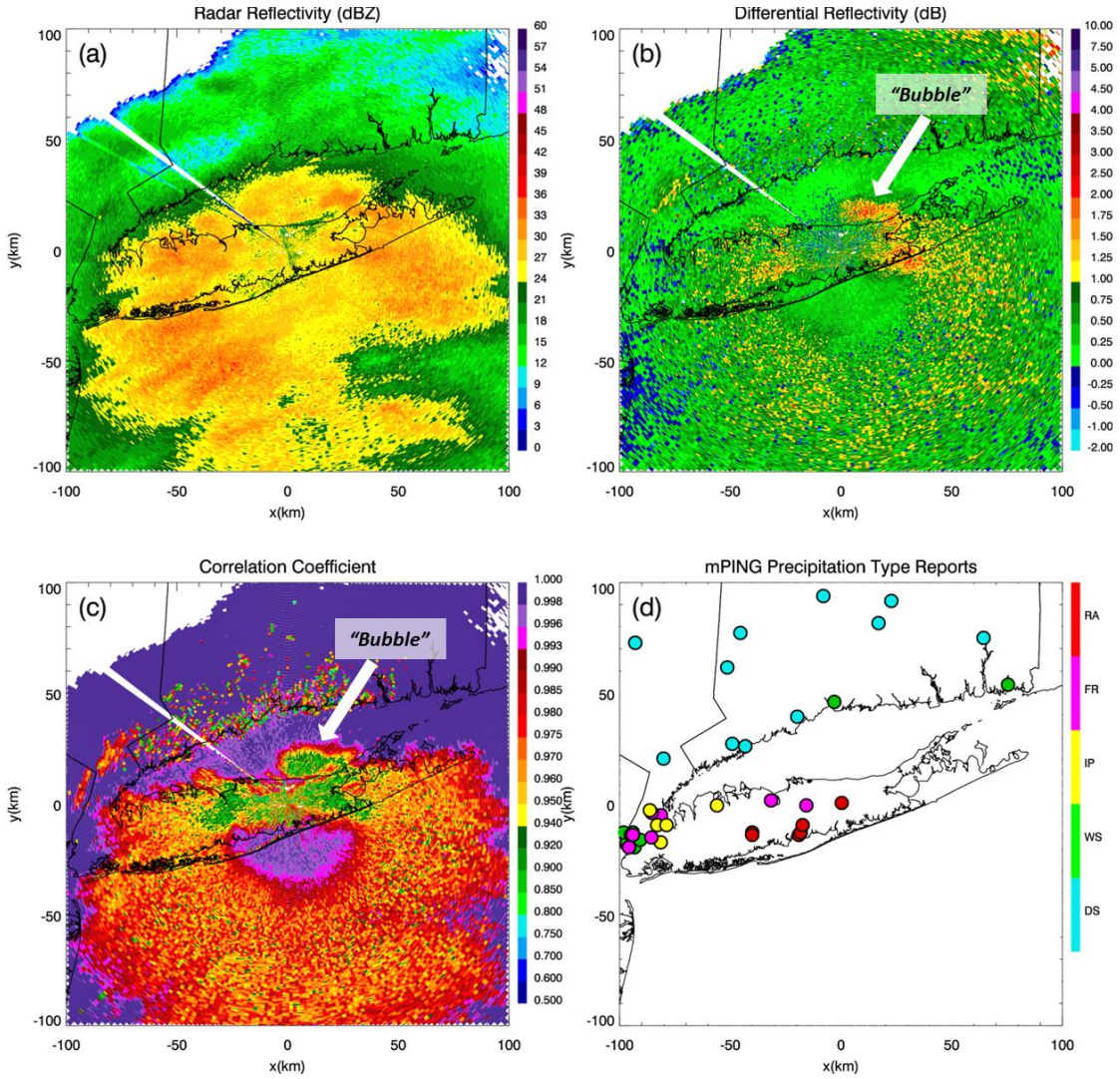

Fig. 2.12: As in Fig. 2.10, but for 1459 UTC 8 Feb 2013. The mPING observations are shown for the 30 min centered at 1459 UTC (i.e., 1444 to 1514 UTC). The bubble-like feature is centered at approximately x = 10 km, y = 20 km in (b) and (c).

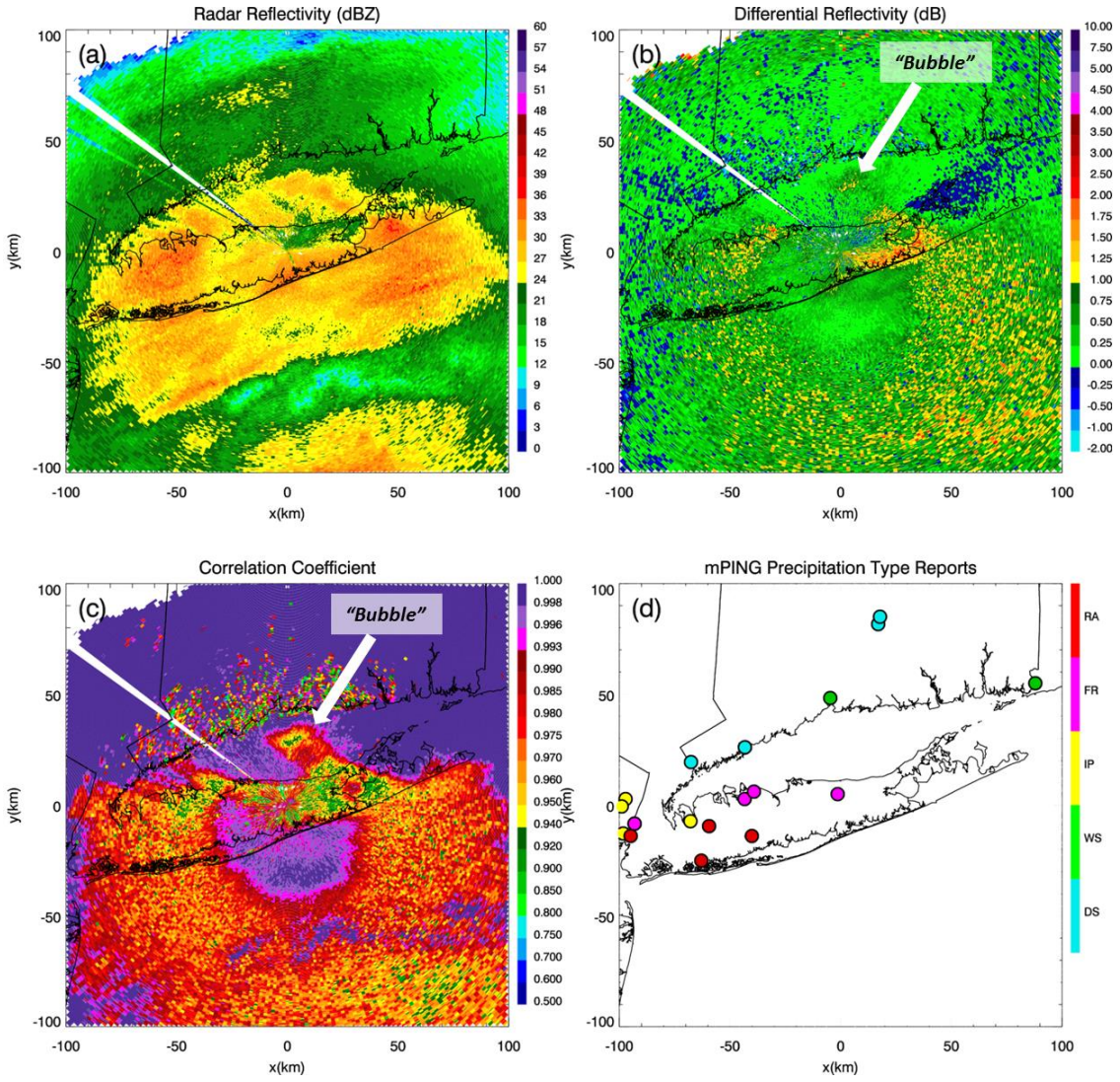

Fig. 2.13: As in Fig. 2.10, but for 1557 UTC 8 Feb 2013. The mPING observations are shown for the 30 min centered at 1557 UTC (i.e., 1542 to 1612 UTC). The bubble-like feature is centered at approximately x = 8 km, y = 35 km in (b) and (c).

Z_{DR} (1–2.5 dB) and reduced ρ_{hv} (as low as 0.9), and was first observed just after 1400 UTC. The semicircular MLBB-to-ground signature became progressively more distinct with increasing elevation and time. By 1459 UTC, the bubble had become larger and more distinct (Fig. 2.12). Eventually, it began to detach from the semicircle, becoming nearly completely detached by 1557 UTC (Fig. 2.13). By 1659 UTC, it had nearly completely

dissipated, leaving the semicircle with a more distinct horizontal line (i.e., transition line) of reduced ρ_{hv} and enhanced Z_{DR} (Figs. 2.14b,c). According to the polarimetric imagery, the bubble was located north of the transition line, within the region of snow indicated by $\rho_{hv} > 0.996$, $Z_{DR} < 0.75$, and $Z_H < 30$ dBZ (e.g., Figs. 2.12a-c). Therefore, the bubble was

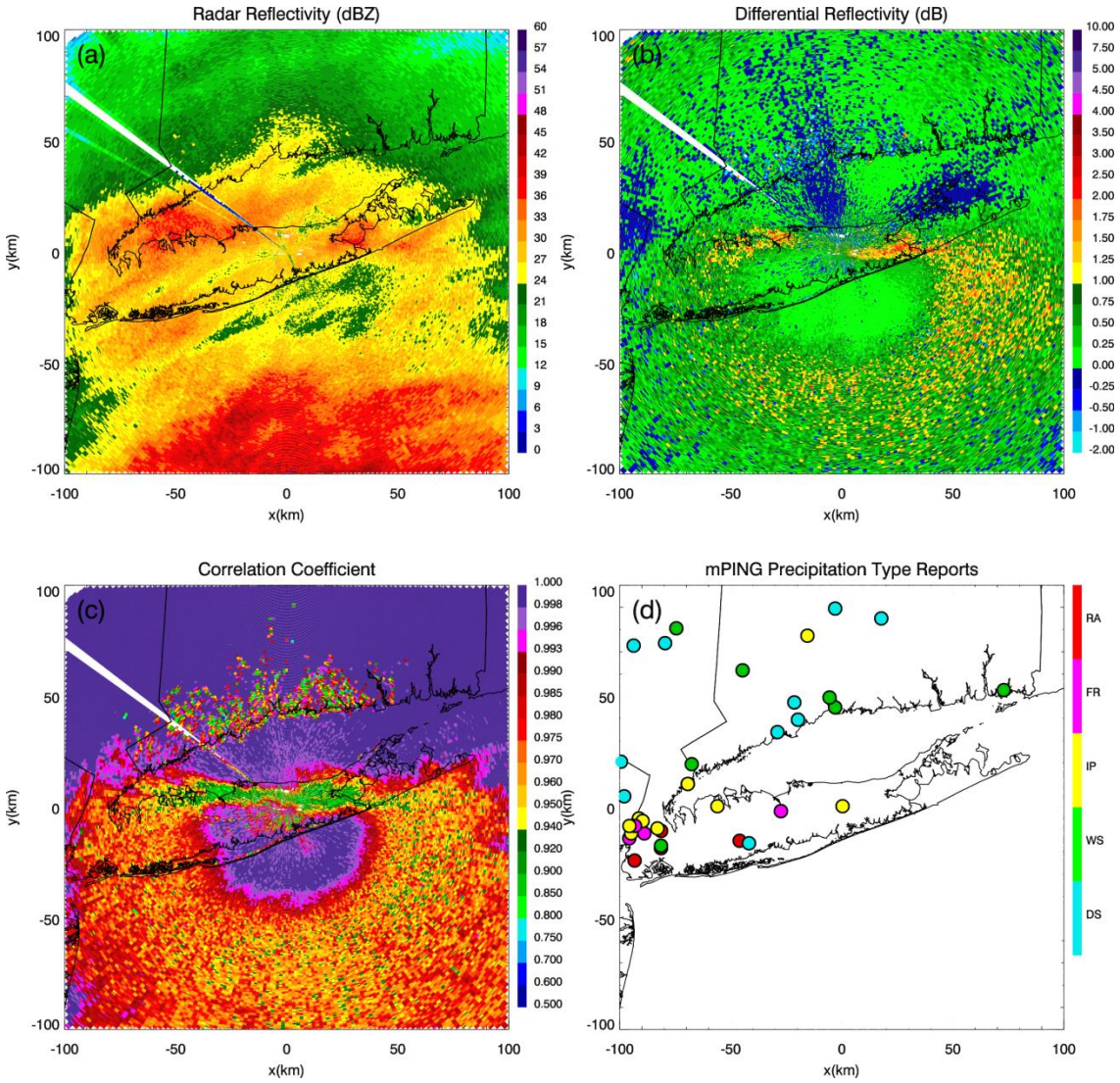

Fig. 2.14: As in Fig. 2.10, but for 1659 UTC 8 Feb 2013. The mPING observations are shown for the 30 min centered at 1659 UTC (i.e., 1644 to 1714 UTC).

potentially a pocket of wet snow associated with local convection and riming aloft within the associated updraft. Before dissipating, it propagated into the colder air temperatures, predominantly carried by the prevailing winds from the south. By 1900 UTC, the downward excursion of the MLBB had become less distinct, as heavy precipitation bands moved northward and meshed with the semicircle, appearing as a widespread region of precipitation with a horizontal leading transition line (not shown).

During the evolution period, the polarimetric detection of the MLBB extension to the surface was verified by an observed abrupt transition of mPING surface precipitation types. Rain was predominant to the south of the transition line, over the southern coast of Long Island, while a narrow zone of freezing rain and ice pellets was positioned along the line, over the central and northern regions of Long Island, with snow predominant to the north (Figs. 2.2b, 2.12d, 2.13d, and 2.14d). After the dissipation of the polarimetric signature, the region of freezing rain and ice pellets shifted slightly southward (Figs. 2.2c,d). Meteorologists and cooperative observers from the NWS Forecast Office in Upton reported a finer temporal resolution of a transition of precipitation type to sleet along the transition line. Therefore, considering the transition line corresponded well with these ice pellet reports, there potentially may have been some contribution of wet growth and melting of refrozen hydrometeors in addition to the melting effects of the downward extension of the MLBB.

d. Depositional growth layer

An elevated horizontal layer of enhanced Z_{DR}, K_{DP}, and reduced ρ_{hv} was observed above the melting layer, within the comma-head region of the cyclone. The enhanced Z_{DR} likely signified rapid depositional growth of large, horizontally oriented ice crystals in the subfreezing temperatures aloft. Further aggregation of large ice crystals causes a decrease of Z_{DR} below. Figure 2.15 illustrates this intriguing feature along the 0° azimuth at 0305 UTC 9 February 2013. Enhanced Z_{DR} (1–3 dB) and K_{DP} (up to 2° km^{-1}) and reduced ρ_{hv} (as low as 0.9) were observed in a layer above ~3 km, within the model-indicated -12° and

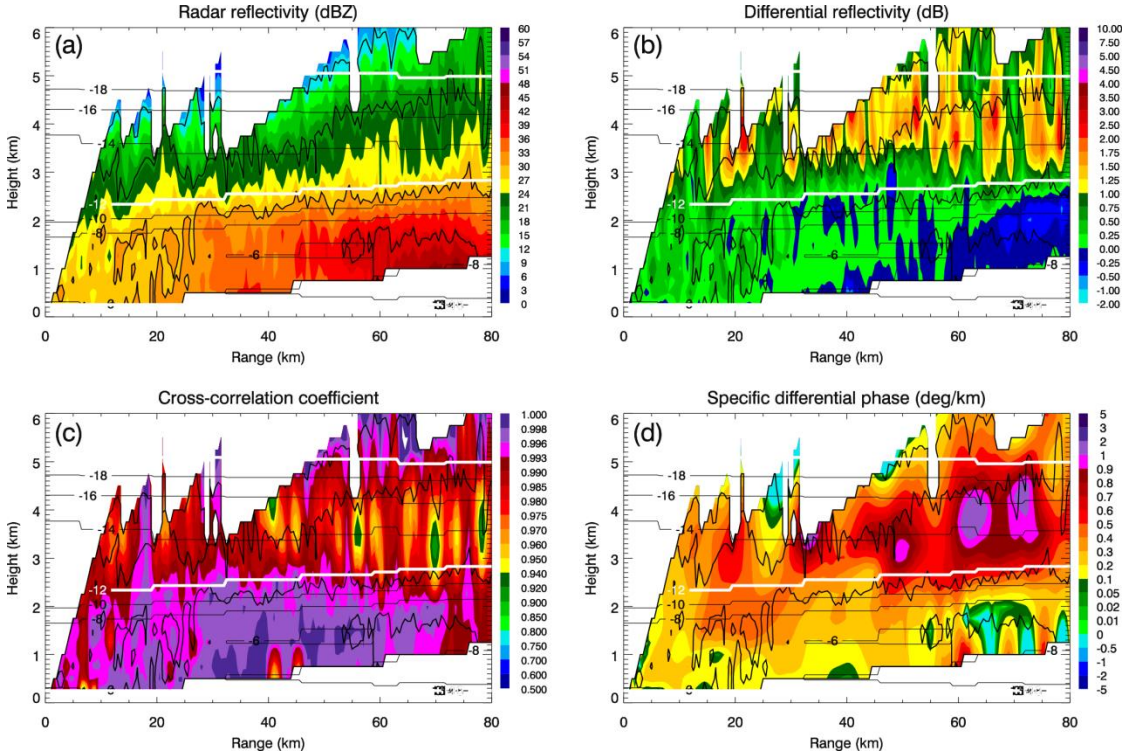

Fig. 2.15: As in Fig. 2.5, but for 0305 UTC 9 Feb 2013 at 0° azimuth. In each RHI, Z_H is contoured at 10, 20, 30, and 40 dBZ. Contours of RAP model T_W are also overlaid (°C), with the -12° and -20°C contours in white.

-20°C T_W isotherms (Fig. 2.15). The largest K_{DP} values were preferentially located between the -14° and -18°C isotherms and there was a pronounced vertical Z_H gradient directly below the layer, consistent with observations documented by Kennedy and Rutledge (2011), Andrić et al. (2013), and Bechini et al. (2013). Also at this time, Z_H near the surface exceeded 50 dBZ, while exceptionally heavy snow (fine, low-density snow with little rime) was found at the surface by observers at the NWS Forecast Office in Upton.

The depositional growth layer was first observed after 1200 UTC, as much as 10 h prior to the greatest Z_H values near the surface and when large Z_H values were most widespread. As time progressed, and as Z_H exceeded 50 dBZ near the surface, the layer became more evident and occurred above the regions of large Z_H. By 2100 UTC, the layer had become yet more evident (particularly in terms of K_{DP}) as Z_H further increased in the heavy snowband and as colder and drier air was introduced near the surface. This layer was particularly apparent in the PPI plots above the 6°-elevation scans. Figure 2.16 (2106 UTC) displays a striking example of double rings of enhanced Z_{DR}, reduced ρ_{hv}, and slightly enhanced K_{DP} encircling KOKX; the outer ring indicates the depositional growth layer (between approximately -12° and -20°C), while the inner ring indicates the MLBB. The depositional growth layer occurred at greater heights southeast of KOKX, where temperatures were warmer at the surface, while the layer occurred at lower heights northwest of KOKX, above colder surface temperatures. At this time, mPING surface precipitation type reports indicate snow, wet snow, and ice pellets. Also at this time, and during the following hour, cooperative observers from the NWS office in Upton reported

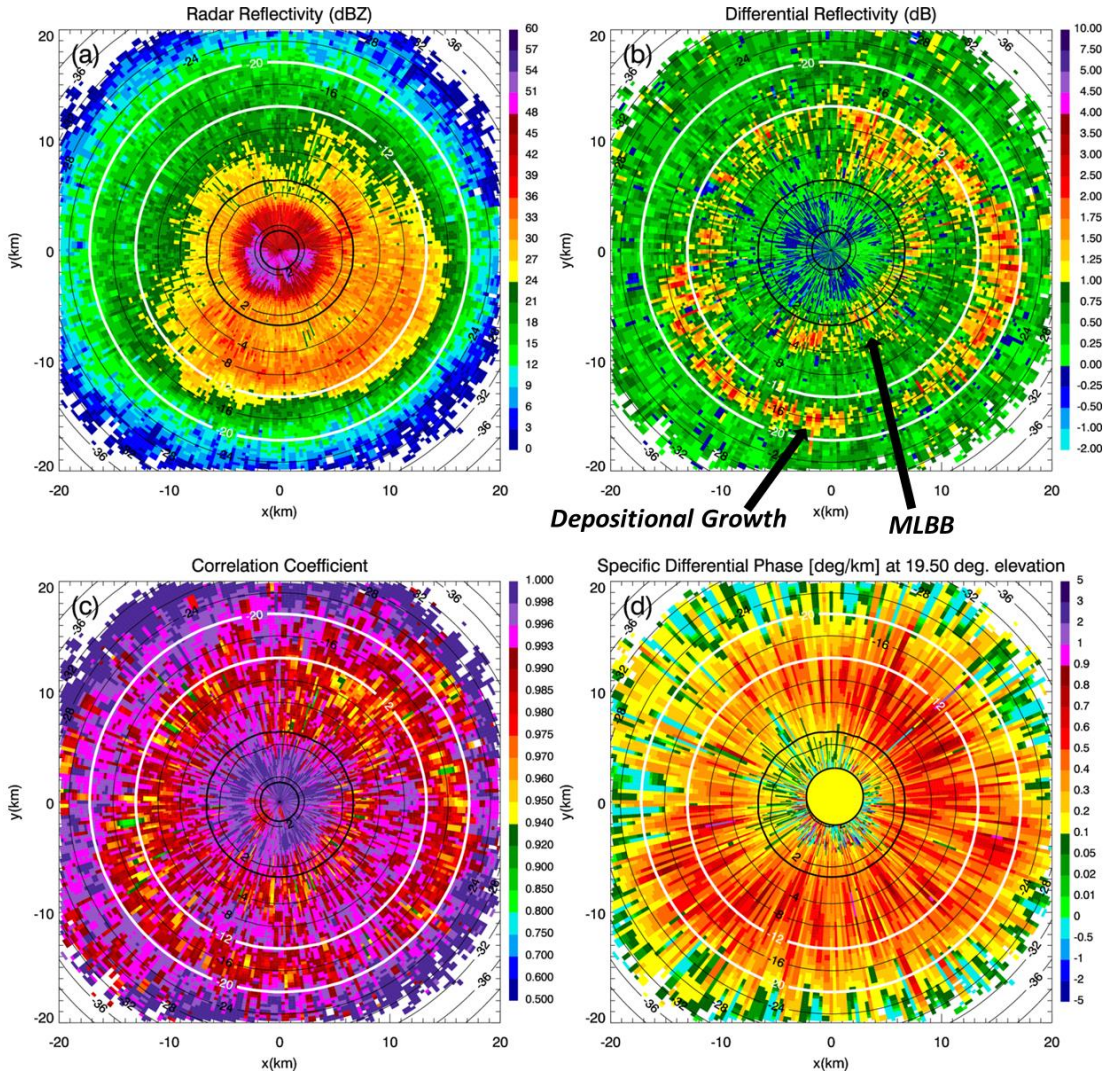

Fig. 2.16: PPIs at 2106 UTC 8 Feb 2013 of (a) Z_H, (b) Z_{DR}, (c) ρ_{hv}, and (d) K_{DP} at 19.5° elevation. Contours of RAP model T_W on the conical surface are overlaid. The boldface contours represent the 0°C wet-bulb isotherms, while the white contours represent the -12° and -20°C isotherms. Double rings of enhanced Z_{DR}, reduced ρ_{hv}, and slightly enhanced K_{DP} encircle KOKX; the outer ring indicates the depositional growth layer, while the inner ring indicates the MLBB. This signature preceded the rapid increase in Z_H near the surface by less than 1 h.

large dendrites and aggregates within heavy snow along the northern shore. Lightly rimed dendrites were falling at Stony Brook University, as observed by Ganetis et al. (2013) at 0409 UTC. Note that this signature (Fig. 2.16) preceded the rapid increase in Z_H near the

surface (>50 dBZ) by less than 1 h. It was less visible between 2300 and 0100 UTC 9 February 2013, but reappeared and became most distinct from 0100 to 0400 UTC, particularly north of KOKX, above the greatest Z_H values over Connecticut (not shown). The physical explanation for the waning of the layer is not yet clear, but it may have been attributed to the instability being relieved for a short time, before being reinvigorated thereafter.

Overall, it appears the depositional growth layer was associated with an increase in heavy snowfall as ice crystals (likely dendrites) were generated aloft, aggregated, descended, and then contributed to the large Z_H near the surface. The layer appeared increasingly more evident as the period of greatest Z_H values neared, with the initial layer observations preceding the greatest Z_H values near the surface by several hours. Additionally, throughout the event, K_{DP} values of 0.5°–2° km^{-1} and Z_{DR} values of up to approximately 3 dB were persistently observed in the vicinity of the -15°C T_W isotherm and were most enhanced during periods of widespread large Z_H values, bolstering the results of Bechini et al. (2013), who documented peak K_{DP} values of around 2.0° and 3.5° km^{-1} at C and X band, respectively (which would produce values of approximately 1.0° km^{-1}at S band), in the ice region of precipitating clouds. Associated maximum ice water content (IWC) estimated values, obtained by using

$$IWC = \frac{CK_{DP}}{1-\frac{1}{Z_{dr}}}, \tag{2.2}$$

were approximately 1.3 g m^{-3}, where Z_{dr} is in linear scale and $C = \frac{0.42\lambda}{30\pi}$, according to Ryzhkov et al. (1998). In Eq. (2.2), IWC is in grams per cubic meter, K_{DP} is in degrees per kilometer, and the radar wavelength λ is in millimeters. This maximum IWC value conveys the large volume of ice present within the depositional growth zone, associated with the heavy snowfall during the event. The IWC (K_{DP}–Z_{DR}) relation, Eq. (2.2), is valid for nonaggregated or moderately aggregated crystals and for Z_{DR} values higher than about 1 dB. The relation is particularly useful when estimating IWC in dendritic growth regions, where Z_{DR} values can be large. Kennedy and Rutledge (2011) reported maximum S-band K_{DP} and Z_{DR} values of ~0.15°–0.4° km^{-1} and ~1.5 dB, respectively. These values would correspond to an IWC value of approximately 0.8 g m^{-3}, further illustrating that the Northeast blizzard was an extreme winter event.

e. Informative polarimetric artifacts

Several types of artifacts were observed in the polarimetric data. These features should not be overlooked, as they can also provide valuable information about storm microphysical processes (Kumjian 2013c).

1) DEPOLARIZATION STREAKS

Depolarization streaks were observed during the time of heaviest precipitation, when the low-level Z_H was >50dBZ. According to Ryzhkov et al. (2011), weak convective updrafts in winter storms can produce a tangible amount of graupel and charge separation sufficient to generate electric fields. Furthermore, strong electrostatic fields can change the

orientation of ice crystals atop these updrafts, causing the transmitted radar signal to become depolarized (Ryzhkov and Zrnić 2007; Ryzhkov et al. 2011). The resulting polarimetric signatures reveal the depolarization through radial streaks of enhanced positive and/or negative Z_{DR}. Therefore, the numerous depolarization streaks observed during the Northeast blizzard event provided evidence of widespread electrification in the cloud.

Depolarization streaks occurred in the southern comma-head region of the synoptic-scale low pressure system from 2100 through 0300 UTC 9 February 2013, and were most frequent and pronounced during the 2300 UTC hour, when Z_H exceeded 55 dBZ near the surface. The location of these streaks within the system supports the work by Rauber et al. (2014), who documented a climatology of electrification in the comma heads of 16 continental winter cyclones. They found that lightning originated in elevated convective cells within the southern region of the comma head, due to advancement of upper-tropospheric dry air within the dry slot over the low-level moist air. Although beyond the scope of this work, it is possible that a similar mechanism may have been responsible for triggering cloud electrification in the February 2013 Northeast blizzard.

The depolarization streaks were observed at the 0.5°– 9.89°-elevation angles, especially at 1.45°–4.3°, and originated at uncharacteristically low heights (compared to streaks typically observed in warm-season convection) atop convective updrafts in regions of heavy, wet snow. Origination heights (i.e., the heights of the tips of the streaks) ranged from 1 to 5km but were primarily at approximately 3 km, where model-indicated T_W values were from -4° to -6°C. Average origination heights were slightly lower after 0000

UTC, when compared to those prior to 0000 UTC. The PPI image at 2314 UTC (Fig. 2.17) provides an example of the streaks observed during the event. The Z_{DR} imagery displays radial streaks of enhanced positive and negative Z_{DR}, with magnitudes of 5 and 2 dB, respectively. The streaks originated atop convective updrafts in regions of heavy wet snow (Z_H > 50dBZ, ρ_{hv} as low as 0.9) and in the vicinity of a cluster of total lightning flashes detected by the Earth Networks Total Lightning Network (Fig. 2.17). These observations bolster the results of Rauber et al. (2014), who documented that lightning flashes typically occur on the southern side of the comma head, where dry air aloft may overrun low-level moist air and trigger convective instability.

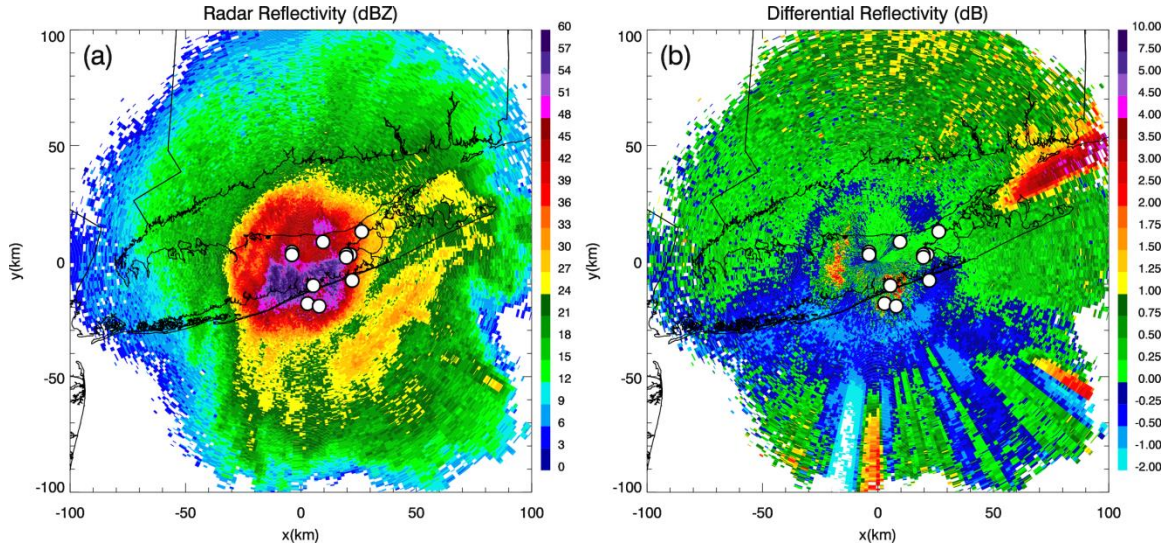

Fig. 2.17: PPIs at 2314 UTC 8 Feb 2013 of (a) Z_H and (b) Z_{DR} at 3.34° elevation. Depolarization streaks are indicated by the radial streaks of positive and negative Z_{DR}. Lightning flash locations at 2316 UTC, from the Earth Networks Total Lightning Network, are indicated by the white circles.

2) NONUNIFORM BEAMFILLING

Another polarimetric artifact observed was nonuniform beamfilling (NBF; Ryzhkov 2007), revealed by a wedge of radial streaks of reduced ρ_{hv} (e.g., Fig. 2.18d). The RHI plots in Fig. 2.5 illustrate the NBF, with ρ_{hv} as low as 0.75 (Fig. 2.5c) and Φ_{DP} as large as 95° (not shown). The wedge of low ρ_{hv} indicated large vertical gradients of Φ_{DP}, due to a nonuniform mixture of precipitation types and sizes within the radar beam cross sections. Here, the diverse precipitation types were likely heavy wet snow and dry snow, heavy sleet, and wet-growth ice hydrometeors (Ganetis et al. 2013; Picca et al. 2014). Furthermore, progressive beam broadening enhanced the impact of NBF with increasing range from the radar. Significant accumulation of Φ_{DP} down the radial provided further evidence of the melting of large aggregates and other larger ice hydrometeors (i.e., graupel, large hail-like ice pellets) near the surface.

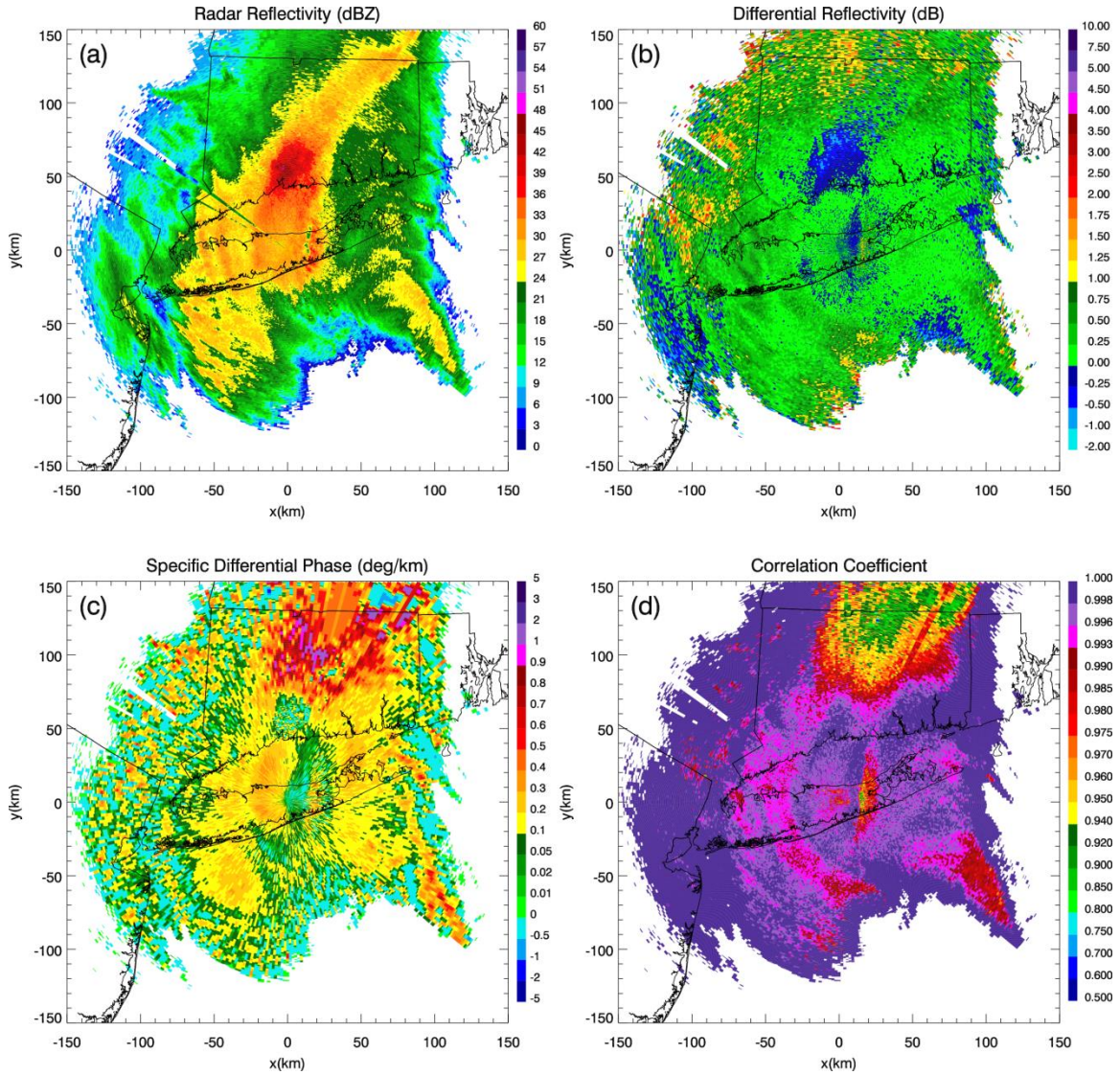

Fig. 2.18: As in Fig. 2.9, but for 0259 UTC 9 Feb 2013. NBF was indicated by the wedge of radial streaks of reduced ρ_{hv}.

3) A "SNOW FLARE" SIGNATURE

An interesting "snow flare" signature, reminiscent of a hail three-body scatter signature, was observed northeast of KOKX from 0000 to 0200 UTC 9 February at the 6°–19.5°-elevation scans, revealed by enhanced values of Z_{DR} and reduced ρ_{hv}, collocated with low Z_H and K_{DP} (e.g., Fig. 2.19). The signature flared outward from the radar and

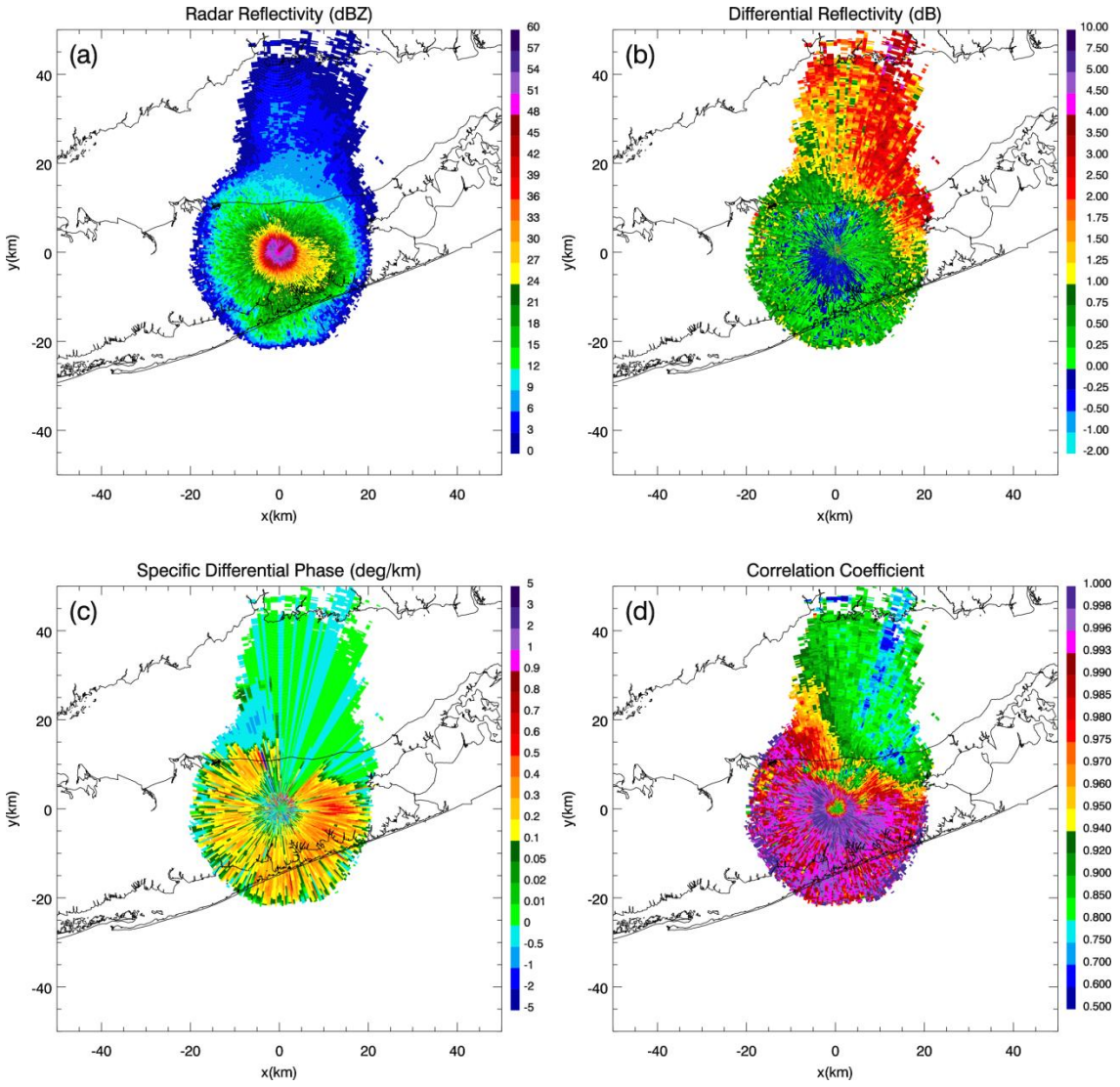

Fig. 2.19: PPIs at 0108 UTC 9 Feb 2013 of (a) Z_H, (b) Z_{DR}, (c) K_{DP}, and (d) ρ_{hv} at 19.5° elevation. The snow flare was revealed by enhanced values of Z_{DR} and reduced ρ_{hv}, collocated with low Z_H and K_{DP}, flaring outward from KOKX. This artificial signature was associated with very large snowflakes, ice pellets, and anomalous hail-like ice hydrometeors (or asteroid ice) at the surface.

appeared similar to a three-body scattering signature (or hail flare) that is frequently associated with the presence of hailstones (e.g., Zrnić 1987; Hubbert and Bringi 2000; Kumjian et al. 2010; Zrnić et al. 2010; Picca and Ryzhkov 2012). However, in this case, the signature appears to have been associated with very large snowflakes and wet-growth

ice hydrometeors. The flare occurred coincident with surface observations of snow and ice pellets in the mPING data. However, it also occurred at the same time that Ganetis et al. (2013) reported the presence of hail-like large ice pellets (or asteroid ice). The coincidental occurrence of asteroid ice with the formation of the snow flare supports that its growth process is analogous to that of hail. However, detailed analysis of RHIs in different azimuthal directions shows that strong sidelobe contamination should not be excluded as a possible source of the snow flare. As the flare began to appear less distinct, wet-growth ice hydrometeors were on a downward trend, with a decreasing density of rimed snow from the NWS Forecast Office in Upton toward the northern shore. During the hour following the disappearance of this signature, heavy, much less dense snow (with some aggregates) was observed at the Forecast Office in Upton and surrounding areas, while there was a rapid decrease in sleet, graupel, and heavily rimed snow.

4. Summary and conclusions

The 8–9 February 2013 Northeast blizzard was a unique event, exhibiting several intriguing dual-polarization radar signatures. This study investigates the evolution and nature of these signatures, and the thermodynamic conditions within which they developed, to obtain a better understanding of the fundamental microphysical processes within this system. Polarimetric data (from the S-band KOKX radar) were analyzed alongside RAP model wet-bulb temperature analyses, as well as surface precipitation type observations from both mPING and the NWS Forecast Office in Upton, New York, for interpretation of polarimetric signatures.

Values of Z_H during this event were extraordinary for a winter storm, exceeding 50 dBZ and reaching as high as 60 dBZ within a shallow layer just above the surface. Also, as the incoming snowbands proceeded northward, the polarimetric data exhibited an exceptionally distinct transition from frozen to unfrozen precipitation, providing detail that was often unmatched by the numerical model output. During this event, the polarimetric observations were critical for accurately assigning the transition from liquid to frozen precipitation, illustrating how dual-polarization radar data could be a potentially valuable tool for forecasters when nowcasting transitional winter precipitation. Another prominent feature of the event was the remarkable differential attenuation, resulting from the radar beam propagating through regions of heavy wet snow and mixed-phase precipitation. These differential attenuation observations reached magnitudes that exceed anything previously documented for S-band radar observations in snow. This study also documents a downward excursion of the MLBB to the surface, characterized by reduced ρ_{hv} and locally maximized Z_H and Z_{DR}; this feature was correlated with an abrupt transition line of precipitation types at the surface.

Some of the most distinctive signatures observed during the event were elevated horizontal layers of enhanced Z_{DR} and K_{DP}, and reduced ρ_{hv}, located above the environmental freezing layer and within the commahead region of the cyclone. The enhanced Z_{DR} values likely signified the presence of large, horizontally oriented ice crystals at the subfreezing temperatures aloft, near the model-predicted -15°C T_W isotherm, where the conditions for rapid depositional growth are most favorable. These depositional growth layers appeared to be correlated with the increase in heavy snowfall; ice crystals

were generated aloft, aggregated, descended, and then contributed to the large Z_H values near the surface. The layers appeared increasingly more evident as the period of greatest Z_H values neared, with the initial layer observations preceding the greatest surface Z_H by several hours, demonstrating the potential utility of this signature for nowcasting increases in precipitation at the surface.

Several polarimetric artifacts were also observed and provided valuable information about the system's microphysical processes. Distinct depolarization streaks occurred with frequency during the 2300 UTC hour, when Z_H exceeded 55 dBZ near the surface. These radial streaks of positive and negative Z_{DR} indicated regions of atmospheric electrification (and possible regions of supercooled water), and they originated at uncharacteristically low heights, atop weak convective updrafts in regions of heavy wet snow. The effects of nonuniform beamfilling were also observed during the event, indicating large gradients of Φ_{DP} within the radar resolution volume, due to a nonuniform mixture of precipitation types and sizes within the radar beam cross sections. Finally, a "snow flare" of reduced ρ_{hv}, enhanced Z_{DR}, moderate K_{DP}, and low Z_H flared outward from the radar and appeared similar to a three-body scattering signature commonly reported in hailstorms; this signature could also be due to sidelobe contamination. This feature was associated with very large snowflakes and ice hydrometeors at the surface, including anomalous ice hydrometeors (Ganetis et al. 2013), which had the appearance of small, irregular hailstones.

This study provides a next step toward understanding the fundamental microphysical processes within winter precipitation and how polarimetric signatures relate

to larger-scale storm structure and evolution. The radar signatures investigated herein convey the value of polarimetry in identifying features undetectable in conventional radar data. These signatures are associated with hazardous winter weather conditions that cause havoc on the public and transportation sectors, both at the surface and in the air. Therefore, polarimetry provides a valuable tool for short-term detection and prediction of winter weather precipitation types, especially transitional events.

Chapter 3: A Polarimetric Analysis of Ice Microphysical Processes in Snow, Using Quasi-Vertical Profiles

Material in this chapter is from Griffin et al. (2018).

Abstract

This study implements a new quasi-vertical profile (QVP) methodology to investigate the microphysical evolution and significance of intriguing winter polarimetric signatures and their statistical correlations. QVPs of transitional stratiform and pure snow precipitation are analyzed using WSR-88D S-band data, alongside their corresponding environmental thermodynamic High-Resolution Rapid Refresh model analyses. QVPs of K_{DP} and Z_{DR} are implemented to demonstrate their value in interpreting elevated ice processes. Several fascinating and repetitive signatures are observed in the QVPs for differential reflectivity Z_{DR} and specific differential phase K_{DP}, in the dendritic growth layer (DGL), and at the tops of clouds. The most striking feature is maximum Z_{DR} (up to 6 dB) in the DGL occurring near the -10-dBZ Z_H contour within low K_{DP} and during shallower and warmer cloud tops. Conversely, maximum K_{DP} (up to 0.3° km^{-1}) in the DGL occurs within low Z_{DR} and during taller and colder cloud tops. Essentially, Z_{DR} and K_{DP} in the DGL are anticorrelated and strongly depend on cloud-top temperature. Analyses also show correlations indicating larger Z_{DR} within lower Z_H in the DGL and larger K_{DP} within greater Z_H in the DGL. The high-Z_{DR} regions are likely dominated by growth of a mixture of highly oblate dendrites and/or hexagonal plates, or prolate needles. Regions of high K_{DP} are expected to be overwhelmed with snow aggregates and crystals with irregular or nearly spherical shapes, seeded at cloud tops. Furthermore, QVP indications of hexagonal plate

crystals within the DGL are verified using in situ microphysical measurements, demonstrating the reliability of QVPs in evaluating ice microphysics in upper regions of winter clouds.

1. Introduction

Polarimetric precipitation observations provide valuable information on the physical characteristics of hydrometeors (e.g., Herzegh and Jameson 1992; Doviak and Zrnić 1993; Zrnić and Ryzhkov 1999; Kumjian 2013a,b,c). Therefore, dual-polarization radar data plays a key role in advancing the understanding of microphysical processes and the nucleation and evolution of ice particles as they fall through a cloud. This will ultimately improve the representation of ice crystal properties in future cloud microphysical models.

Specific differential phase (K_{DP}) observations in winter precipitation are particularly valuable for assessing ice content in the upper levels of clouds (e.g., Vivekanandan et al. 1994; Ryzhkov et al. 1998; Kennedy and Rutledge 2011). The most pronounced polarimetric radar signatures occur in the dendritic growth layer (DGL; i.e., between -10° and -20°C) and at the tops of clouds, while aggregation and riming processes dissolve prominent differential reflectivity (Z_{DR}) signatures below. Intriguing Z_{DR} and K_{DP} signatures above the melting layer (ML) have been documented in previous studies, demonstrating polarimetric indications of dendrites and plate-like ice crystals in the DGL (e.g., Ryzhkov and Zrnić 1998; Ryzhkov et al. 1998; Wolde and Vali 2001; Kennedy and Rutledge 2011; Bechini et al. 2013; Andrić et al. 2013; Griffin et al. 2014; Williams et al.

2015; Schrom et al. 2015; Kumjian and Lombardo 2017), and a variety of ice habits generated as primary ice at the top of clouds, for example, in generating cells (e.g., Kumjian et al. 2014).

Ryzhkov et al. (1998) documented a pronounced elevated region of high K_{DP}, centered at a height of 6 km, within a trailing precipitation region of a squall line, and Ryzhkov and Zrnić (1998) found peak K_{DP} of 0.35° km^{-1} at S band at 5 km, in a warm snow storm that contained heavily aggregated snow. Later, Kennedy and Rutledge (2011) reported on S-band measurements of an elevated layer of K_{DP} in four Colorado winter storms that had local maxima of ~0.15°–0.4° km^{-1} near the -15°C isotherm. They further showed that the passage of these regions was associated with an increase in surface precipitation. Calculations using an electromagnetic scattering model indicated that highly oblate spheroidal particles with diameters between ~0.8 and 1.2 mm in range and moderate ice densities produced K_{DP} values that were consistent with radar observations. Their calculations were unable to reproduce Z_{DR}, however. They further concluded that the persistent collocation of this signature with the -15°C isotherm was an indication that rapidly growing dendrites likely played a significant role in producing the elevated K_{DP} signature. In another study of winter storms, Andrić et al. (2013) reported on isolated pockets of enhanced K_{DP} and Z_{DR} that were collocated with reduced cross-correlation coefficient (ρ_{hv}). These signatures were also found to be located at temperatures between -10° and -15°C, and were coincident with a zone of large radar reflectivity vertical gradient, with reflectivity factor Z_H increasing toward the ground. Using a simple kinematical, one-dimensional, two-moment bulk microphysical model that was coupled with an

electromagnetic scattering model, Andrić et al. (2013) were able to approximately reproduce the correct profile types of vertical dependencies and magnitudes of Z_H and ρ_{hv} and the correct profiles (but not magnitudes) of Z_{DR} and K_{DP}. They concluded that their inability to reproduce the correct profiles and magnitudes of all of the signatures indicated that microphysical processes not included in the model, such as secondary ice production, were likely important factors in producing the observed signature. Bechini et al. (2013) also documented enhanced Z_{DR} and K_{DP} values near the model-indicated -15°C isotherm in the ice region of precipitating clouds, using C- and X-band radars in northwestern Italy. They found that these regions of enhancement (K_{DP} values peaked at around 2.0° km^{-1} at C band) were likely associated with dendritic growth and were correlated with the Z_H below. Furthermore, Griffin et al. (2014) observed that DGLs near the model-predicted -15°C isotherm were correlated with increased snowfall and large Z_H near the surface in a historic northeastern blizzard, bolstering the results of Bechini et al. (2013), Andrić et al. (2013), and Kennedy and Rutledge (2011).

In a more recent study, Schrom et al. (2015) documented X-band observations of these enhanced K_{DP} signatures near -15°C, with Z_{DR} decreasing and Z_H increasing toward the ground (indicating aggregation or riming), within several Colorado winter storms. They retrieved particle size distributions of dendrites and plates, demonstrating that enhancements in Z_{DR} can likely indicate both plates and dendrites. Similarly, Wolde and Vali (2001) reported hexagonal plates, stellars, and dendrites occurring within large Z_{DR} near the -15°C isotherm. To help identify regions of likely icing hazards, Williams et al. (2015) identified two categories of enhanced Z_{DR} in winter and summer stratiform systems.

In one category, Z_{DR} between 0 and 3 dB occur in larger Z_H (i.e., 10–30 dBZ) when dendrites are present among supercooled water and water-saturated environments, at temperatures between -10° and -20°C. They described how this region can potentially produce hazardous icing conditions for aircraft. In their second category, flat-plate and dendritic crystals are associated with Z_{DR} between 3 and 7 dB, in areas of lower Z_H (i.e., from -10 to 10 dBZ) near the tops of clouds. In this region, they found evidence of diffusional growth of the high aspect- ratio ice crystals, within minimal or absent amounts of supercooled water, therefore posing no icing hazards. From a different perspective, Moisseev et al. (2015) suggested that layers of K_{DP} near the -15°C isotherm can rather be attributed to the onset of aggregation, occurring within high concentrations of ice, because of a seeder–feeder process. They also proposed that when layers of enhanced Z_{DR} occur near the -15°C isotherm within minimal K_{DP}, and within low concentrations of ice, crystal growth is likely to be the main microphysical process, explaining why layers of maximum K_{DP} and Z_{DR} may not always be temporally collocated. Additionally, Kumjian and Lombardo (2017) documented that layers of enhanced K_{DP} are correlated with greater radar-inferred ascent near the -15°C isotherm, and that enhanced K_{DP} occurs more often in regions of greater supersaturations, with increased Z_H and heavier snowfall near the surface. Overall, these studies have established important building blocks toward a more thorough understanding of these polarimetric signatures and their implications, however, more polarimetric and in situ analyses are needed to better diagnose the ice processes that govern the evolution of winter clouds and precipitation.

Recently, a new method of processing and displaying polarimetric radar data has been developed, providing an opportunity to better elucidate ice microphysical processes and their temporal evolution. Ryzhkov et al. (2016) introduced a quasi-vertical profile (QVP) methodology in which Z_H, Z_{DR}, ρ_{hv}, and differential phase Φ_{DP} from weather surveillance radars are azimuthally averaged at relatively high antenna elevation angles exceeding 10°–20°. Use of these high elevation angles reduces the effects of beam broadening and horizontal inhomogeneity (Ryzhkov et al. 2016). The resulting QVPs display the polarimetric variables in a convenient time-versus-height format, which allows for efficient investigation of key cloud microphysical processes. Ryzhkov et al. (2016) documented QVP examples to demonstrate advantages of the QVP technique, including the ability to compare polarimetric WSR-88D data with data from vertically looking remote sensors (e.g., wind profilers, lidars, and cloud radars), to continuously monitor the ML and DGL with high vertical resolution, and to potentially discriminate between rimed and aggregated snow. The QVP methodology has quickly become popular and has now been implemented by Kumjian and Lombardo (2017), who demonstrate the value of QVPs for providing knowledge on the microphysical and kinematic structures of Northeast winter storms. They are also the first to directly relate kinematic and microphysical information in winter storms, using WSR-88D QVPs of Doppler velocity and polarimetric variables, including K_{DP}, to infer regions of mesoscale ascent.

Since January of 2013, we have compiled a database that consists of thousands of hours of polarimetric WSR-88D observations in a wide variety of winter precipitation events. Many of those datasets exhibit several intriguing, repetitive, and previously

undocumented polarimetric signatures. In this chapter, we use QVPs produced from a few select events obtained from that database to investigate the microphysical evolution and significance of some of those. Radar data and their microphysical interpretation are presented in context of the thermodynamic environment provided by a numerical model with data extracted from the QVPs, to document statistical correlations between cloud-top temperature (CTT) and K_{DP} and Z_{DR} in the DGL between -10° and -20°C.

2. QVP Methodology

QVPs provide an unprecedented look into the microphysical processes within winter storms and are an efficient way to process and analyze polarimetric WSR-88D data. This investigation builds on the work of Ryzhkov et al. (2016) by demonstrating the value of using QVPs of K_{DP} and Z_{DR} to examine the temporal evolution of ice microphysical processes in winter clouds and precipitation. The K_{DP} signatures contain important information about ice microphysics aloft and are particularly useful for the quantification of ice. Ryzhkov et al. (1998) documented two methods of ice water content (IWC) estimation that define IWC either as a function of K_{DP} and Z_{DR}, or as a function of K_{DP}. The IWC–K_{DP}–Z_{DR} algorithm is particularly useful when estimating IWC in DGLs, where Z_{DR} can be large, and the IWC–K_{DP} algorithm is applicable for regions of low Z_{DR}. They found the polarimetric methods outperform the conventional IWC–Z_H methods. Accordingly, there is ample potential for K_{DP} and Z_{DR} measurements to improve upon existing radar-based techniques to estimate IWC in snow.

The QVP methodology, described in Ryzhkov et al. (2016), assumes a certain degree of horizontal homogeneity of the atmosphere, particularly at higher altitudes (Table 3.1). Kaltenboeck and Ryzhkov (2017) demonstrated that the horizontal resolution of QVPs retrieved from data collected at antenna tilts of 10°–20° is sufficient to monitor the passage of mesoscale frontal boundaries associated with cold season transitional events. It should also be noted that in the QVP methodology, the averaging does not include azimuths that contain no data.

Table 3.1: Horizontal and vertical resolutions of QVPs at two different antenna elevations (i.e., 10° and 20°) and two heights above ground (H), indicating resolutions near the ML (H = 3 km) and near the top of the cloud (H = 8 km).

	Horizontal resolution		Vertical resolution		
Elev	H = 3 km	H = 8 km	H = 3 km	H = 8 km	Min height
10°	34 km	91 km	0.30 km	0.79 km	0.35 km
20°	16.5 km	44 km	0.14 km	0.38 km	0.68 km

The procedure for generating QVPs of K_{DP}, however, was not specified in Ryzhkov et al. (2016) and requires explanation herein. Radial profiles of Φ_{DP} at each azimuth are used to generate radial profiles of K_{DP} as described elsewhere (e.g., Ryzhkov et al. 2005). Then, QVPs of K_{DP} are obtained by azimuthal averaging of radial K_{DP} profiles produced at each azimuth. The estimation of K_{DP} does not pose any problem for pure snow events but requires special processing in stratiform rain with bright bands because of strong contribution of the backscatter differential phase δ to the total differential phase Φ_{DP} in the ML (Trömel et al. 2014). Large δ (up to 80° at S band) is clearly exhibited in the QVP of Φ_{DP} (Ryzhkov et al. 2016; Fig. 3.1a) and has to be taken into account in the processing of

K_{DP} in each individual radial. We use the following routine to avoid δ contamination in the estimation of K_{DP}. A radial profile of Φ_{DP} along a single ray is characterized by enhanced noisiness at range gates corresponding to the ML due to a sharp drop in ρ_{hv} (Fig. 3.1b). Two criteria are used to recognize these range gates: ρ_{hv} is less than 0.9 and the texture parameter of Φ_{DP} [SD(Φ_{DP})] is higher than 10°. Noisy values of Φ_{DP} associated with the ML are removed from the raw Φ_{DP} data and replaced by an interpolation line connecting valid (i.e., noncontaminated) values of Φ_{DP} between the gates below and above the ML, as shown in Fig. 3.1b. The modified profile of Φ_{DP} is then used to compute K_{DP} that is not contaminated by the contribution from the backscatter differential phase. This

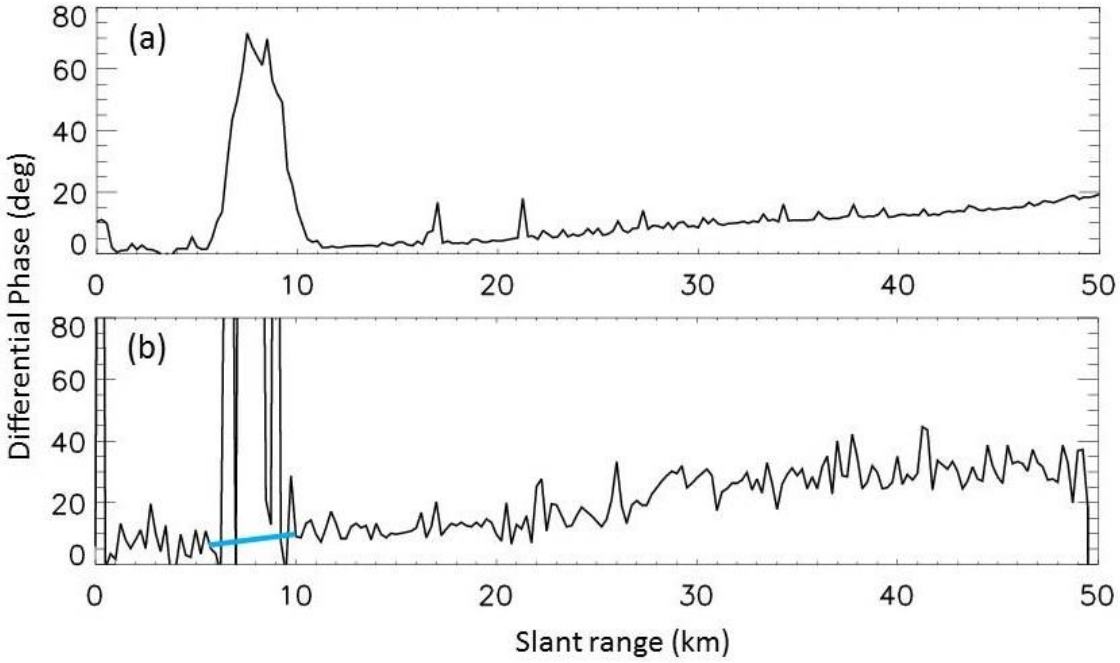

Fig. 3.1: Slant range vs (a) QVP of Φ_{DP} and (b) Φ_{DP} along the 220° radial, for KDGX QVP data from 0252 through 0257 UTC 12 Feb 2014, at 10° elevation. The blue-highlighted line represents the interpolated values of Φ_{DP} between the gates below and above the ML.

method also allows for roughly estimating "net" K_{DP} within the ML as a slope of the interpolation line in Fig. 3.1.

QVP results are dependent on the choice of antenna elevation angle. Theoretical dependencies of Z_{DR} and K_{DP} on elevation angle θ for oblate spheroidal hydrometeors are represented by the formulas

$$Z_{dr}(\theta) \approx \frac{Z_{dr}(0)}{\left[Z_{dr}^{1/2}(0)sin^2\theta+cos^2\theta\right]^2} \quad \text{and} \tag{3.1}$$

$$K_{DP}(\theta) \approx K_{DP}(0)cos^2\theta. \tag{3.2}$$

In Eq. (3.1), $Z_{dr}(0)$ and $Z_{dr}(\theta)$ represent linear scale differential reflectivities at elevation angles 0° and θ°, respectively (Ryzhkov et al. 2005, 2016). In Eq. (3.2), $K_{DP}(0)$ and $K_{DP}(\theta)$ represent K_{DP} at elevation angles 0° and θ°, respectively. According to Eqs. (3.1) and (3.2), the elevation dependencies of Z_{DR} and K_{DP} are relatively weak in the range of elevation angles between 10° and 20°, as illustrated in Fig. 3.2 where QVPs generated at elevations 9.9° and 19.5° are compared. The differences between Figs. 3.2a–d and Figs. 3.2e–h are likely more related to differences in the averaging areas at the two elevations, rather than elevation dependencies of Z_{DR} and K_{DP}.

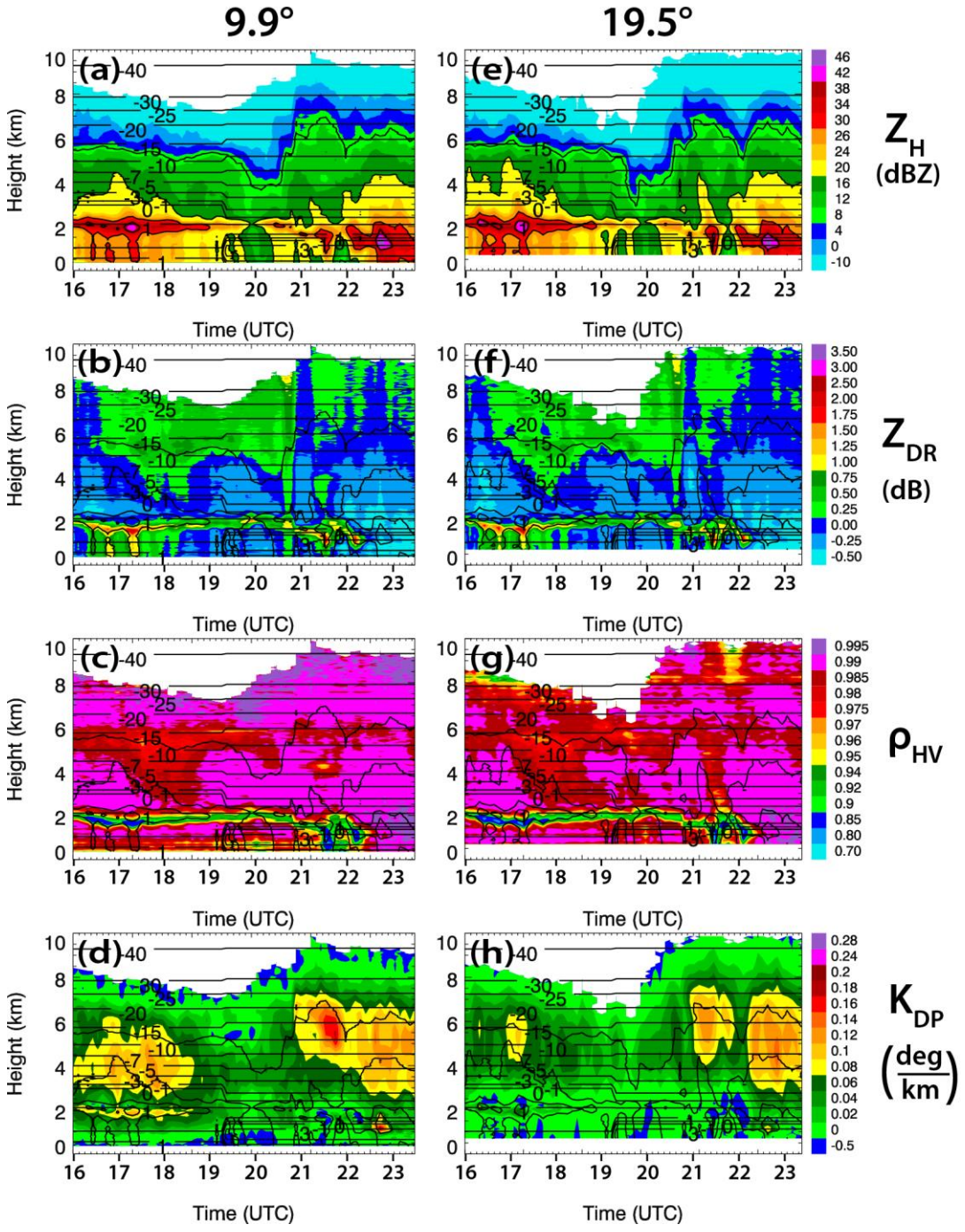

Fig. 3.2: Time-vs-height QVP of (a),(e) Z_H, (b),(f) Z_{DR}, (c),(g) ρ_{hv}, and (d),(h) K_{DP} from KLVX from 1600 through 2328 UTC 4 Mar 2015 at (left) 9.9° and (right) 19.5° elevation angles. Contours of HRRR model wet-bulb temperature (°C) are overlaid in each plot. Also, in each QVP, Z_H is contoured at 10, 20, 30, and 40 dBZ.

3. Data analysis

In this section, QVPs of polarimetric WSR-88D variables at high elevation angles (i.e., 9.9°–19.5°) are presented with their corresponding environmental thermodynamic analyses from the operational 3-km High-Resolution Rapid Refresh (HRRR; Smith et al. 2008; Benjamin et al. 2016) model overlaid. The selection of QVPs at varying elevation angles illustrates that data at 9.9° are just as valuable as those at 19.5°. The model output are used to interpret the polarimetric signatures of ice crystal habits that form at different temperatures, ultimately helping to elucidate the relationship between the polarimetric signatures and ice microphysical processes within winter precipitation. Surface precipitation type observations from 5-min augmented Automated Surface Observing System (ASOS) sites and Meteorological Phenomena Identification Near the Ground (mPING; Elmore et al. 2014) are also used to aid in the interpretation of the approximate 5-min radar observations and provide verification of radar-indicated transitions in precipitation type at the surface.

Here, we present QVPs for five winter precipitation events to explore the evolution and significance of key ice microphysical processes in the upper levels of winter storms. The cases include one pure snow event and four transitional events, three of which occur within the same winter system over the southeastern United States. Though several repetitive signatures are observed, particularly in the Z_{DR} and K_{DP} profiles, this analysis focuses on a newly discovered recurring correlation between CTT (defined as the wet-bulb temperature at the uppermost level for which $Z_H \geq$ -10 dBZ is encountered) with Z_{DR} and K_{DP} signatures in DGLs.

a. KEAX 1 February 2014 winter storm

On 1 February 2014, a transitional winter storm passed over the KEAX WSR-88D (Pleasant Hill, Missouri) producing surface precipitation types that included ice pellets, freezing rain, and snow (mPING and ASOS observations). Figures 3.3a–d depict polarimetric QVPs of Z_H, Z_{DR}, ρ_{hv}, and K_{DP}, at 12.5° elevation from 0353 through 1630 UTC during this event. A distinct ML bright band, as is particularly evident in the ρ_{hv} profile, is indicated from 0546 through 1029 UTC. The most prominent feature in the QVPs, however, is a fascinating layer of enhanced Z_{DR} from 1029 through 1630 UTC that ranges from 1 to >3.5 dB (maximum Z_{DR} of 5.1 dB at ~1600 UTC) between heights of approximately 3 and 5 km. This layer of enhanced Z_{DR} occurs during a period that follows the largest Z_H near the surface, within low Z_H from -10 to -12 dBZ, ρ_{hv} as low as 0.92, and a period during which the cloud-top height drops from approximately 8 km to 5 km. During this period, we believe ice crystals falling out of the upper cloud layer completely sublimate within a midlevel layer of dry air that lies immediately above the layer of high Z_{DR}.

In this study, CTT is defined at the first occurrence of -10 dBZ, beginning at the top of the grid and using a top-down methodology. It should be noted that, because of the presence of the dry layer, this event requires additional criteria for defining cloud top. To extract CTTs for this event (with respect to microphysical analysis of the QVPs), we use a methodology that seeks to find the cloud top that falls immediately below the midlevel layer of dry air. The top-down methodology therefore begins in the midlevel dry layer

where Z_H < -10 dBZ and requires that at least three consecutive (in order to eliminate false tops that might result from additional gaps in the data) levels of $Z_H \geq$ -10 dBZ are

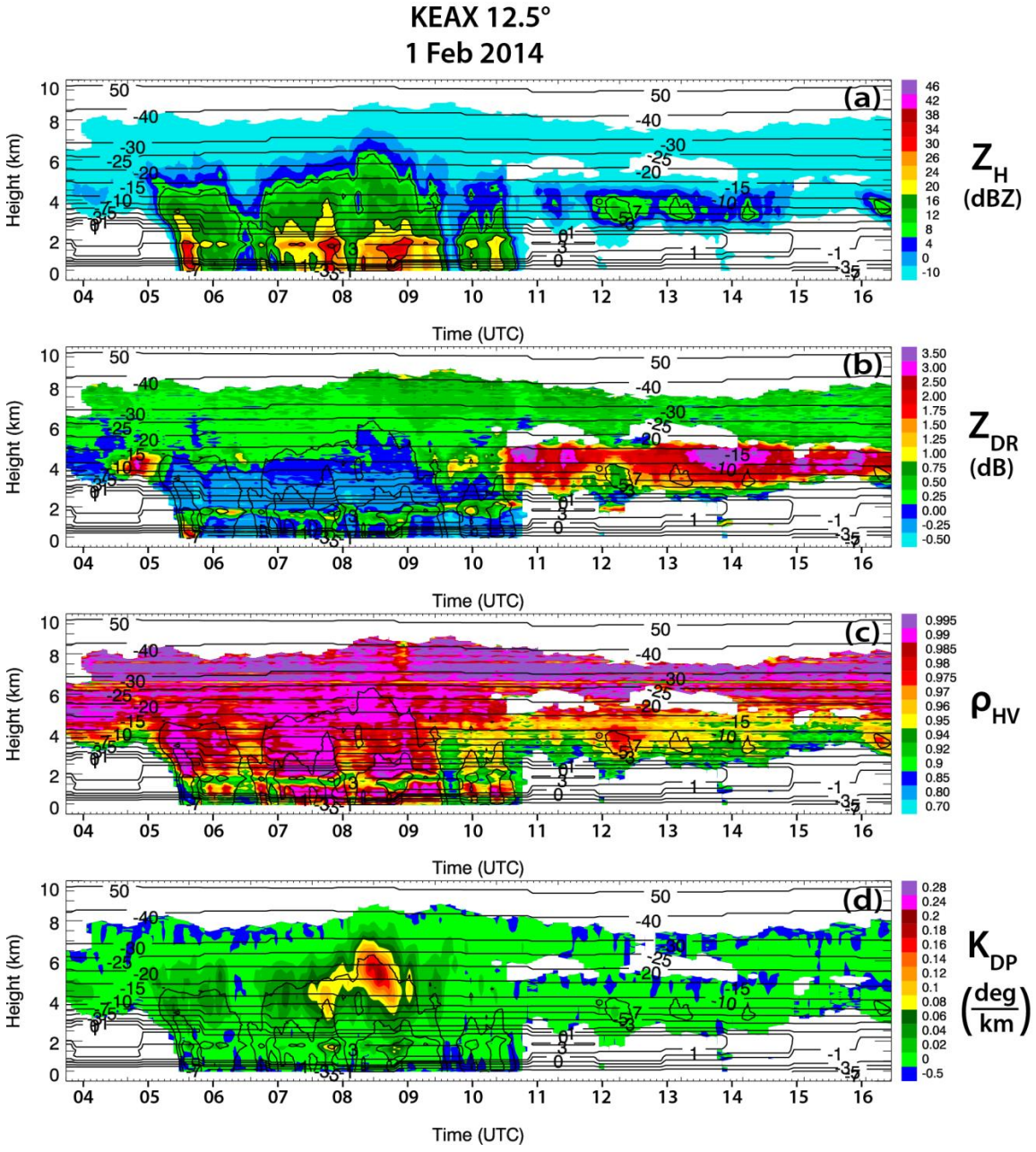

Fig. 3.3: QVPs of (a) Z_H, (b) Z_{DR}, (c) ρ_{hv}, and (d) K_{DP}, for KEAX from 0353 through 1630 UTC 1 Feb 2014, at 12.5° elevation. Contours of HRRR model wet-bulb temperature (°C) are overlaid in each plot. Also, Z_H is contoured at 10, 20, 30, and 40 dBZ.

encountered before a secondary, lower-level cloud top can be defined. Below the dry layer, ice condensation nuclei are likely activated at temperatures between -15° and -20°C in a layer that is saturated with respect to ice, and nearly saturated with respect to water, resulting in the generation of either hexagonal plate crystals or pristine dendrites, depending on humidity, that account for the high Z_{DR} signature.

To better understand the thermodynamic environment responsible for the observed signatures, we present the 1200 UTC 1 February 2014 thermodynamic sounding from Topeka, Kansas (Fig. 3.4), which is located ~120 km west of the KEAX radar. In agreement with the interpretation presented above, this sounding reveals a layer of dry air at temperatures < -20°C and heights between approximately 5 and 7 km. This explains the absence of echo above the DGL in Fig. 3.3 during the period of high Z_{DR}. Immediately below the dry layer, the sounding also indicates a layer that is slightly below water saturation with a mean DGL (indicated by the blue line between the -10° and -20°C isotherms in Fig. 3.4) relative humidity of 88%. Though subsaturated with respect to water, calculations using a first approximation for the saturation vapor pressure of ice $e_i(T) = Ae^{-\frac{B}{T}}$ with A = 3.41 x 10^9 kPa and B = 6.13 x 10^3 K (Rogers and Yau 1989) indicate that this moist layer was supersaturated with respect to ice by as much as 10%. This supports the QVP results and provides quantitative validation that activation and growth of hexagonal plates or dendrites is likely in these ambient conditions.

Another prominent feature in the QVPs in Fig. 3.3 is an anticorrelation between maximum K_{DP} and maximum Z_{DR} in the DGL. Maximum K_{DP} in the DGL peaks at 0.24° km^{-1} just after 0800 UTC, within Z_H between -10 and 20 dBZ and above the largest Z_H

near the surface. It is important to note that the K_{DP} maximum occurs during the period of lowest Z_{DR} in the DGL, and when cloud tops are tallest and coldest (approximately -40°C). Conversely, maximum Z_{DR} in the DGL occurs during the periods of lowest K_{DP} in the DGL and when cloud tops are shallower and warmer (from approximately -15 to -20°C).

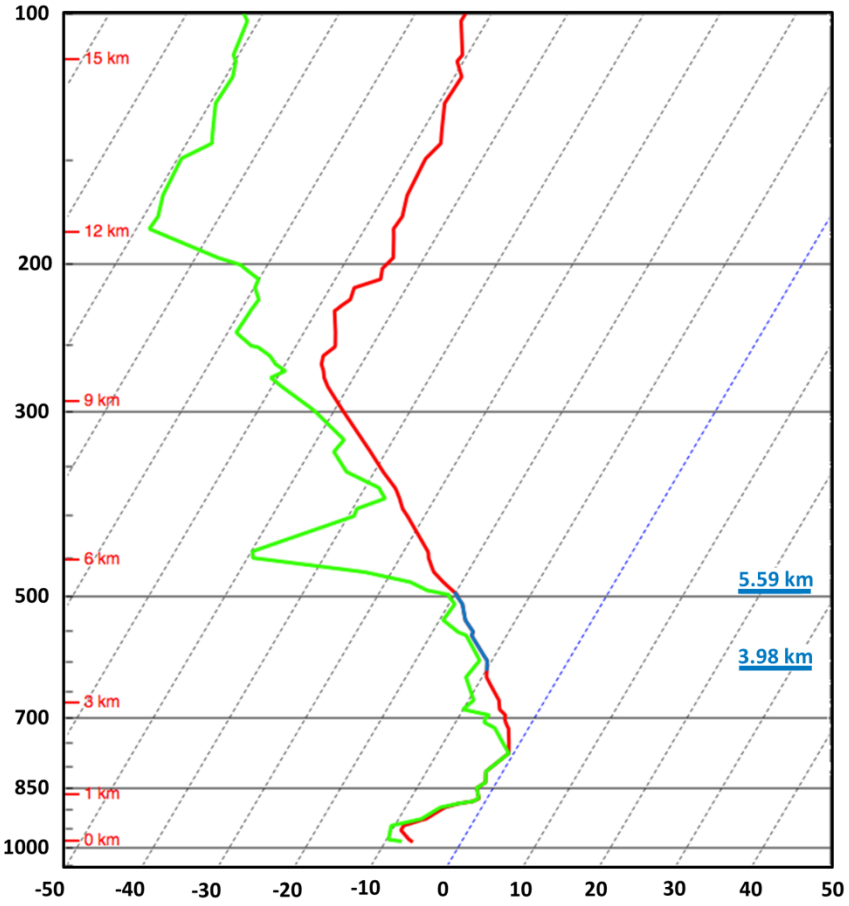

Fig. 3.4: SHARPpy thermodynamic sounding (Blumberg et al. 2017) for Topeka at 1200 UTC 1 Feb 2014, located approximately 120 km from KEAX. The red line represents temperature (°C), the green line represents dewpoint temperature (°C), and the blue solid lines indicate the location of the interpreted DGL (km).

The low K_{DP} is a result of small ice concentrations, while the Z_{DR} of the rapidly growing particles does not depend on concentration. Anisotropic particles must have a sufficient concentration to result in larger K_{DP}. There is also a notable decrease of ρ_{hv} in areas of the

DGL where Z_{DR} is particularly high. This interdependence of Z_{DR} and ρ_{hv} in ice clouds is well known and reported in a number of studies (e.g., Melnikov and Straka 2013). The ρ_{hv} of very anisotropic crystals (such as pristine dendrites, plates, and needles) is usually lower than that of quasi-spherical hydrometeors.

It is important to note that low reflectivities (< 0 or even -10 dBZ) do not indicate low signal-to-noise ratio (SNR), which affects the accuracy of Z_{DR} estimates. Indeed, the WSR-88D is a sensitive radar with minimal Z_H from approximately -10 to -11 dBZ (corresponding to SNR = 0 dB) reliably measured at the distance of 50 km from the radar. Because of the use of high elevation angles (between 10° and 20°) for generating QVPs, slant ranges at which most important polarimetric radar signatures within the DGL are observed are significantly smaller than 50 km, which means the SNR values are well above 0 dB. Additionally, noise powers in the orthogonal H and V channels are measured very accurately at each individual radial following the methodology of Ivic et al. (2013), which allows accurate estimates of Z_{DR} and ρ_{hv} at low SNR.

b. KOKX winter storm (pure snow case): 23 January 2016

Strong K_{DP} signatures are also found in pure snow cases. As an example, we present 19.5°-elevation QVPs from the KOKX (Upton, New York) radar for the Northeast U.S. winter event on 23 January 2016, which produced heavy snow with accumulations up to 50.8 cm (NWS 2016). The precipitation structure of this pure snow case exhibits a different appearance than the transitional event structures. For example, Z_H contours appear more slanted (Fig. 3.5a) and, as expected, there is an absence of a ML signature

(e.g., Fig. 3.5c). As with the KEAX event, maximum K_{DP} in the DGL occurs during the periods of tallest and coldest cloud tops, more specifically from 1020 through 1320 UTC

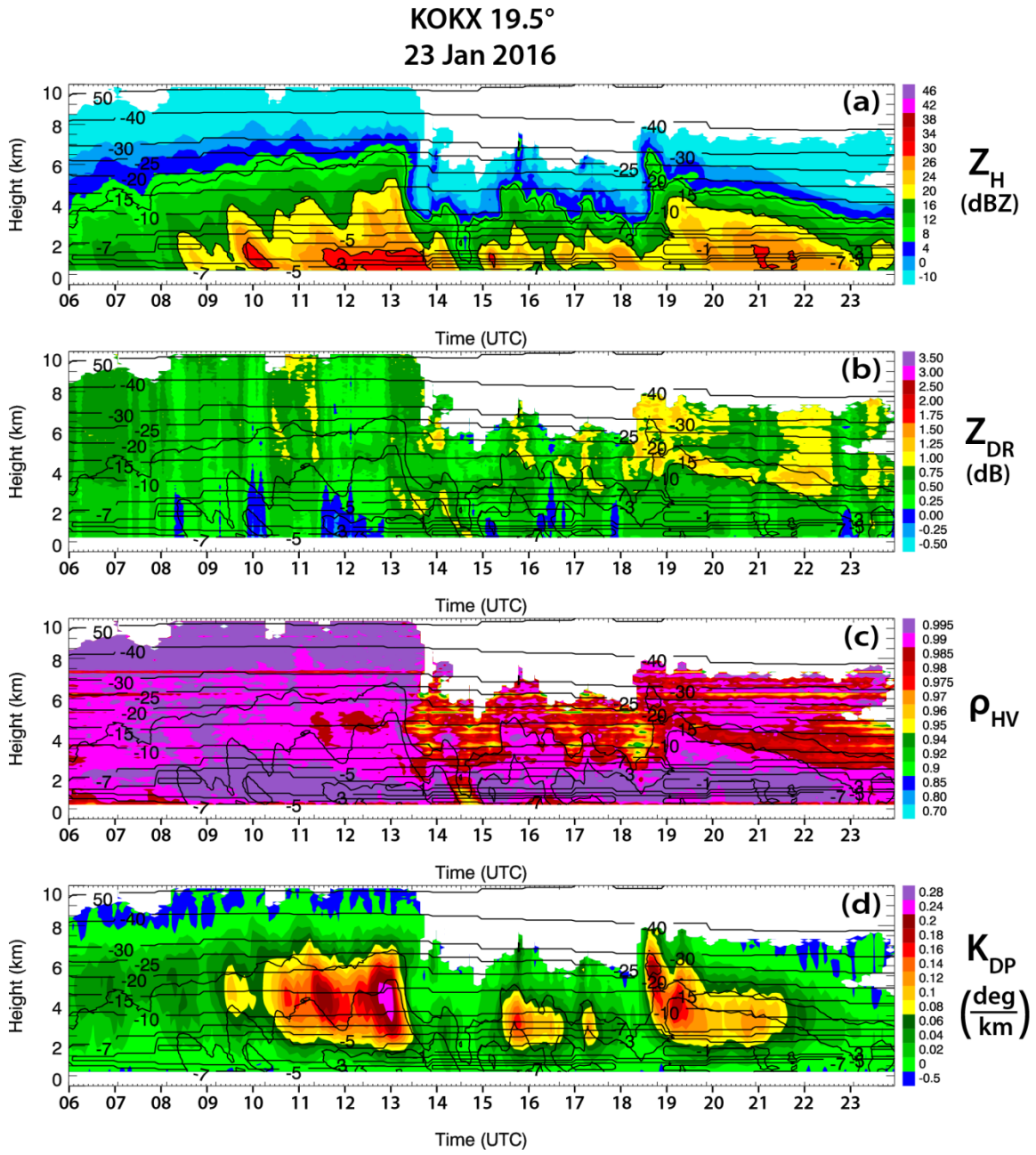

Fig. 3.5: As in Fig. 3.3, but for KOKX from 0600 through 2359 UTC 23 Jan 2016, at 19.5° elevation.

and from 1845 through 2130 UTC, with cloud top up to 10 and 8 km (at -50° and -40°C, respectively; Figs. 3.5a,d). From approximately 1320 through 1830 UTC, cloud tops are shallowest and warmest, at about 6 km and from -20° to -25°C. Moreover, there is no pronounced enhancement of Z_{DR} within the cloud (Fig. 3.5b), while K_{DP} in the DGL is expectedly well pronounced, reaching magnitudes up to 0.29° km^{-1} within the deep snow layer (Fig. 3.5d). These signatures suggest nucleation of pristine ice crystals at cloud top, and a resulting increase in ice concentration below. Although the increase of Z_{DR} in the DGL is not well pronounced during the period of low cloud top from 1320 until 1830 UTC, the drop of ρ_{hv} in the DGL is quite noticeable (Fig. 3.5c), which indicates the presence of very anisotropic ice particles.

c. Southern U.S. winter storm: 11-12 February 2014

This section presents polarimetric QVP results from the perspective of three radars located in the southeastern United States (KGWX, Columbus Air Force Base, Mississippi; KDGX, Jackson, Mississippi; KBMX, Birmingham, Alabama), during a transitional winter storm on 11–12 February 2014 that produced maximum ice and snow accumulations of 2 and 12.7 cm (NWS 2014a), respectively. The system subsequently progressed northeastward up the eastern coast, where it produced further historic ice, snow, and sleet accumulations over the Carolinas. In agreement with previously presented events, each of the three radars exhibit numerous examples of the correlation between CTT with maximum Z_{DR} and K_{DP} in the DGL, thereby providing an example that demonstrates spatial consistency of the polarimetric signatures over a large area within a single winter storm.

1) KGWX 11 FEBRUARY 2014

QVPs for the KGWX radar at 19.5° elevation from 0102 through 1555 UTC 11 February 2014 are presented in Fig. 3.6. A notable excursion of the ML to the surface (Figs. 3.6b,c) from approximately 1000 through 1320 UTC is indicated by enhanced Z_{DR} (as large as 2 dB) and reduced ρ_{hv} (as low as 0.8). The Z_{DR} profile (Fig. 3.6b) illustrates the most dramatic polarimetric signature during this period. From approximately 0700 through 0800 UTC and from 1220 through 1555 UTC, enhanced Z_{DR} from 1 to >3.5 dB is seen in the DGL near the -10°C isotherm, with Z_{DR} maxima of as much as 4.9 dB occurring just after 0700 and 1500 UTC during the periods of warmest and shallowest (as warm as approximately -15°C at 5 km) cloud top (i.e., at $Z_H \geq$ -10 dBZ). The enhanced values are also located within Z_H around -10 dBZ, along the periphery of the detected radar echo. During the periods of maximum DGL Z_{DR}, K_{DP} in the DGL is generally < 0.06° km^{-1}, suggesting low concentrations of ice crystals. This is consistent with relatively low cloud tops, which were mostly below the -30°C isotherm. Also, ρ_{hv} in the DGL ranges from 0.85 to 0.95 (Fig. 3.6c). The common notion that the depression of the cross-correlation coefficient is associated with the diversity of hydrometeor types within the radar resolution volume may not be necessarily applicable to the case of very anisotropic crystals with high Z_{DR} that are characterized by low ρ_{hv}, although it might be only a single habit of ice particles (Melnikov and Straka 2013). The lowest values of ρ_{hv} in DGLs are always associated with the highest values of Z_{DR}.

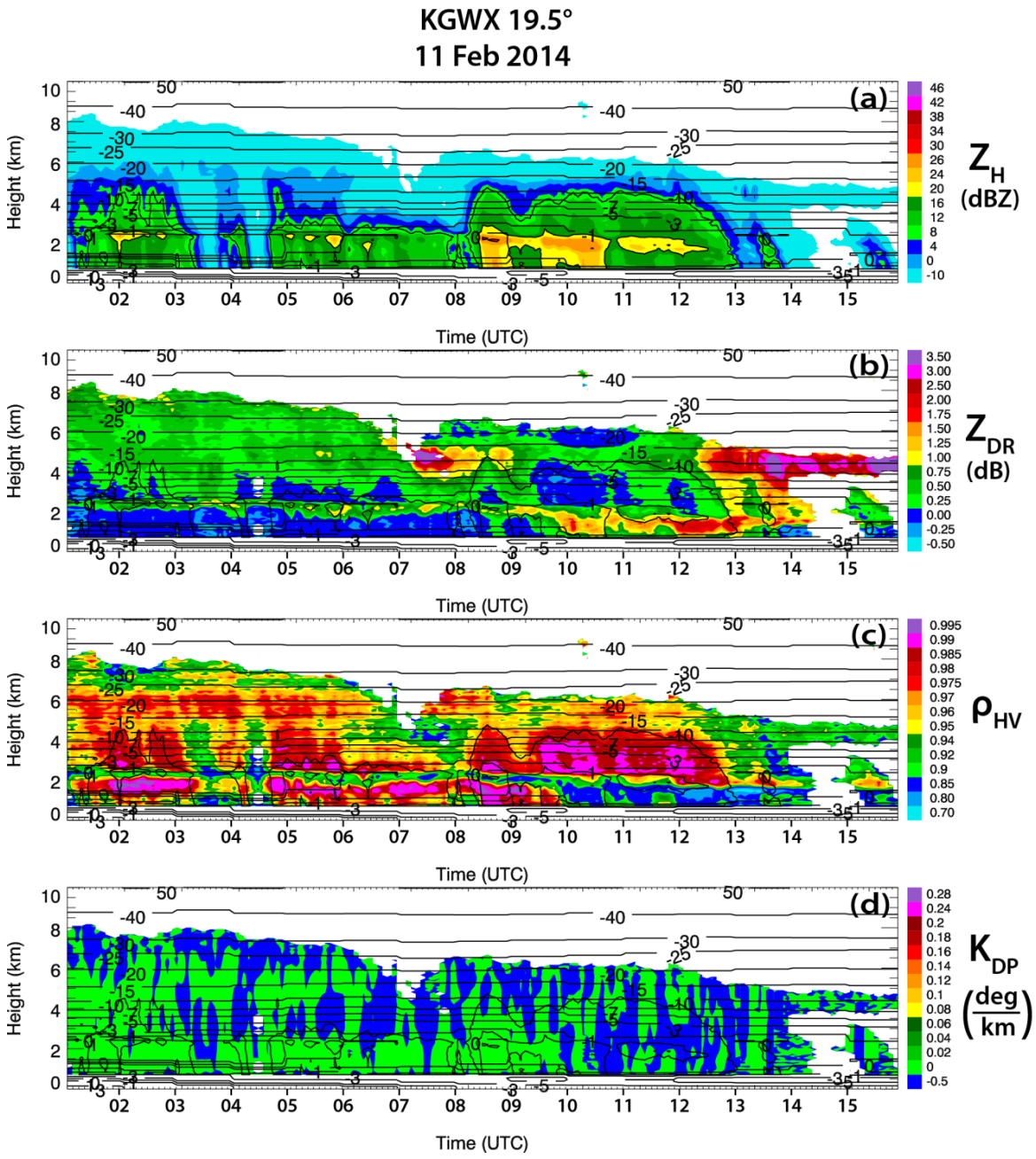

Fig. 3.6: As in Fig. 3.3, but for KGWX from 0102 through 1555 UTC 11 Feb 2014, at 19.5° elevation.

2) KBMX 12 FEBRUARY 2014

Figure 3.7 presents another example from the same winter system using 14.6°-elevation QVPs from the KBMX radar from 0119 through 2325 UTC 12 February 2014. Heavy snow and freezing rain were the predominant precipitation types observed at the surface, with significant snow and ice accumulation up to 15.24 and 0.64 cm, respectively (NWS 2014b). The QVPs provide another prominent example of the anticorrelation of maximum K_{DP} and maximum Z_{DR} in the DGL, as well as the correlation of those features with CTT. Maximum K_{DP} in the DGL (up to 0.23° km^{-1}) occurs from approximately 0430 through 0940 UTC in a layer from 3.5 to 7 km, within Z_H between 10 and 20 dBZ, and above the largest Z_H near the surface. The K_{DP} maximum also occurs during the period of lowest Z_{DR} in the DGL, when cloud top is tallest (10 km) and coldest (< -40°C). Note that this event requires additional criteria for defining cloud top because of minimal echoes above the main cloud top. To extract CTTs (with respect to microphysical analysis of the QVPs) for this event, the KBMX plots were processed in a similar manner to those of the KEAX event in section 3a, but with cloud top after 1231 UTC defined as the top of the echo beneath the midlevel layer of dry air, at approximately 5 km.

After 1200 UTC, cloud top decreases in height to approximately 5 km, near the -15°C model-indicated isotherm, while Z_H never exceeds 20 dBZ near the surface. During this period of shallower cloud top (i.e., from 1200 through 2325 UTC), K_{DP} in the DGL is very low, while Z_{DR} is enhanced and remains high within a layer between cloud top and the ML (i.e., between approximately 2 and 5 km), with maximum values up to 4.3 dB within the DGL. The layer of enhanced Z_{DR}, low K_{DP}, and low Z_H between cloud top and

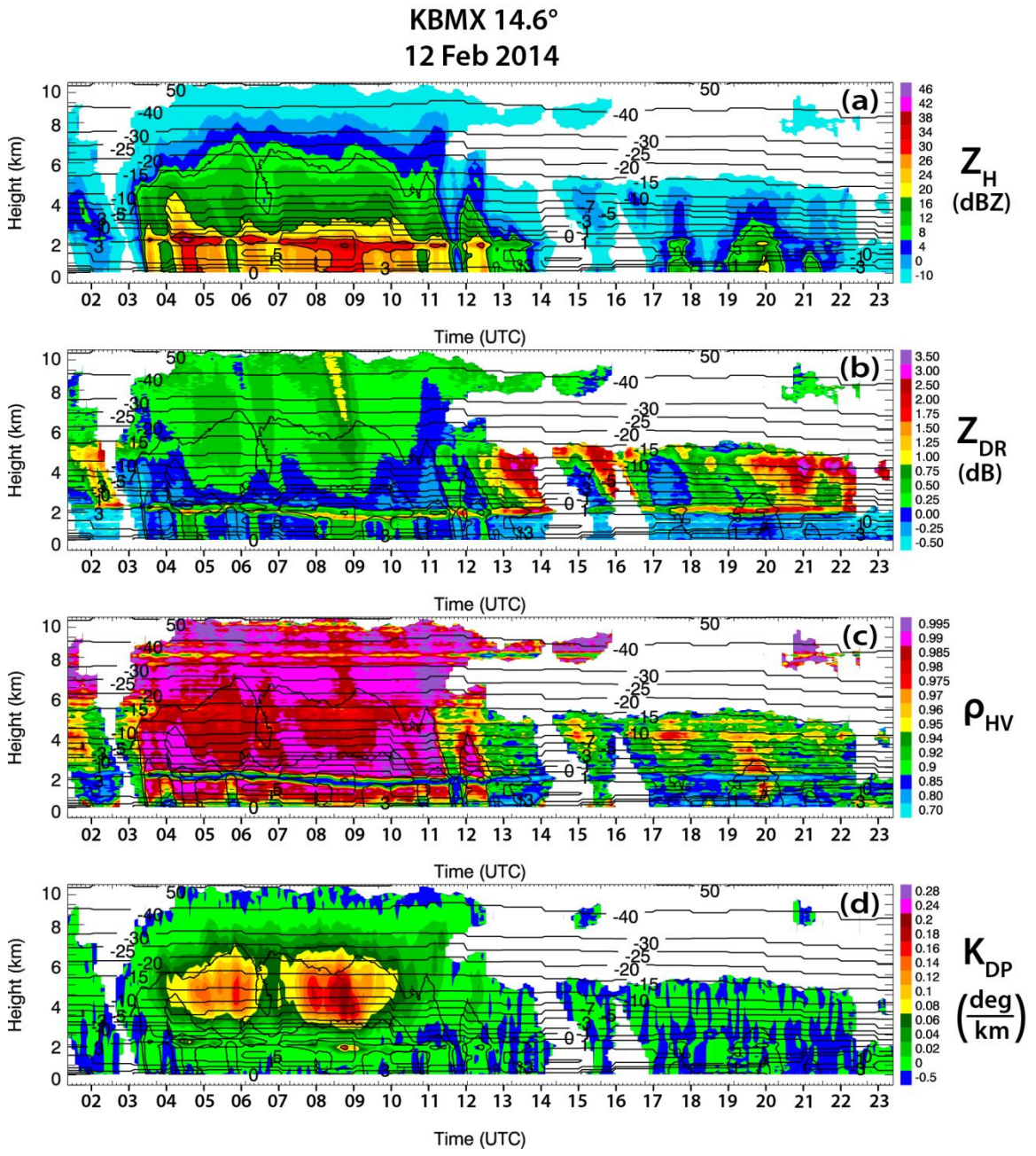

Fig. 3.7: As in Fig. 3.3, but for KBMX from 0119 through 2325 UTC 12 Feb 2014, at 14.6° elevation.

the ML indicates a low concentration of crystals that are generated in the DGL and fall into the ML without being aggregated, so that Z_{DR} remains high (Fig. 3.7b). Anisotropic, high-

density ice crystals acquire water coating while falling through the ML and produce very high Z_{DR} combined with almost nonexistent brightband enhancement of Z_H because of low concentration of ice particles and their small sizes.

3) KDGX 12 FEBRUARY 2014

A final example from the same southeastern U.S. winter storm event is from the KDGX radar, which produced a variety of precipitation types at the surface, including rain and freezing rain (ASOS). Figure 3.8 illustrates the 10° elevation KDGX QVPs from 0006 through 1500 UTC 12 February 2014. As with the other radars presented for this system, these plots provide an exceptional example of anticorrelated maximum K_{DP} and maximum Z_{DR} in the DGL, as well as the correlation of those features with CTT.

One of the most dramatic signatures is found in the K_{DP} profile (Fig. 3.8d). Maximum K_{DP} in the DGL reaches 0.3° km^{-1} from approximately 0200 through 0320 UTC in a layer from approximately 4 to 7 km, within Z_H between approximately 10 and 20 dBZ, and above the largest Z_H near the surface. The K_{DP} maximum also occurs during the period of lowest Z_{DR} in the DGL, when cloud tops are tallest and coldest (at approximately 10 km and < -40°C, respectively; Figs. 3.8b,d). During this period, enhanced Z_{DR} of approximately 1–1.75 dB and ρ_{hv} near unity in the upper region of the cloud indicates nucleation of pristine crystals within the coldest temperatures aloft, with maximum K_{DP} suggesting a resultant increase in ice concentration in the DGL.

After the period of tallest cloud-top height and largest Z_H near the surface, cloud-top height drops to approximately 5 km, near the -15°C isotherm, after approximately

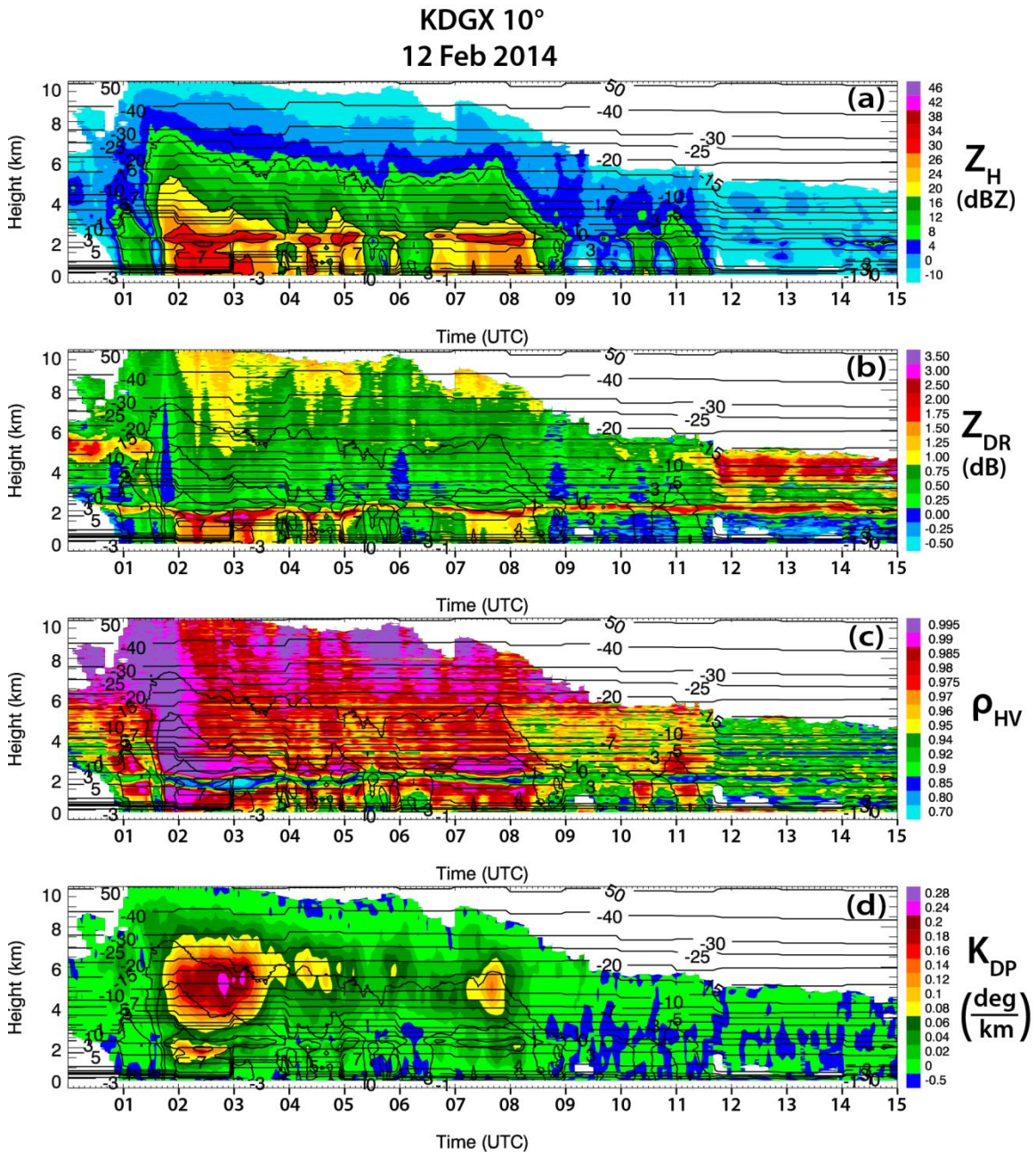

Fig. 3.8: As in Fig. 3.3, but for KDGX from 0006 through 1500 UTC 12 Feb 2014, at 10° elevation.

1150 UTC. From 1150 through 1500 UTC, cloud-top height is the shallowest during the event, while K_{DP} in the DGL is reduced to approximately 0° km^{-1} and Z_{DR} is noticeably enhanced between 3 and 5km, between the -7° and -15°C isotherms. Differential reflectivity Z_{DR} within this layer reaches a maximum of 4.3 dB, within ρ_{hv} from 0.9 to 0.95 and Z_H from -10 to 0 dBZ, suggesting the generation of pristine ice crystals in this region. The layer of enhanced Z_{DR}, low K_{DP}, and low Z_H between cloud top and the ML indicates the crystals grow quickly and fall toward the surface and into the ML, without being aggregated. The Z_{DR} is noticeably enhanced in the ML directly below this layer, indicating water-coating of the crystals as they begin to melt. Overall, this event further exhibits the consistency of the polarimetric features observed in the previous winter cases.

4. Statistical analysis

To quantify the above QVP results, 90th-percentile maximum Z_{DR} in the DGL (i.e., between -10° and -20°C), 90th-percentile maximum K_{DP} in the DGL, and 90th-percentile maximum Z_H in the DGL are computed (in this section referred to as maximum Z_{DR}, K_{DP}, and Z_H, respectively). Scatterplots are then generated to compare the relationships between these variables, as well as between the polarimetric variables and CTT. Using values within the 90th percentile ensures a good representation of the largest values in the layer, without being skewed by any extreme values.

Figure 3.9 depicts a composite of each of the scatterplots from the winter event QVPs described in section 3. Overall, the datasets for each event in each of the scatterplots align well, with particularly close agreement in the CTT versus maximum Z_{DR} in the DGL

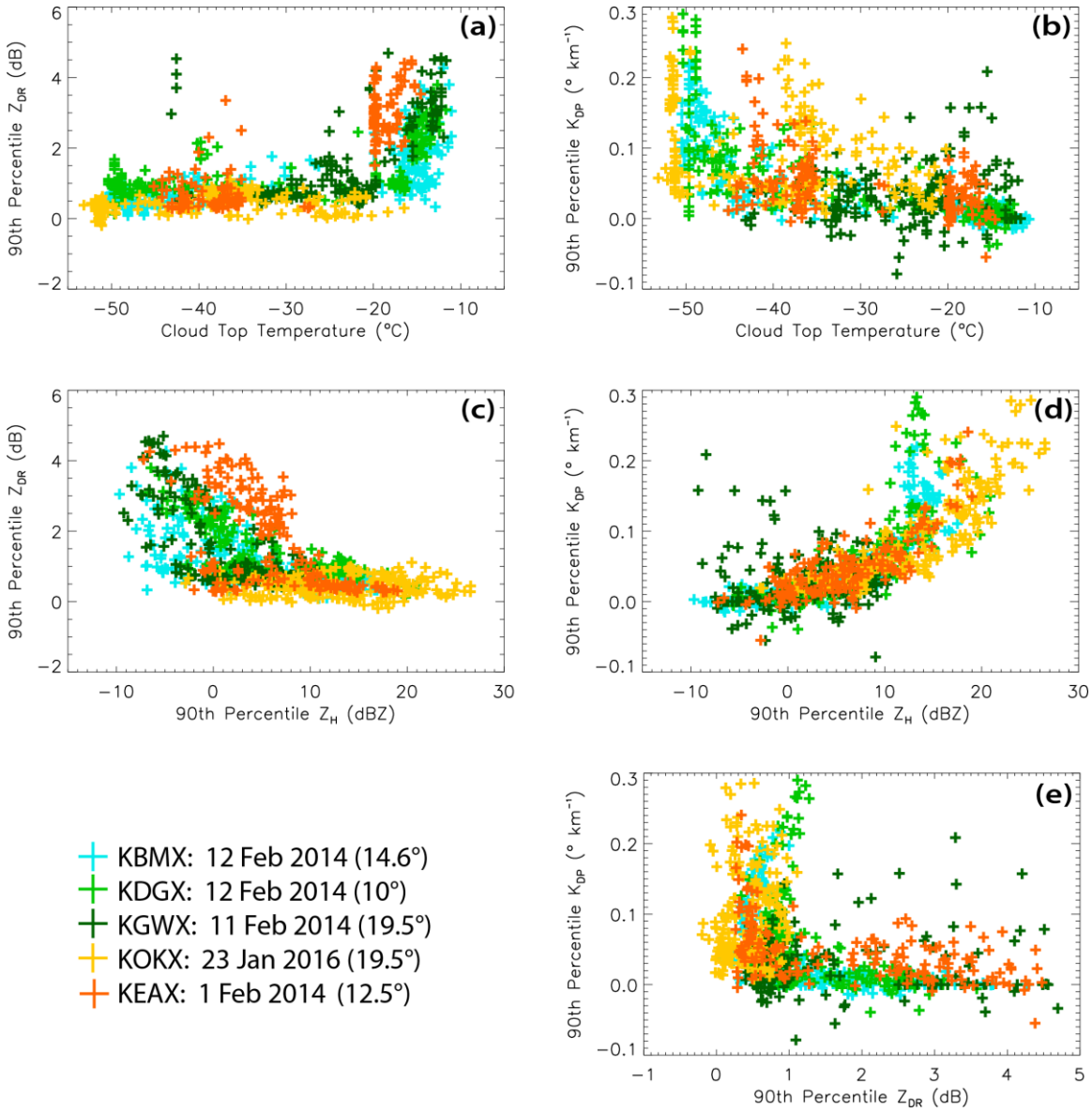

Fig. 3.9: Composite scatterplots of CTT (°C) vs 90th-percentile maximum (a) Z_{DR} and (b) K_{DP} in the DGL, 90th-percentile maximum Z_H in the DGL vs 90th-percentile maximum (c) Z_{DR} and (d) K_{DP} in the DGL, and (e) 90th-percentile maximum Z_{DR} in the DGL vs 90th-percentile maximum K_{DP} in the DGL. Data from the KBMX, KDGX, KGWX, KOKX, and KEAX events are indicated by the light-blue, light-green, dark-green, yellow, and orange symbols in each plot, respectively.

(Fig. 3.9a), maximum Z_{DR} in the DGL versus maximum K_{DP} in the DGL (Fig. 3.9e), and maximum Z_H in the DGL versus maximum K_{DP} in the DGL (Fig. 3.9d) plots. The plot of

CTT versus maximum Z_{DR} in the DGL (Fig. 3.9a) reveals two distinct clusters of values indicating moderate-to-high Z_{DR} (up to 6 dB) during warmer CTT between approximately -25° and -10°C, and low Z_{DR} (approximately 0–2 dB) during colder CTT of approximately < -25°C. Conversely, CTT versus maximum K_{DP} in the DGL (Fig. 3.9b) demonstrates two clusters of data indicating generally larger K_{DP} (approximately 0°–0.3° km^{-1}) during colder CTT from approximately -30° to -55°C, and lower K_{DP} (from approximately -0.1° to 0.1° km^{-1}) during warmer CTT from approximately -30° to -10°C.

Additionally, Fig. 3.9c demonstrates that larger maximum Z_{DR} in the DGL occurs within lower Z_H, with larger Z_{DR} of approximately 1–5.5 dB within Z_H between -10 and 10 dBZ, and Z_{DR} between approximately 0 and 1.5 dB within Z_H of approximately 0–30 dBZ. Figure 3.9d demonstrates a tight cluster of data points, distinctly indicating that for each of the QVP events, larger maximum K_{DP} occurs within greater Z_H in the DGL (strong positive correlation), with K_{DP} of approximately 0.05°–0.3° km^{-1} corresponding to Z_H between approximately 10 and 30 dBZ, and K_{DP} from -0.05° to 0.1° km^{-1} corresponding to Z_H between -10 and 10 dBZ. In other words, larger maximum Z_{DR} occurs within lower Z_H, while larger maximum K_{DP} occurs within greater Z_H in the DGL. Furthermore, Fig. 3.9e illustrates distinct anticorrelation of maximum Z_{DR} in the DGL versus maximum K_{DP} in the DGL, with larger K_{DP} from approximately -0.05° to 0.3° km^{-1} corresponding to Z_{DR} of approximately 0–1.5dB, and larger Z_{DR} of approximately 1–5 dB corresponding to K_{DP} between approximately -0.05° to 0.05° km^{-1}.

Overall, the data from the winter events reveal several trends. There is ample evidence of the repetitiveness of anticorrelation of Z_{DR} and K_{DP} in the DGL, with the

polarimetric variables strongly correlated with CTT. The Z_{DR} in the DGL is most pronounced and K_{DP} in the DGL is least pronounced during the shallowest and warmest cloud tops, while the opposite is true during the tallest and coldest cloud tops. These events also demonstrate that larger Z_{DR} in the DGL generally occurs within lower Z_H, while larger K_{DP} typically occurs within greater Z_H in the DGL.

5. Discussion

a. Interpretation of ice microphysical processes

The results of the observations can be tentatively explained using the concept of two primary habits of ice particles with distinct polarimetric radar characteristics. The first includes a broad category of snow aggregates and ice crystals with irregular or nearly spherical shapes. This category comprises an overwhelming majority of ice particles in stratiform clouds, according to the observations of Korolev et al. (2000, 2003). Another category includes pristine dendrites, hexagonal plates, and needles, which have very anisotropic shape and higher density than ice particles in the first category. Schrom and Kumjian (2016) distinguish these two classes of ice particles as "isometric" (I type) and "dendritic" (D type) and we will use similar names for these two categories, although they are not completely accurate. Indeed, "isometric" ice cannot be considered purely spherical or isometric because its aspect ratio is usually close to 0.6, as claimed by Korolev and Isaac (2003), Matrosov et al. (2005a), and Hogan et al. (2012). This means that I-type ice can produce moderate Z_{DR} and quite significant K_{DP} (if the concentration of I-type ice is sufficiently high). The "dendrite" class includes highly oblate (dendrites or hexagonal

plates) or prolate (needles) hydrometeors with aspect ratios as low as 0.01 or as high as 10. These ice crystals can have extremely large Z_{DR} (up to 10 dB) and tangible K_{DP} (if their concentration is sufficiently high). As opposed to the I-type crystals, which can be generated at any level in the full depth of a cloud, the D-type crystals are generated only in certain temperature ranges: from -20° to -10°C for dendrites and hexagonal plates and between -3° and -8°C for needles.

We suggest that the areas of high Z_{DR} are dominated by D-type ice, whereas the areas of high K_{DP} are overwhelmed with the I-type ice, which does not exclude the presence of D-type ice crystals as well. If the cloud top is high and cold, then a variety of ice habits can be generated as primary ice at the cloud tops, for example, in generating cells (Kumjian et al. 2014). Initial concentration of primary ice is determined by the concentrations of ice nuclei that strongly depend on temperature (DeMott et al. 2010; Bailey and Hallett 2009) or supercooled cloud droplets that undergo homogeneous ice nucleation for $T < -37$°C. In the latter case, the concentration of primary ice is particularly high. The I-type ice particles may grow slowly via deposition or aggregation (if their concentration and size are large enough) while they fall down to the top of the DGL at about -20°C. Within the DGL, their growth by deposition intensifies because of the increasing difference between the water vapor saturation pressures with respect to water and ice. This is a dominant process in the upper half of the DGL (Lo and Passarelli 1982). When a sufficient number of I-type particles reach larger size, then the aggregation process quickly takes over the deposition growth and becomes a dominant growth process in the

lower part of the DGL (below the -15°C level) and at lower altitudes down to the ML (Moisseev et al. 2015).

Once large isometric crystals/snowflakes fall through the DGL, they continue to grow as I-type ice without much change in their shape. However, small I-type crystals may serve as embryos of rapidly growing dendrites or plates (depending on the supersaturation with respect to ice) with very anisotropic shape (Chen and Lamb 1994; Sheridan et al. 2009). These D-type crystals grow much faster in the DGL than the isometric ones, because of their higher capacitance. In addition, they can grow to very large sizes because their residence time within the DGL is longer than that of the isometric crystals because of the difference in their terminal velocities (Schrom and Kumjian 2016). Chen and Lamb (1994) demonstrate that D-type crystals become more anisotropic during their growth and acquire extremely low aspect ratios, leading to very high values of Z_{DR} (up to 10 dB, e.g., as supported by observations of Z_{DR} up to 5.5 dB in Figs. 3.3 and 3.11).

Polarimetric radar variables depend on the relative contributions of the I-type and D-type ice particles in the mixture. In the situations when the DGL is not heavily seeded by I-type crystals falling from above, the contribution of the D-type ice is not masked by the contribution of I-type ice to Z_{DR} and the resulting Z_{DR} is very high. This explains strong dependence of Z_{DR} in the DGL on the temperature at the cloud top, which determines the concentration and size of I-type ice. The K_{DP} is usually quite low there because the total concentration of ice is low. There is also a notable decrease of ρ_{hv} in areas of the DGL where Z_{DR} is particularly high, since the ρ_{hv} of very anisotropic crystals is usually lower than that of quasi-spherical hydrometeors.

If the cloud is deep and the amount of isometric ice seeding the DGL is large, the contribution of I-type ice dominates the contribution from D-type crystals generated locally. This is why Z_{DR} may not show any enhancement in the DGL and the overwhelming majority of ice particles have aspect ratios close to 0.6, which is enough to produce very high values of K_{DP} (because of high overall concentration of ice) combined with very modest Z_{DR} that does not depend on the concentration. Moreover, the dominance of large-sized I-type ice may inhibit dendritic growth in the DGL completely because of strong competition of the D-type and I-type crystals for available water vapor.

Below the DGL, Z_H rapidly increases and Z_{DR} and K_{DP} tend to decrease toward the ground as a result of aggregation. The decrease of K_{DP} is likely caused by 1) the decrease of the snowflake density in the process of aggregation, 2) more chaotic orientation of large-sized snowflakes (e.g., Hendry et al. 1976, 1987; Matrosov et al. 2005b; Melnikov and Straka 2013), and 3) the decrease of the contribution of the pristine, nonaggregated D-type crystals. Z_{DR} usually remains high at the altitudes between -10° and 0°C, if Z_{DR} in the DGL is high and the cloud above the DGL is shallow (e.g., Figs. 3.3b, 3.6b, and 3.7b). This is attributed to very low concentration of ice, which inhibits aggregation.

Specific differential phase K_{DP} may exhibit a secondary maximum in the temperature interval between -3° and -8°C, where secondary ice production is possibly driven by the Hallett–Mossop process. This requires some presence of riming and results in a large number of splinters that rapidly grow as needles in this interval of temperatures. Although the present study did not observe this, the corresponding increase of K_{DP} and, sometimes, Z_{DR} is documented by Sinclair et al. (2016) and Giangrande et al. (2016).

b. In situ verification of polarimetric QVP observations of hexagonal plates in the DGL

Williams et al. (2013) recently documented airborne in situ microphysical measurements of a winter snowstorm that occurred on 28 February 2013 over the KBUF WSR-88D in Buffalo, New York. During their flight, they discovered rare evidence of hexagonal flat-plate crystals in horizontally expansive layers of low, mainly negative Z_H and high Z_{DR} of 4-8 dB, near the -11°C isotherm (Williams et al. 2013). Figure 3.10 displays a selection of their in situ observations, taken from 1835 through 1839 UTC. During this period, they document a region of predominantly hexagonal plates in a positive Z_{DR} region with values between 0 and 6 dB, with low Z_H from -15 to 7 dBZ, and indications of riming on the plates due to rounded corners on several of the crystals.

To look into the same cloud from the QVP perspective, and to determine whether the polarimetric QVP methodology reveals the presence of these crystals, data were obtained for this case and used to generate the associated QVPs. Unfortunately, because of the volume coverage pattern (VCP) used during this event, radar data are only available at as high as the 4.5° elevation angle. Nevertheless, even at 4.5° we see a prominent display of high Z_{DR} in the layer the aircraft was flying in during this period. Figure 3.11 shows the KBUF QVPs for Z_H and Z_{DR} at 4.5° elevation from 1600 through 2020 UTC 28 February 2013, for comparison with the Z_{DR} and in situ observations in Fig. 3.10. The Z_{DR} QVP indeed displays values in the range of 0-5.5 dB in the DGL, between the -10° and -15°C isotherms and during approximately 1800–1945 UTC. After inspection of the raw data, maximum values of up to 5.5 dB occurred near the -11°C isotherm, during approximately

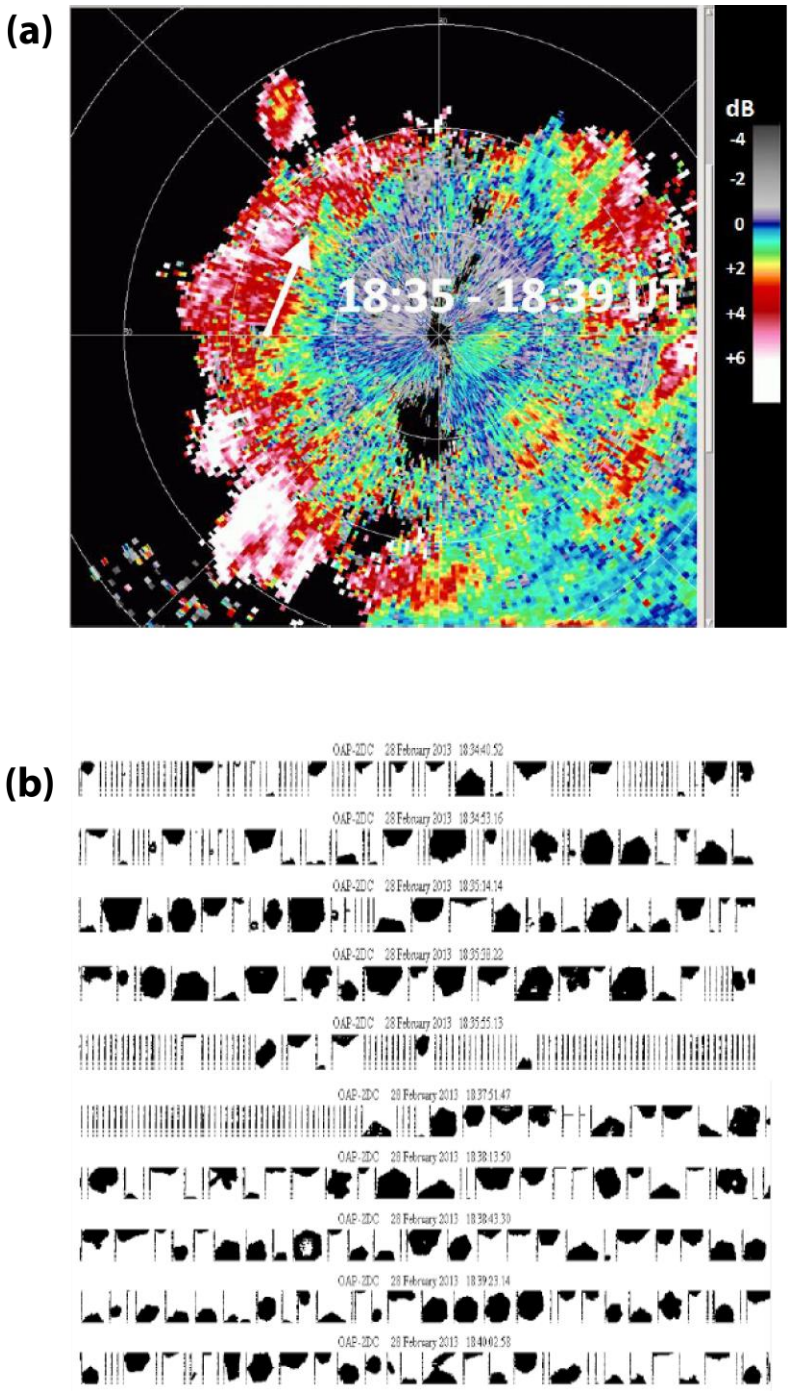

Fig. 3.10: (a) Differential reflectivity Z_{DR} at 2.5° elevation angle with range ring labels spaced every 10 n mi (18.52 km). The white arrow indicates a segment of the aircraft trajectory during this period. (b) Ice particle PMS 2DC imagery, with 25-μm pixel resolution and 800-μm spacing between vertical lines. During 1835–1839 UTC, hexagonal flat-plate crystals were found to be the predominant hydrometeor type, with corresponding Z_{DR} values of 0–6 dB. The figure is adapted from Williams et al. (2013).

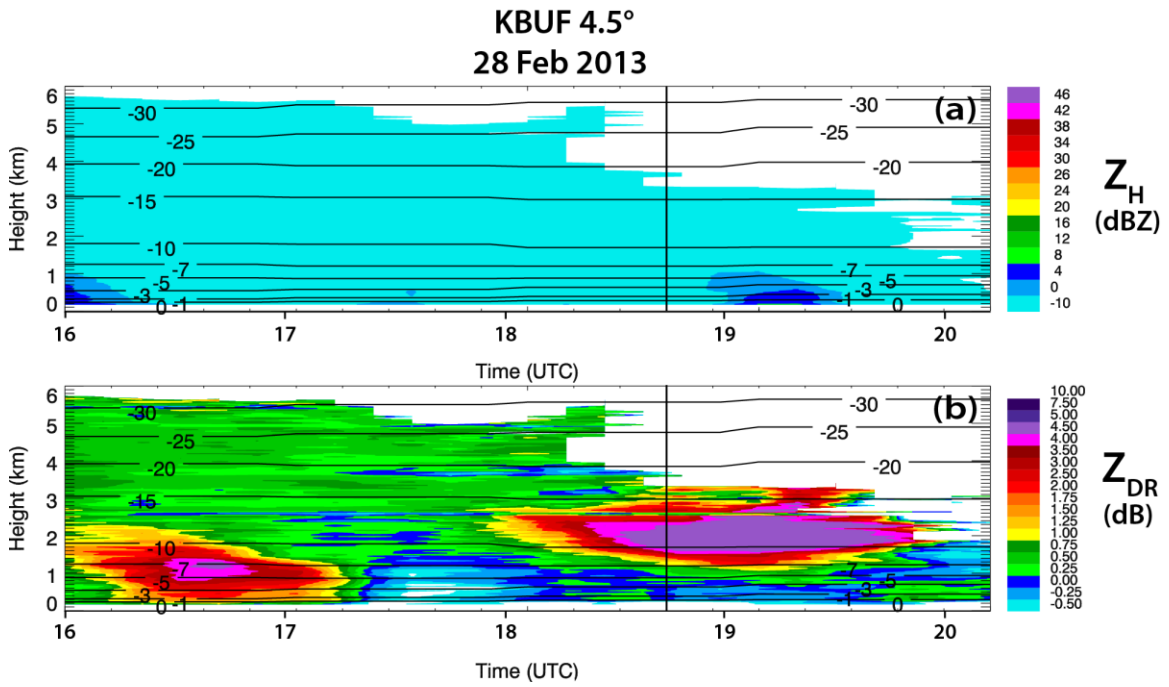

Fig. 3.11: QVPs of (a) Z_H and (b) Z_{DR} for KBUF from 1600 through 2020 UTC 28 Feb 2013, at 4.5° elevation. Contours of HRRR model wet-bulb temperature (°C) are overlaid in each plot. Also, Z_H is contoured at 10, 20, 30, and 40 dBZ. The vertical black lines indicate the flight time of the Williams et al. (2013) observations between approximately 1.5 and 2 km, from 1835 through 1839 UTC. Note that the Z_{DR} scale is expanded to illustrate the maximum Z_{DR} values in this event and is different than the Z_{DR} scale used in the other figures.

1837-1923 UTC (Fig. 3.11), which is consistent with Z_{DR} associated with hexagonal plates. Furthermore, the maximum Z_{DR} values occur near the edge of the -10-dBZ Z_H threshold. Overall, the KBUF QVP data support the findings of hexagonal plates in the DGL by Williams et al. (2013), and also support our interpretation of the QVP results of the five winter events in the previous sections.

6. Summary

Investigating the polarimetric and thermodynamic characteristics of winter precipitation is necessary to further our understanding of the microphysical processes within winter storms, as well as to improve their representation in numerical models. This study implements a new QVP methodology to investigate the microphysical evolution and significance of intriguing polarimetric signatures and their statistical correlations, observed in a selection of winter events. QVPs of transitional stratiform and pure snow precipitation are analyzed at high elevation angles (i.e., 9.9°–19.5°) using data from S-band WSR-88Ds, alongside their corresponding environmental thermodynamic HRRR model analyses. In particular, QVPs of K_{DP} are implemented to demonstrate their value in interpreting ice processes in the upper levels of storms. The radar data are examined in light of the thermodynamic environment within which they developed, to help deduce their relation to cloud-top temperature and to identify the types of crystals potentially present throughout the depth of the cloud.

Several fascinating and repetitive polarimetric signatures are observed in the Z_{DR} and K_{DP} QVPs, in the DGL and at the tops of clouds. The most striking feature is maximum Z_{DR} (up to 6 dB) in the DGL that occurs near the edge of the -10-dBZ Z_H contour within low K_{DP} and during shallower and warmer cloud tops, while maximum K_{DP} (up to 0.3° km^{-1}) in the DGL occurs within low Z_{DR} and during taller and colder cloud tops. Essentially, Z_{DR} and K_{DP} in the DGL are anticorrelated and depend on the temperature at the top of the cloud.

To quantify the QVP observations, 90th-percentile maximum Z_{DR} in the DGL, 90th-percentile maximum K_{DP} in the DGL, and 90th-percentile maximum Z_H in the DGL were computed to analyze the relationships between these variables, as well as between the polarimetric variables and CTT. The data demonstrate the distinct correlations of CTT with Z_{DR} and K_{DP} signatures in DGLs. The statistics also show that larger Z_{DR} occurs within lower Z_H in the DGL, while larger K_{DP} occurs within greater Z_H in the DGL. QVP data are also analyzed and compared to in situ microphysical measurements collected by Williams et al. (2013). These datasets verify the ability of the QVP to detect the presence of hexagonal plate crystals within the DGL, demonstrating the veracity of using QVPs to evaluate ice microphysics in the upper regions of winter clouds.

The QVP results can be attributed to distinct polarimetric radar characteristics of isometric (I type) and dendritic (D type) ice particles. I-type particles include a broad category of snow aggregates and ice crystals with irregular or nearly spherical shapes and can result in moderate Z_{DR} and significant K_{DP} (if the concentration of isometric ice is sufficiently high). The D-type crystals are composed of highly oblate (dendrites or hexagonal plates) or prolate (needles) hydrometeors that have very anisotropic shape and higher density than I-type ice particles. These ice crystals can exhibit extremely large Z_{DR} and tangible K_{DP} (if their concentration is sufficiently high; e.g., Fig. 3.5 illustrates enhanced Z_{DR} and K_{DP} between 1800 and 2100 UTC at approximately 5 km). As opposed to the I-type crystals, which can be generated at any level in the full depth of a cloud, the D-type crystals are generated only in certain temperature ranges, with dendrites and hexagonal plates between -20° and -10°C and needles between -3° and -8°C. We advocate

that the regions of high Z_{DR} are dominated by D-type ice, whereas the regions of high K_{DP} are overwhelmed with the I-type ice, which does not exclude the presence of D-type ice crystals as well. Overall, the results of this analysis provide a next step toward advancing understanding of microphysical processes within winter clouds and precipitation, and demonstrate the value of QVPs in detecting key features in the upper regions of clouds.

Chapter 4: A Polarimetric Radar Analysis of Ice Microphysical Processes in Melting Layers of Winter Storms using S-band Quasi-Vertical Profiles

Material in this chapter is from Griffin et al. (2019), submitted for publication.

Abstract

Quasi-vertical profiles (QVPs) obtained from a large-scale database of U.S. WSR-88D radar data are used to document the polarimetric characteristics of the melting layer (ML) in cold-season storms with high vertical resolution and accuracy. A polarimetric technique to define the top and bottom of the ML is first introduced. Using the QVPs, statistical relationships are then developed to gain insight into the evolution of microphysical processes above, within, and below the ML, leading to a statistical polarimetric model of the ML that reveals characteristics that reflectivity data alone are not able to provide, particularly in regions of weak Z_H. Results reveal strong positive correlation between Z_H in rain (i.e., 0.3 km below ML) and Z_H in snow (i.e., 0.3 km above ML) and between maximum Z_{DR} in the ML and Z_{DR} in rain. Strong positive correlation is also observed between maximum K_{DP} and maximum Z_H in the ML; these are the first reliable QVP observations of K_{DP} in MLs documented at S band. Strong negative correlation occurs between maximum Z_{DR} and minimum ρ_{hv} in the ML and between minimum ρ_{hv} in the ML and the corresponding enhancement of Z_H (i.e., $\Delta Z_H = Z_{Hmax} - Z_{Hrain}$). Quantifying the $\Delta Z(\min(\rho_{hv}))$ dependence is crucial for implementation of a polarimetric vertical profiles of rain (PVPR) technique designed to mitigate the impact of ML contamination on QPE. The evidence of very large Z_{DR} (up to 4 dB) and δ (up to 145°) associated with lower Z_H (-10 to 20 dBZ) in the ML is documented in situations

when pristine, non-aggregated ice falls through it. A strong microphysically-driven connection between polarimetric signatures in the ML and aloft in the dendritic growth layer (DGL, between -10 and -20°C) and the temperature at the top of the cloud has been found. For example, "sagging" of the ML typically occurs during periods of enhanced K_{DP} in the DGL and taller cloud tops. Also, a strong positive correlation between K_{DP} in the DGL and K_{DP} in the ML is observed.

1. Introduction

Winter precipitation events, particularly transitional storms and heavy snow, are difficult to accurately forecast and nowcast, largely due to poor parameterization of ice microphysical processes in numerical weather prediction (NWP) models. Since snow and ice particles are typically non-spherical and have aspect ratios, orientations, and bulk densities that vary significantly in clouds both temporally and spatially, polarimetry is a valuable tool that can be used to estimate bulk properties of snowstorms (Ryzhkov et al. 1998). In particular, operational polarimetric radar networks, such as the WSR-88D network, provide an opportunity to identify and quantify informative polarimetric signatures on a large scale, investigate their repeatability and relations to underlying physical processes of precipitation formation, and perform statistical analyses of their properties. Furthermore, since polarimetric observations provide valuable information on the size, shape, orientation, and phase of hydrometeors (e.g., Herzegh and Jameson 1992; Doviak and Zrnić 1993; Zrnić and Ryzhkov 1999; Straka et al. 2000; Kumjian 2013a,b,c), they improve our understanding of microphysical processes and the lifecycle of ice

particles as they nucleate, evolve, and fall through a cloud. They also lead to improvements in the representation of ice crystal properties including size, shape, density, and temperature dependence in future cloud microphysical models. This is important, since ice crystal habits are particularly sensitive to even slight changes in thermodynamic conditions and ice supersaturation (e.g., Bailey and Hallett 2009), which can influence precipitation rates at the surface.

The most pronounced and persistent polarimetric signatures in stratiform clouds are typically those associated with the melting layer (ML) and the dendritic growth layer (DGL; e.g., Griffin et al. 2018). Ice microphysical processes are particularly complex within and near MLs, resulting in poor representation of ML microphysics in numerical models. MLs are identified by a narrow, nearly horizontal layer beneath the 0°C isotherm that is typically characterized by high radar reflectivity (Z_H), reduced co-polar correlation coefficient (ρ_{hv}), and increased differential reflectivity (Z_{DR}) as particles melt (e.g., Wolfensberger et al. 2015). Developing a thorough understanding of the polarimetric properties of the ML is important for several reasons. First, the microphysical structure of the ML mirrors key microphysical processes of precipitation formation and evolution aloft and is also closely related to rain drop size distributions below the ML (e.g., Wolfensberger et al. 2015; Kumjian et al. 2016; Trömel et al. 2014; Trömel et al. 2017). Second, current NWP models do not adequately treat melting and sublimation of snow within the ML and, third, satellite retrievals require an appropriate microphysical model of the ML that does not exist. Ideally, all existing models and retrievals should be optimized using vertical profiles of polarimetric radar variables after converting their outputs to the

fields of radar variables. These needs all point to the importance of obtaining a catalogue of polarimetric signatures in the ML against which model outputs and satellite retrievals can be compared.

Another important application of improved ML observations is to mitigate "bright band" contamination in quantitative precipitation estimation (QPE) estimates at large distances from the radar, where the radar's beam intersects mixed-phase and frozen particles within the ML resulting in erroneous rainfall estimates (Giangrande et al. 2008). Techniques that use vertical profiles of reflectivity (VPR) to mitigate ML contamination on QPE have been developed and used with limited success (e.g., Fabry and Zawadski 1995). More recently, there have been efforts to augment the use of Z_H in VPRs by complementing it with Z_{DR} and ρ_{hv} in a scheme referred to as polarimetric vertical profiles of rain (PVPR; e.g., Trömel et al. 2017).

While relatively few studies have documented the polarimetric characteristics of MLs, several (e.g., Brandes and Ikeda 2004; Tabary et al. 2006; Giangrande et al. 2008; Matrosov et al. 2007; Kalogiros et al. 2013; and Wolfensberger et al. 2015) have proposed algorithms to automatically detect either the height of the freezing level or top and bottom of the ML in polarimetric PPIs or RHIs using different combinations and thresholds of ρ_{hv}, Z_{DR}, and Z_H. For example, Wolfensberger et al. (2015) developed an algorithm to detect the ML in stratiform precipitation using polarimetric X-band RHI scans. Their results indicated strong relationships between ML depth and the presence of rimed particles, the vertical velocity of particles, and ML intensity.

More recently, polarimetric quasi-vertical profiles (QVPs, used in this study and described in more detail in Section 2) have been used to study ice microphysical processes and document their temporal evolution. The QVP methodology was first implemented by Kumjian et al. (2013) to investigate polarimetric characteristics of refreezing signatures in winter storms and Trömel et al. (2014) to document the reliability of backscatter differential phase (δ) measurements in the ML. Ryzhkov et al. (2016) more formally developed the QVP methodology and documented its many benefits, including its abilities to continuously monitor the evolution of the ML and DGL with high vertical resolution, to easily compare data from polarimetric WSR-88D radars to data from vertically-looking remote sensors (e.g., wind profilers, lidars, and cloud radars), and to potentially discriminate between rimed and aggregated snow. Since then, QVPs have been used by numerous researchers to study the microphysical structure of stratiform clouds. Kumjian and Lombardo (2016), in a study of a Northeast winter storm, were the first to use WSR-88D QVPs of Doppler velocity and polarimetric variables to infer regions of mesoscale ascent and directly relate kinematic and microphysical information in winter storms. Tobin and Kumjian (2017) used a modified QVP technique, referred to as the range-defined QVP, to investigate the relationships between refreezing layer signatures and warm air advection, transitions in surface precipitation type, and how the refreezing signature might be used operationally to forecast those transitions. Griffin et al. (2018) used QVPs to demonstrate the value of Z_{DR} and specific differential phase (K_{DP}) to interpret elevated ice processes in winter storms, finding that Z_{DR} and K_{DP} in the DGL strongly depend on cloud-top temperature and were anti-correlated. They also found that the high Z_{DR} regions

in the DGL were likely dominated by the growth of a mixture of highly oblate dendrites and/or hexagonal plates, or prolate needles, while the regions of high K_{DP} in the DGL were likely dominated by snow aggregates and crystals with irregular or nearly spherical shapes, seeded at cloud tops.

Perhaps most relevant to this study is the study of Trömel et al. (2017), who used QVPs to develop polarimetric rainfall estimation algorithms. To gain insight into microphysics within and above the ML, Trömel et al. (2017) followed the ML detection methodology of Hickman et al. (2017) to conduct a study that examined X-band polarimetric radar data from 52 stratiform events in Bonn, Germany (BoXPol). QVPs were used to estimate polarimetric profiles of the ML and DGL and develop a PVPR technique to detect the ML and reliably estimate Z_H, Z_{DR}, ρ_{hv}, and K_{DP} in the ML and DGL at X band. They were also the first to document reliable K_{DP} statistics in the ML at X-band, as well as high correlations between K_{DP} in the ML and rain rate at the surface, K_{DP} and maximum Z_H in the ML, and maximum Z_{DR} and δ in the ML. K_{DP} is a particularly valuable polarimetric parameter since it contains important information about ice microphysics and is especially useful for the quantification of ice (e.g., Ryzhkov et al. 1998; Griffin et al. 2018; Ryzhkov et al. 2018). It also more accurately characterizes precipitation flux in the ML than either Z_H or Z_{DR}, which are both heavily weighted by large wet snow aggregates (e.g., Trömel et al. 2017). Since there is often a strong contribution of δ to the total differential phase Φ_{DP} in the ML at S band, Griffin et al. (2018) introduced a methodology to remove δ contamination in the estimation of K_{DP}.

Currently, more reliable statistics are needed to understand the behavior of K_{DP} in the ML and its relation to elevated ice processes and precipitation rates at the surface.

While eliminating δ is necessary to accurately estimate K_{DP} in the ML, it is in itself an important polarimetric parameter that can be used to improve understanding of ice processes above and within the ML. Trömel et al. (2014) documented measurements of δ within the ML, as well as how it depends on radar frequency. They found that δ in the ML is a reliable measurement, with observed maximal δ of 8.5° at X band and up to 70° at S band, which they attributed to large, partially melted snowflakes in the ML. Hydrometeors in the ML are large and wet and are not Rayleigh scatterers. Therefore, all radar variables in the ML are wavelength dependent. Also, maximum Z_H in the ML vanishes at mm wavelengths. Since values of δ in the ML in the U.S. at S band are much higher than those measured in Europe at both C and X band (e.g., Trömel et al. 2014), it would be useful to determine if that difference is entirely attributed to the difference in radar wavelengths or if it can also be accounted for by differences in the intensity and morphology of storms from different climate regions. Backscatter differential phase δ also provides valuable information on accretion and aggregation microphysical processes within the ML, as well as the degree of riming of crystals above the ML (e.g., Trömel et al. 2014). Larger δ and high Z_{DR} in the ML can indicate larger aggregates above the ML (e.g., Trömel et al. 2014; Ryzhkov et al. 2016; Fridlind et al. 2017) and may be valuable for determining the degree of riming above the ML since unrimed snow was observed to result in significantly larger δ than rimed snow (Trömel et al. 2014). There is also a possible correlation between the presence of DGLs and δ in the ML (Trömel et al. 2014). Furthermore, since microphysical

models of the ML must consider accretion and aggregation to reveal large δ in the ML (Trömel et al. 2014), δ measurements can help improve representation of ML microphysics in future models.

Since January of 2013, we have compiled a database that consists of thousands of hours of polarimetric WSR-88D S-band radar observations in a wide variety of winter precipitation events. Many of those datasets exhibit several intriguing and repetitive polarimetric signatures. In this study, we use QVPs produced from 33 WSR-88D radar data sets collected during 17 winter weather events to investigate the microphysical evolution and significance of some of those signatures and to improve understanding of the structure and behavior of the ML in cold-season precipitation. Radar data and their microphysical interpretation are presented in context of the thermodynamic environment provided by a numerical model to develop a polarimetric model of the ML and document statistical relationships in the ML to gain insight into the evolution of the microphysical processes above, within, and below the ML.

2. Methodology

The overarching goals of this study are 1) to create a large-scale database that documents the polarimetric characteristics of the ML in winter storms, and 2) to use statistical relationships developed from that database to gain insight into the evolution of microphysical processes above, within, and below the ML. In total, the data base included several hundred WSR-88D data sets collected during winter weather events. From that data base, 33 WSR-88D data sets from 17 events were chosen for analysis in this study.

Those data sets are listed in Table 4.1. To eliminate contributions from warm-season events, in which the microphysical structure of the ML might be influenced by nearby convection, particular care was taken to choose cold-season events that exhibited widespread regions of stratiform precipitation. As can be seen from Table 4.1, all events chosen for this analysis were collected during cold-season months (late November through early March). Most also exhibited winter weather precipitation types (snow, wet snow, ice pellets, and freezing rain) within the radar domain.

The events listed in Table 4.1 constitute approximately 400 h of data. In that sense, this study is probably most similar to that of Fabry and Zawadzki (1995, hereafter referred to as FZ95), who used vertical profiles of reflectivity obtained from 600 h of vertically-pointing X-band radar data (and 50 h of UHF boundary layer wind profiler data) to produce quantitative analysis of microphysical processes through the ML. While their results are valuable, they lack a polarimetric perspective that can reveal characteristics of the ML that reflectivity data alone are not able to provide. We now present the methodology for identifying the ML in the radar data and extracting the polarimetric variables above, within, and below the ML of those events.

Table 4.1: QVP winter ML events, including their dates, radars, radar elevation angles, and periods for 17 ML winter precipitation events that were observed from the perspective of the 33 QVPs used in this study.

QVP Winter ML Events (17 Events, 33 QVPs)			
Date	**Radar**	**Elevation (°)**	**Time (UTC)**
28 Jan 2014	KJGX	19.5	1314-2400
	KMOB	19.5	1218-2400
	KCLX	19.5	1910-2356
	KLCH	19.5	1109-2300
29 Jan 2014	KLTX	19.5	0004-1000
1 Feb 2014	KEAX	12.5	0353-1700
3 Feb 2014	KDIX	19.5	0641-1900
4 Feb 2014	KPAH	9.9	1553-2400
11 Feb 2014	KLTX	19.5	0900-2400
	KGWX	19.5	0006-2400
	KMHX	19.5	0352-2400
	KFFC	9.9	0008-1600
12 Feb 2014	KGSP	12.5	1438-2400
	KRAX	14.6	0809-2400
	KFFC	9.9	0212-2400
	KJGX	19.5	0244-2400
	KLTX	19.5	0614-2030
	KCLX	14.6	0009-2351
	KDGX	10.0	0006-1955
	KBMX	14.6	0119-2243
13 Feb 2014	KGSP	12.5	0004-1500
2 March 2014	KTLX	19.5	1801-2207
21 Feb 2015	KLVX	19.5	0321-2219
25 Feb 2015	KFFC	19.5	1400-2400
	KBMX	9.9	1224-2355
3 March 2015	KCLE	14.6	1156-2400
4 March 2015	KLVX	19.5	0326-2400
	KPAH	19.5	0026-2400
	KVWX	19.5	0007-2400
5 March 2015	KLWX	9.9	0009-2100
27 Nov 2015	KLTX	19.5	1006-2000
27 Dec 2015	KVNX	10.0	0004-1834
22 Jan 2016	KRAX	9.9	0546-2400

a. Quasi-vertical profiles (QVPs)

As noted earlier, we utilize the QVP methodology to study the polarimetric signatures above, within, and below the ML of winter precipitation systems. As documented by Ryzhkov et al. (2016) and Griffin et al. (2018), QVPs are constructed by azimuthally averaging Z_H, Z_{DR}, ρ_{hv}, and Φ_{DP} fields at relatively high antenna elevation angles exceeding 10° to 20°. Use of these high elevation angles reduces the effects of beam broadening and horizontal inhomogeneity, which allows for quantifying polarimetric characteristics of clouds and precipitation with high vertical resolution and dramatically improved statistical accuracy (Ryzhkov et al. 2016). The resulting QVPs display the polarimetric variables in a convenient time-versus-height format, which allows for efficient investigation of key cloud microphysical processes and their temporal evolution. The QVP's higher vertical resolution and reduced noisiness in the polarimetric signatures allows for observation of smaller-scale features that would not be observable using range height indicators reconstructed from plan-position indicator scans with lower resolution. QVPs, including methodologies to extract δ and accurately compute K_{DP} in the ML, are discussed in more detail by both Ryzhkov et al. (2016) and Griffin et al. (2018).

b. Defining the top and bottom of the ML

A crucial step in examining the polarimetric and microphysical characteristics of the ML is to accurately define both the top and bottom of the ML. In their study, FZ95 capitalized on the fact that vertical profiles of Z_H through the ML (see their Fig. 1) are typically characterized by a sharp increase/decrease in reflectivity at the top/bottom

(associated, respectively, with the heights where melting begins/ends) of the ML. By determining the heights of maximum curvature associated with these points, FZ95 were able to determine physically relevant heights associated with both the top and bottom of the ML. For the curvature method to be successful, however, FZ95 noted that it was necessary for the vertical profile of reflectivity to exhibit strong curvature at both the top and bottom of the ML, and not elsewhere. In this study, we seek to develop a polarimetric methodology for determining the top and bottom of the ML that not only closely replicates the results of FZ95, but also provides heights for the ML top and bottom in regions of weak reflectivity where polarimetric signatures of a ML are strong but the FZ95 curvature method was found to frequently fail.

Since the onset of melting also results in an increase in hydrometeor diversity, the most logical polarimetric method to determine the height of the ML top and bottom is to utilize ρ_{hv}. For each event analyzed, the height of minimum ρ_{hv} was first determined for a narrow height interval that encompassed the ML over the entire period of that event. Once the height of the minimum ρ_{hv} was found, an upward/downward search was conducted from that point to find the ML top/bottom heights associated with the first occurrence of ρ_{hv} that exceeded a predefined threshold. After testing this methodology on several events, a threshold of $\rho_{hv} \geq 0.97$ was found to exhibit the best agreement with the curvature results of FZ95. When compared to the curvature method on several events, the ρ_{hv} method was found to produce ML top heights that were on average only as much as 200 m lower and ML bottom heights that were 0 to 100 m higher or lower than the curvature method. An

additional search criterion that required Z_H to exceed 10 dBZ at the top/bottom heights was added to eliminate poor detections where ρ_{hv} was depressed in regions of weak echo.

For weak reflectivity regions or times at which corresponding ρ_{hv} data points were missing, an alternative method that relied upon the identification of the level of maximum backscatter differential phase, δ, was used. In this study, system differential phase is removed prior to computing the QVPs. Since the radar beam only passes through a few km of precipitation prior to encountering the ML, the Φ_{DP} presented in the QVPs typically provides an accurate representation of δ in the ML. Using the Φ_{DP} field and a methodology similar to that used for ρ_{hv}, the level of maximum δ was found and then upward/downward searches were conducted from that location to find the ML top/bottom heights associated with the first threshold of δ that corresponded well with the first occurrence of $\rho_{hv} > 0.97$ in regions of higher reflectivity. The δ thresholds varied for each of the 33 events, ranging between 0 and 40°, with a mean of about 9°. When necessary, ML top/bottom height results of the δ method were then combined with results from the ρ_{hv} method, particularly in regions of weak reflectivity or missing ρ_{hv} data, to produce a contiguous record of ML top/bottom height designations. This improves upon the Wolfensberger et al. (2015) method that implements Z_H and ρ_{hv} data to detect the top and bottom of the ML.

c. Polarimetric signatures above, within, and below the ML

An example of the application of our methodology to a winter storm is illustrated by Fig. 4.1, which shows a time series of QVPs from the KFFC (Atlanta, GA) WSR-88D on 11 February 2014. As can be seen in Fig. 4.1, a well-defined ML is difficult to discern

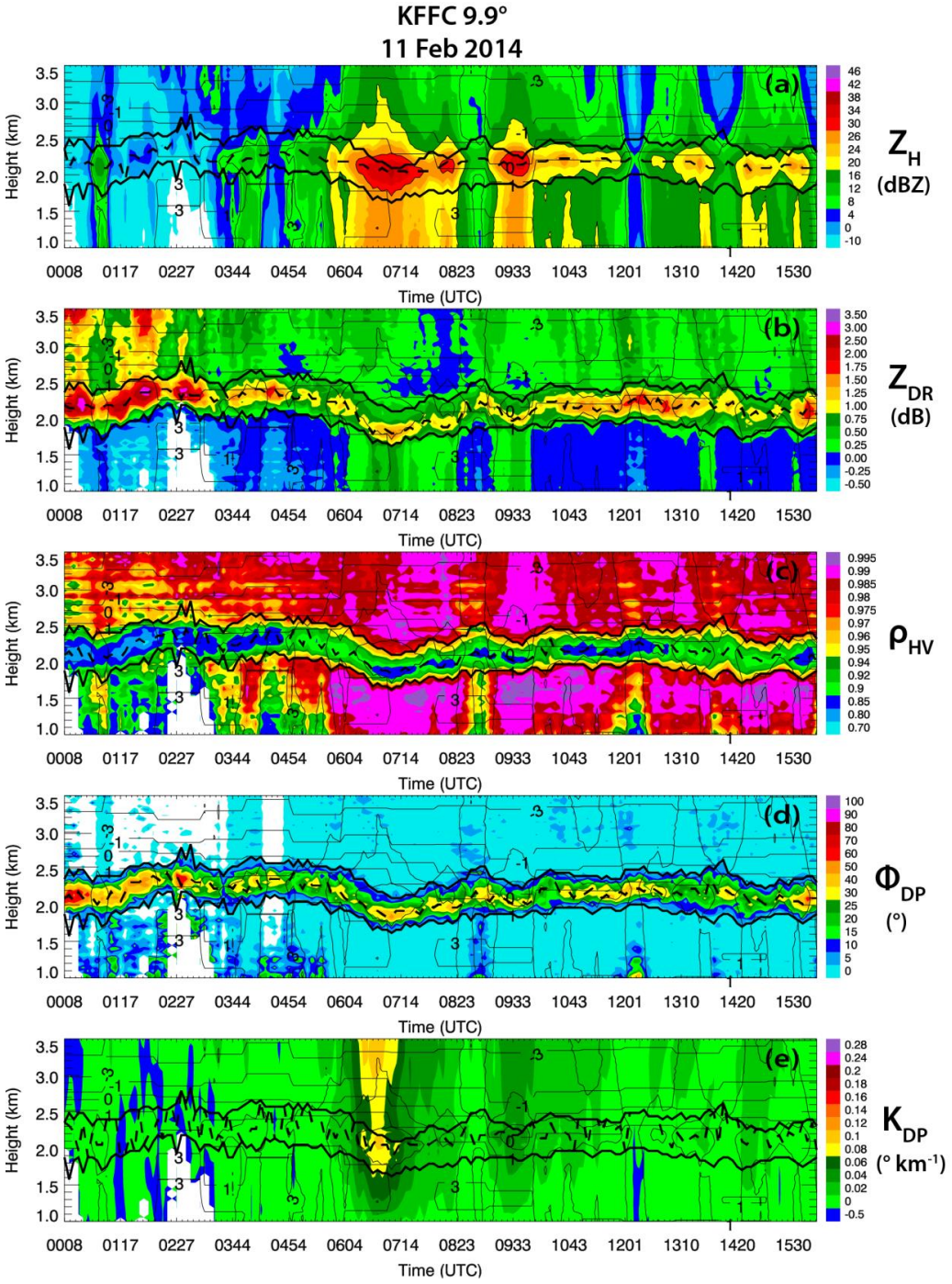

Fig. 4.1: QVPs of a) Z_H (dBZ), b) Z_{DR} (dB), c) ρ_{hv}, d) Φ_{DP} (°), and e) K_{DP} (° km^{-1}) for KFFC from 0008 through 1559 UTC on 11 Feb 2014, at 9.9° elevation. Contours of HRRR model wet-bulb temperature (°C) are overlaid in each plot. Also, Z_H is contoured at 10, 20, 30, and 40 dBZ. The ML top and bottom are represented by the bold black lines, while the bold dashed line between them represents the height of maximum Z_H, Z_{DR}, Φ_{DP}, K_{DP}, or minimum ρ_{hv}.

from approximately 0000-0300 UTC using Z_H alone (Fig. 4.1a), during which the curvature method of FZ95 failed to produce accurate results. On the other hand, a distinct ML signature is clearly evident in the Z_{DR}, ρ_{hv}, and Φ_{DP} fields (Figs. 4.1b, c, and d) over this same period. Results from the polarimetric method of ML top/bottom height detection are depicted in Fig. 4.1 by the solid black lines overlaid on each polarimetric variable, showing good overall visual consistency with the ML as depicted by the Z_{DR}, ρ_{hv}, and Φ_{DP} fields. Note that we follow the methodology of Griffin et al. (2018) to remove δ contamination in the estimation of K_{DP} in the ML. Also, all Z_{DR} measurements are corrected for bias according to the preprocessing procedures detailed by Ryzhkov et al. (2005) and by observationally ensuring Z_{DR} in snow is approximately 0.1 to 0.2 dB within heavily aggregated snow and Z_{DR} in pure rain near the surface is 0 to 5 dB, to ensure consistency across all cases in this investigation.

Once the ML top/bottom heights were determined, each period was examined to derive polarimetric characteristics above, within, and below the ML. These polarimetric characteristics are listed and defined in Table 4.2 and are used throughout the remainder of the text to examine polarimetric and microphysical features in the vicinity of the ML. The table also includes polarimetric variables derived from the DGL, as discussed by Griffin et al. (2018). Overall, the heights of the ML top and ML bottom for the FZ95 curvature and polarimetric methods compare well everywhere except within regions of low Z_H, with the FZ95 curvature method exhibiting slightly higher (i.e., approximately 200 m) ML tops and slightly higher or lower (i.e., approximately 50 m) ML bottoms. Since QVPs provide an unprecedented look into the microphysical processes within winter storms and are an

Table 4.2: Polarimetric variables derived from above, within, and below the ML. Variables derived from the DGL are also included (Griffin et al. 2018).

Variable	Definition
MLtopHeight	Height of ML top
MLbotHeight	Height of ML bottom
MLdepth	Depth of ML
ΔZ_H	Enhancement of Z_H (i.e., Maximum Z_H in ML - Z_H in rain)
MLmaxZ_H	Maximum Z_H in ML
MLmaxZ_{DR}	Maximum Z_{DR} in ML
MLminρ_{hv}	Minimum ρ_{hv} in ML
MLmaxδ	Maximum Φ_{DP} (i.e., δ) in ML
MLmaxK_{DP}	Maximum K_{DP} in ML
MLmaxZ_HHeight	Height of the maximum Z_H in the ML
MLmaxZ_{DR}Height	Height of the maximum Z_{DR} in the ML
MLminρ_{hv}Height	Height of the minimum ρ_{hv} in the ML
MLmaxδHeight	Height of the maximum δ in the ML
MLmaxK_{DP}Height	Height of the maximum K_{DP} in the ML
Z_HSnow	Z_H at 0.3 km above MLtopHeight
Z_{DR}Snow	Z_{DR} at 0.3 km above MLtopHeight
ρ_{hv}Snow	ρ_{hv} at 0.3 km above MLtopHeight
δSnow	δ at 0.3 km above MLtopHeight
K_{DP}Snow	K_{DP} at 0.3 km above MLtopHeight
Z_HRain	Z_H at 0.3 km below MLbotHeight
Z_{DR}Rain	Z_{DR} at 0.3 km below MLbotHeight
ρ_{hv}Rain	ρ_{hv} at 0.3 km below MLbotHeight
δRain	δ at 0.3 km below MLbotHeight
K_{DP}Rain	K_{DP} at 0.3 km below MLbotHeight
DGLmaxZ_H	90^{th} Percentile Maximum Z_H in DGL
DGLmaxZ_{DR}	90^{th} Percentile Maximum Z_{DR} in DGL
DGLminρ_{hv}	90^{th} Percentile Minimum ρ_{hv} in DGL
DGLmaxK_{DP}	90^{th} Percentile Maximum K_{DP} in DGL

efficient way to process and analyze polarimetric WSR-88D data, this investigation implements and builds upon the QVP methodology detailed in Ryzhkov et al. (2016) and Griffin et al. (2018) by demonstrating the value of using polarimetric QVPs to detect the ML.

3. Data analysis

In this section, we present data from S-band polarimetric WSR-88D QVPs at high elevation angles (i.e., 9.9°-19.5°) for the data sets presented in Table 4.1. The ML events occurred within stratiform precipitation over radars located in the southern, Midwestern, and northeastern United States. This analysis focuses on exploring ice microphysical processes above, within, and below the ML, as well as examining microphysically-driven connections between polarimetric signatures in the ML, the DGL (i.e., between -10 and -20°C), and below the ML. Since the events presented in Table 4.1 constitute more than 400 hours of observations and thousands of data points, composite histograms and composite density scatterplots are used to more effectively demonstrate the statistical relationships between the polarimetric variables. Weighted polynomial regressions are also implemented to obtain the most accurate fits while reducing the influence of any significant outliers.

a. Polarimetric statistics in the ML

1) HISTOGRAMS

Considering that polarimetric radar variables in the ML are poorly represented in numerical weather prediction models, statistical analyses of polarimetric signatures in the ML can help improve parameterization and understanding of microphysical processes above, within, and below the ML. Figures 4.2a-f present composite (computed using ML data obtained from QVPs of all of the events listed in Table 4.1) histograms of maximum

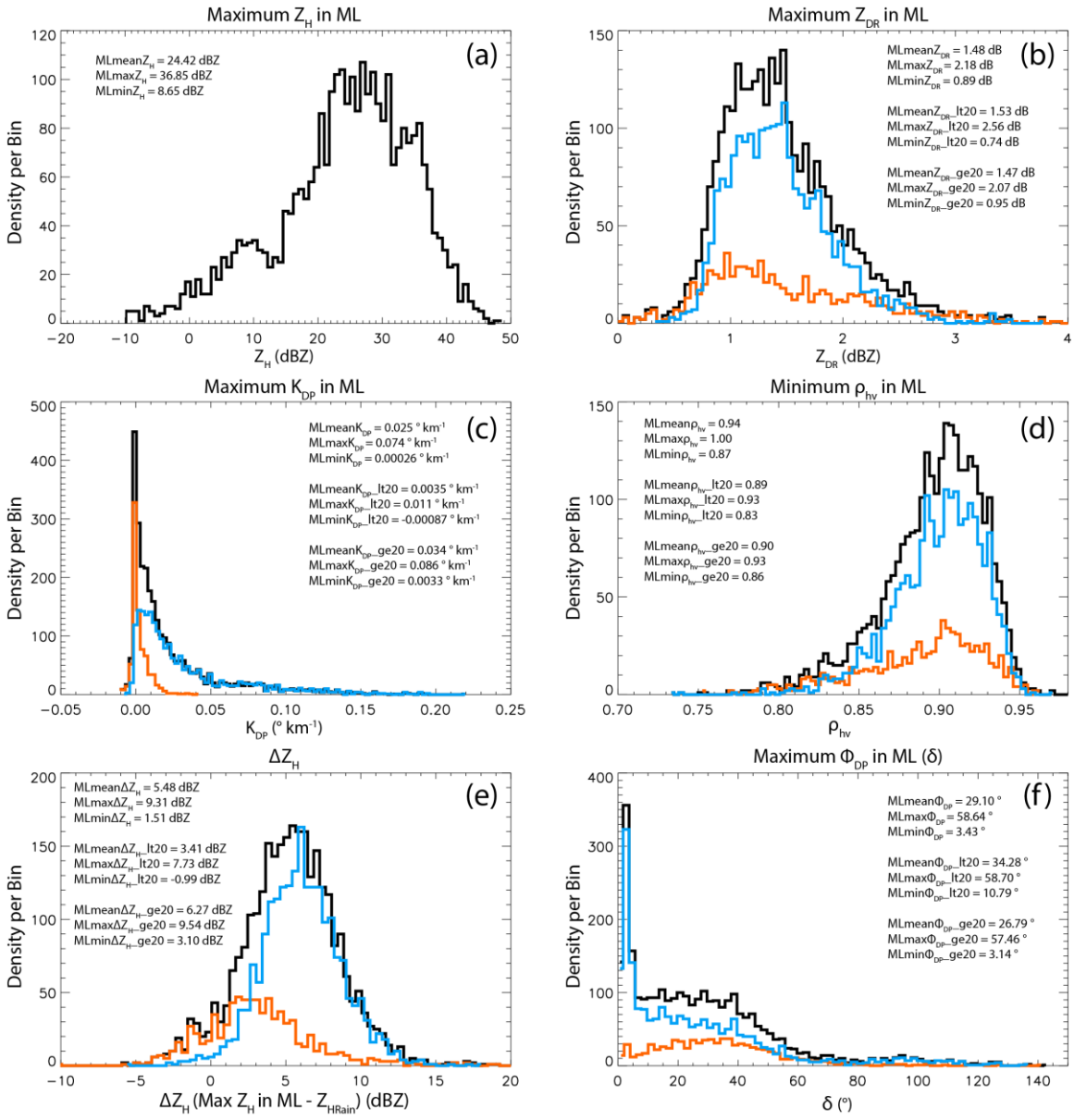

Fig. 4.2: Composite histograms of a) maximum Z_H in the ML (dBZ), b) maximum Z_{DR} in the ML (dB), c) maximum K_{DP} in the ML (° km^{-1}), d) minimum ρ_{hv} in the ML, e) ΔZ_H (i.e., Z_H in ML - Z_H in rain; dBZ), and f) maximum Φ_{DP} (i.e., δ; °) in the ML, for the 33 QVP ML events. Mean, 90th percentile maximum (indicated as max), and 10th percentile minimum (indicated as min) values of the variables are indicated in each panel, for the total dataset (represented by the bold black lines), the data corresponding to Z_H < 20 dBZ (represented by the orange lines), and the data corresponding to $Z_H \geq$ 20 dBZ (represented by the blue lines).

Z_H in the ML, maximum Z_{DR} in the ML, maximum K_{DP} in the ML, minimum ρ_{hv} in the ML, enhancement of Z_H (i.e., ΔZ = maximum Z_H in ML - Z_H in rain), and maximum Φ_{DP} (i.e., δ) in the ML, respectively. Additionally, Fig. 4.3 presents a composite histogram of ML depth (ΔH). Each of the histograms also include overlays of corresponding distributions

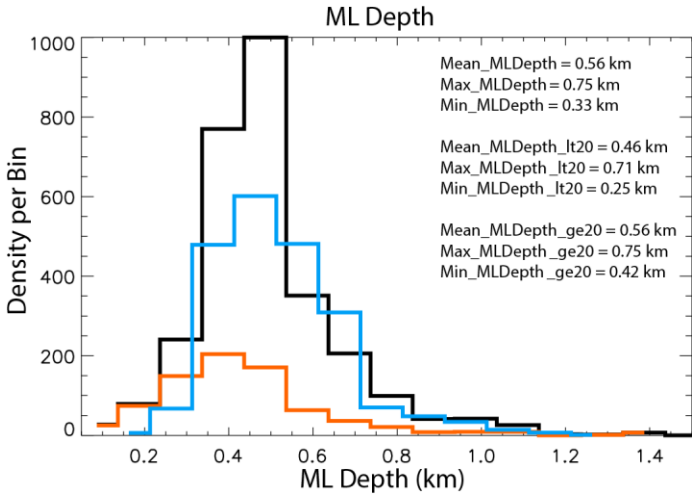

Fig. 4.3: Same as in Fig. 4.2, but for ML depth (km).

of data for which Z_H < 20 dBZ (indicated by the orange lines) and $Z_H \geq$ 20 dBZ (indicated by the blue lines). As will be discussed, these distributions exhibit both similarities and differences compared to X-band polarimetric ML distributions documented by Wolfensberger et al. (2015) and Trömel et al. (2017). It is important to note that the QVP-based histograms of polarimetric variables in the ML in Fig. 8 of Trömel et al. (2017) improve upon the RHI-based analyses in Fig. 15 of Wolfensberger et al. (2015). The distributions in Trömel et al. (2017) are narrower than those in Wolfensberger et al. (2015) due to the resolution differences in QVP vs. RHI methodologies. Also, the Wolfensberger et al. (2015) analyses include negative Z_{DR} and K_{DP} measurements that are not physically

relevant and are likely attributed to statistical errors in the RHI data. In general, implementation of the QVP methodology produces more narrow histograms and more accurate quantification of polarimetric variables compared to those using RHI methodology.

In Fig. 4.2, the distribution of maximum Z_H in the ML ranges from -10 to 50 dBZ, with an overall average of 25 dBZ (Fig. 4.2a), and maximum Z_{DR} in the ML ranges between ~0 and 4 dB, with an average of 1.5 dB (Fig. 4.2b). Also, Fig. 4.2d illustrates corresponding minimum ρ_{hv} in the ML between 0.73 and 1.0, with an overall average of 0.94. Aside from the inclusion of data for $Z_H < 0$ dBZ, the shapes and mean values of the Z_H, Z_{DR}, and ρ_{hv} distributions closely agree with those documented at X band by Wolfensberger et al. (2015) and Trömel et al. (2017). Comparing the results in Fig. 4.2a,b,d, Fig. 15 in Wolfensberger et al. (2015), and Fig. 8 in Trömel et al. (2017), the Z_H distributions are noticeably skewed toward higher Z_H near 30 dBZ, while the greatest densities for Z_{DR} occur between 0 and 2 dB, and the ρ_{hv} distributions peak near 0.95. In Fig. 4.2c, maximum K_{DP} in the ML ranges between -0.01 and 0.22° km^{-1} with an average of 0.03° km^{-1} both overall and within $Z \geq 20$ dBZ and a comparatively lower mean K_{DP} of 0.004° km^{-1} within low Z_H (likely due to low concentration of pristine crystals). These are the first reliable QVP K_{DP} observations in MLs documented at S band. The K_{DP} distribution is noticeably weighted toward smaller values, with the majority of the dataset occurring between 0 and 0.05° km^{-1}. After scaling and taking into account the difference in radar wavelength, these K_{DP} values are comparable to those documented by Wolfensberger et al. (2015) and are significantly lower than those documented by Trömel

et al. (2017). The shape of the distribution is most similar to that of Wolfensberger et al. (2015), who observed composite mean K_{DP} in the ML of 0.11° km^{-1} with values ranging between approximately -0.5 and 1.5° km^{-1} at X band, and least similar to that of Trömel et al. (2017), whose composite mean K_{DP} in the ML was 0.61° km^{-1} with values ranging from -0.77 to 2.85° km^{-1} at X band. Discrepancy between the K_{DP} magnitudes in Fig. 4.2 and those of Trömel et al. (2017) are likely due to more than the difference in wavelength and could partly be attributed to climatological differences in precipitation. For example, weaker and shallower precipitation systems can produce higher ρ_{hv} in the ML due to smaller snowflakes melting in the ML. The differences could also potentially be affected by the difference in ML detection strategies.

In Fig. 4.2e, the enhancement of Z_H (i.e., ΔZ = maximum Z_H in ML - Z_H in rain) varies between -5.6 and 26 dBZ, with an overall mean of 5.6 dBZ. This suggests that Z_H in the ML is on average 5.6 dBZ greater than that of Z_H in rain, which can be valuable information for improving rainfall estimation in bright band regions. Next, in Fig. 4.2f, remarkably large δ in the ML is observed at S band, ranging between 0.7 and 145° with an overall mean of 29°. δ within $Z_H < 20$ dBZ in the ML ranges between 1.0 and 143°, with a slightly larger mean of 34° (orange line in Fig. 4.2f) compared to that of 27° for δ within $Z_H \geq 20$ dBZ (blue line in Fig. 4.2f), possibly due to more anisotropic particles and less riming occurring above the ML in regions of low Z_H. Wolfensberger et al. (2015) do not include δ analyses, but Trömel et al. (2017) document δ in the ML at X-band, with a mean of 1.8° and maximum values up to 5°, which are dramatically lower than those observed in the present study. However, the shape of the total δ distribution compares well for values

between 0 and 5°, where peak densities occur in both distributions (Fig. 4.2f and Fig. 8 in Trömel et al. 2017). The total δ distribution is skewed toward higher values (i.e., approximately 0 to 60°) within low Z_H regions in the ML and toward lower values (i.e., mostly between 0 and 10°) within regions of larger Z_H in the ML. A potential reason for the remarkably large δ in the ML and stronger ML signatures at S band compared to smaller δ in the ML at X band involves effects of large partially-melted hydrometeors in the Mie regime. According to Trömel et al. (2017), although positive values of δ are most common, negative δ can also occur and the observations of δ are obtained by integrating over the full particle size spectrum. They suggest that, at X band, large negative δ associated with melting particles with sizes of 1.5-1.6 cm in the middle of the ML may cancel out positive δ associated with other hydrometeors, resulting in smaller magnitudes of δ compared to those at S band. They further explain that large δ magnitudes likely result from the occurrence of large, partially-melted snowflakes that increase in size via riming and aggregation microphysical processes.

Lastly, the composite histogram of ML depth in Fig. 4.3 reveals an average ML depth of 560 m, with depths as small as 250 m and as large as approximately 750 m. The shape and magnitude of the distribution are similar to those of Wolfensberger et al. (2015) and Giangrande et al. (2008). Giangrande et al. (2008) observed typical ML thicknesses of approximately 300 m with a long right tail and Wolfensberger et al. (2015) document ML thicknesses ranging between 175 m and 600 m, with an average of 320 m. Other similar statistical observations of ML depth are documented by Bandera et al. (1998) and Durden et al. (1997). Trömel et al. (2017) observed ML thickness values up to approximately 250

m, which is shallower than those of the aforementioned studies, likely attributed to their defining ML thickness as the difference between the heights of the Z_H and Z_{DR} maxima, which is proportional to ML depth. For data within $Z \geq 20$ dBZ, the minimum ML depth of 160 m and maximum ML depth of 1350 m (e.g., Fig. 4.3; blue line) closely compares with that observed by FZ95, who document bright band thicknesses ranging between approximately 150 and 900 m (e.g., Fig. 6 in FZ95), which is expected since our polarimetric ML detection methodology was developed to closely approximate the results of FZ95 curvature method.

2) HIGH δ IN THE ML

As mentioned earlier, one of the most remarkable features of the polarimetric QVP ML data are the very large values of δ observed at S band. As depicted in each of the composite scatterplots in Figs. 4.4a-c, the largest δ in the ML exceeds 100° with maximum values up to 145°, while the majority of the dataset occurs for δ up to 80°, supporting the S-band observations of δ up to 70° by Trömel et al. (2014). Note that non-density composite scatterplots are used here to focus on the extent of the δ values. The orange and blue data points represent ML data for which $Z_H < 20$ dBZ and $Z_H \geq 20$ dBZ, respectively. In Fig. 4.4a, the relationship between maximum δ and maximum Z_H in the ML is depicted. Although the majority of the $\delta > 100°$ values occur for $Z_H \geq 20$ dBZ, there are also a significant number of $\delta > 100°$ data points within very low $Z_H < 20$ dBZ in the ML (Fig. 4.4a). Therefore, very large δ at S band can exist within the ML even in regions of weak Z_H, when a ML signature would not be detected using conventional Z_H data alone.

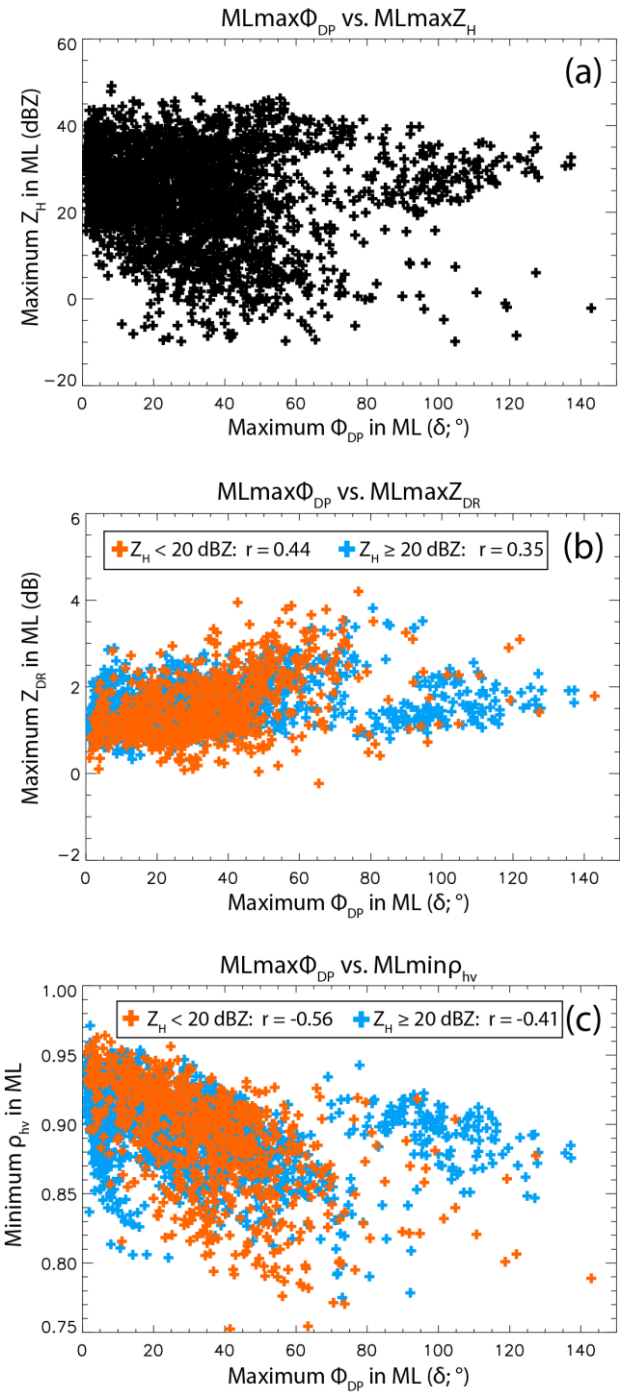

Fig. 4.4: Composite scatterplots of a) maximum Φ_{DP} (i.e., δ) in the ML (°) vs. maximum Z_H in the ML (dBZ), b) δ in the ML vs. maximum Z_{DR} in the ML (dB), and c) δ in the ML vs. minimum ρ_{hv} in the ML, for the 33 QVP ML events. Orange and blue data points represent ML data for which $Z_H < 20$ dBZ and $Z_H \geq 20$ dBZ, respectively. Correlations between the variables (i.e., r) are indicated in each plot for data within $Z_H < 20$ dBZ and $Z_H \geq 20$ dBZ.

However, it is important to note that beam smearing is possibly contributing to the appearance of a deeper layer of maximum Z_{DR}, δ, and minimum ρ_{hv} within the very low Z_H in the ML, as can be seen at ~0000-0300 UTC in Fig. 4.1. Figure 4.4 also illustrates that large δ are well correlated with Z_{DR} and ρ_{hv} in the ML. For example, in Fig. 4.4b, positive correlation ($r = 0.44$ for $Z_H < 20$ dBZ and $r = 0.35$ for $Z_H \geq 20$ dBZ) is evident between maximum δ and maximum Z_{DR} in the ML, with larger δ generally occurring for larger Z_{DR}. Specifically, Z_{DR} ranges between 0 and 4 dB within δ up to 145°. These results support those of Trömel et al. (2013, 2017), who observed strong interdependence between maximum Z_{DR} and δ in the ML at X band. In Fig. 4.4c, maximum δ and minimum ρ_{hv} in the ML exhibit correlations of -0.56 and -0.41 for $Z_H < 20$ dBZ and $Z_H \geq 20$ dBZ, respectively, with ρ_{hv} ranging between approximately 0.75 and 0.97 for δ up to 145°. It is expected that excluding the outlying cluster of data for which $\delta > 80°$ would result in stronger correlations in Figs. 4.4b,c. Overall, the larger Z_{DR} and lower ρ_{hv} in the ML generally occur with larger δ (Figs. 4.4b-c), potentially indicating efficient aggregation above the ML (Fridlind et al. 2017; Trömel et al. 2014; Ryzhkov et al. 2016) and larger-sized partially melted snowflakes in the ML (Trömel et al. 2013, 2014), as the ice particles become water coated and more oblate as they fall through the ML. Indeed, Fig. 4.1 provides evidence of larger δ, larger Z_{DR}, and reduced ρ_{hv} in the ML during larger Z_{DR} above the ML (e.g., between 2.5 and 3.5 km at 0008-0027 UTC), likely resultant of oblate pristine crystals falling from the DGL above. Furthermore, since unrimed snow produces much larger δ than rimed snow (e.g., Trömel et al. 2014), the very large δ in Figs. 4.4a-c can be used to generally estimate a minimal degree of riming aloft.

Zrnić et al. (1993) observed δ up to 10-15° for large (>10 mm), oblate, and spongy (water-soaked) aggregates and explain that a significant increase in δ can occur when hydrometeors are large enough to scatter in the resonant regime. They also explain that if an aggregate is coated with a sufficient amount of water (i.e., if thickness of the water coating is 10% of the particle's radius), the resultant polarimetric radar signature is similar to that of an aggregate of the same size that is filled with water (i.e., a liquid hydrometeor; Zrnić et al. 1993). Furthermore, Melnikov et al. (2005) and Melnikov (2012) also discuss δ in the ML and explain possible mechanisms for δ enhancements in the ML, indicating that δ is small for dry ice particles with any oblateness, δ increases with increasing oblateness of wet particles, and δ increases with thicker water coating on oblate particles with ice cores. They also observed $\delta > 10°$ for large and oblate spongy snowflakes.

3) MAXIMUM Z_{DR} vs. MINIMUM ρ_{hv} IN THE ML

Figure 4.5 presents a composite density scatterplot of maximum Z_{DR} in the ML vs minimum ρ_{hv} in the ML. Maximum Z_{DR} ranges from 0 to 4 dB, with corresponding minimum ρ_{hv} between approximately 0.75 and 0.97. The majority of the dataset is represented by ρ_{hv} between approximately 0.86 and 0.95 and Z_{DR} between 0.5 and 1.75 dB, as is evidenced by the deeper blue colors representing the largest densities of data points. As expected, a prominent strong negative correlation (i.e., r = -0.65) exists between the variables. As ice particles begin to melt as they fall through the ML, they become water coated and the larger partially-melted snowflakes result in increased Z_{DR} and reduced ρ_{hv} in the ML.

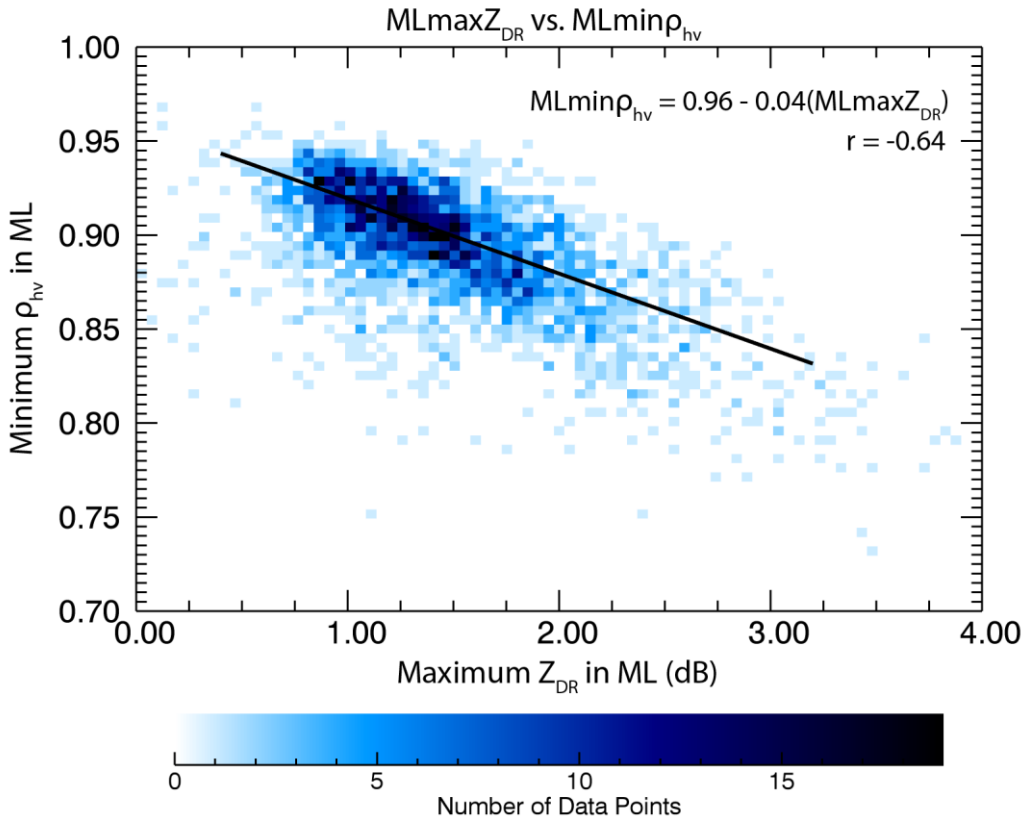

Fig. 4.5: Composite density scatterplot of maximum Z_{DR} in the ML (dB) vs. minimum ρ_{hv} in the ML for the 33 QVP ML events. Strong negative correlation (r = -0.65) occurs between these variables as ice particles begin to melt as they fall through the ML and become more oblate as they become water coated.

4) TWO ML REGIMES

Another significant and repetitive feature of the 33 QVP ML events is the occurrence of two ML regimes. As previously demonstrated in the KFFC 11 February 2014 9.9° QVP in Fig. 4.1, a region of higher Z_H distinctly indicates the presence and location of a ML, collocated with enhanced Z_{DR}, reduced ρ_{hv} and enhanced Φ_{DP} (or δ) in a layer between approximately 2 and 2.5 km (Figs. 4.1a,b,c,d). On the other hand, prior to about 0300 UTC, a well-defined ML is difficult to discern from approximately 0000-0300 UTC using Z_H alone. During this period of weak Z_H (< 20 dBZ), the ML is only

identifiable in the polarimetric imagery where a distinct ML signature is clearly evident in the Z_{DR}, ρ_{hv}, and Φ_{DP} fields (e.g., Figs. 4.1b, c, and d, respectively). Here, the reduced Z_H and enhanced Z_{DR}, ρ_{hv}, and Φ_{DP} indicate a very small concentration of small hydrometeors including pristine crystals such as dendrites (0.01-1 mm diameters; Straka et al. 2000), plates (0.01-3 mm diameters; Straka et al. 2000), or needles that contribute to the enhanced Z_{DR} due to their lower aspect ratios. The small concentration of these small crystals and a lack of larger aggregates suggest an absence of aggregation, while the smaller particle sizes and their resultant quick melting produce a very shallow ML.

The two ML regimes are also evident in the composite density scatterplot in Fig. 4.6, which displays the relationship between maximum Z_{DR} in the ML and Z_{DR} in rain (i.e., 300 m below the bottom of the ML). Two distinct branches of data demonstrate the higher Z_{DR} that corresponds with low Z_H in the ML and the Z_{DR} values that correspond to the higher Z_H in the ML (Fig. 4.6). If the data for low $Z_H < 20$ dBZ are filtered out, a strong relationship between maximum Z_{DR} in the ML and Z_{DR} in rain is evident (not shown), with higher Z_{DR} in the ML occurring with higher Z_{DR} in rain. This strong relationship is potentially valuable for improving future rainfall estimation in bright band regions, particularly at more distant ranges from the radar. Further evidence of the two ML regimes is provided in Fig. 4.7, which illustrates the non-monotonic dependence of Z_{DR} on Z_H in the ML. When maximum Z_H in the ML ranges between approximately -10 and 20 dBZ, larger Z_{DR} of 0 to 4 dB occurs as pristine, non-aggregated crystals fall through the ML. During larger maximum Z_H in the ML (i.e., > 20 dBZ), a stronger relationship is apparent

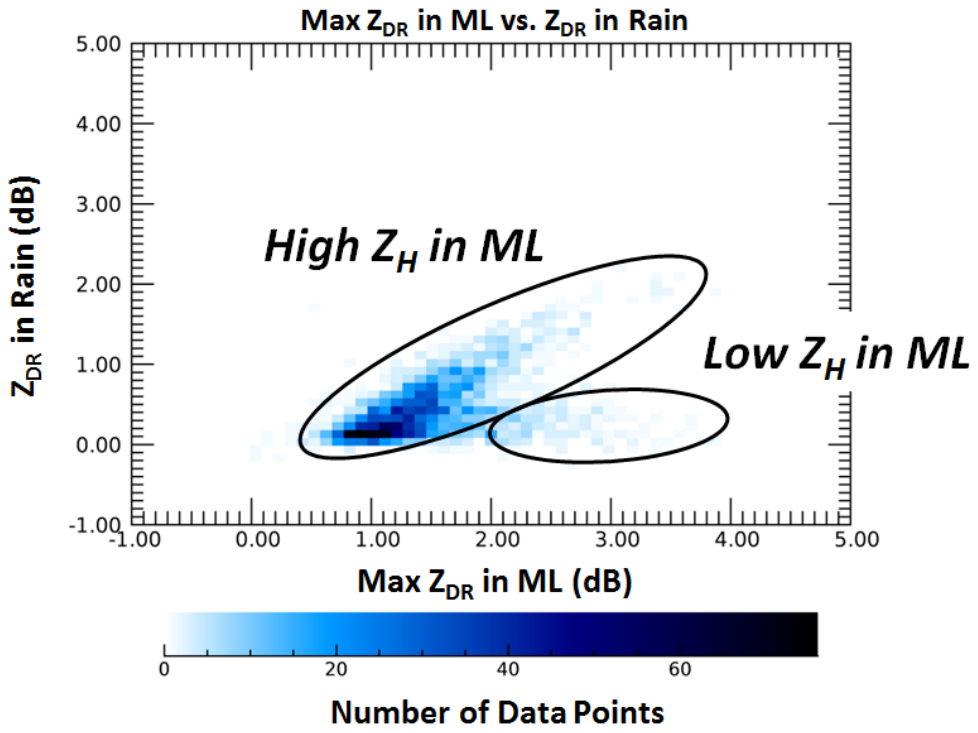

Fig. 4.6: Composite density scatterplot of maximum Z_{DR} in the ML vs. Z_{DR} in rain for the 33 QVP ML events. Two ML regimes are evident: 1) Lower Z_{DR} corresponding to higher Z_H in the ML, resulting in a distinct ML, and 2) Higher Z_{DR} corresponding to low Z_H in the ML (< ~20 dBZ) where the ML is only identifiable in polarimetric imagery. In the second region, there is a small concentration of small hydrometeors including crystals such as dendrites and plates, resulting in higher Z_{DR}.

as larger Z_H generally coincides with increasing Z_{DR} in the ML. Overall, there is ample evidence that polarimetric radar data are much more valuable for detecting ML microphysical processes than conventional reflectivity data alone, particularly in regions of low Z_H.

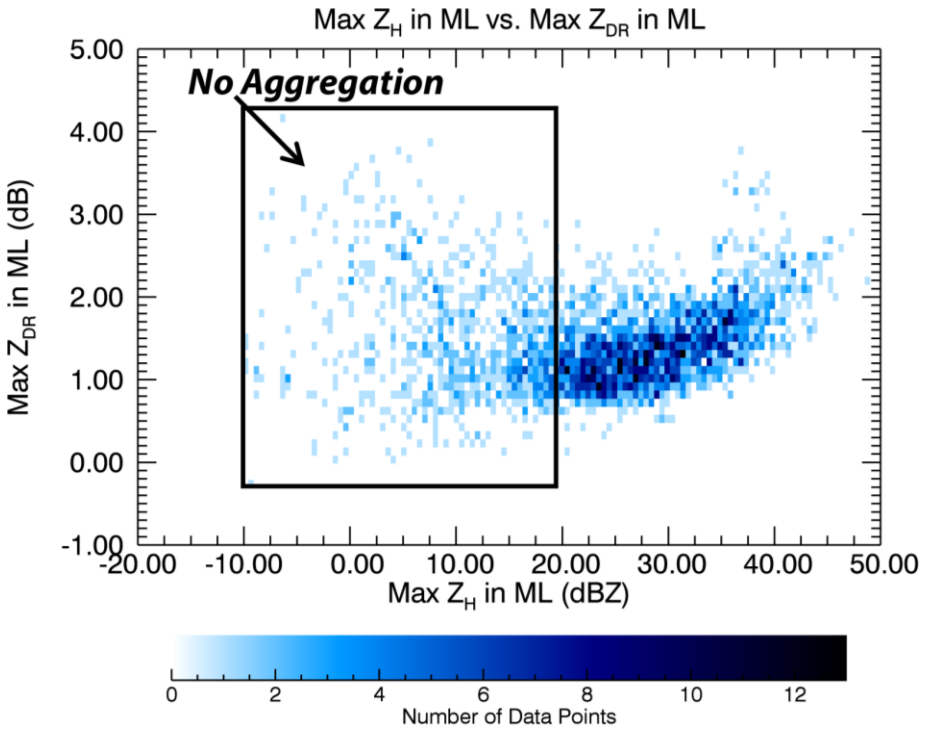

Fig. 4.7: Composite density scatterplot of maximum Z_H in the ML (dBZ) vs. maximum Z_{DR} in the ML (dB) for the 33 QVP ML events. Low Z_H in the ML (< ~20 dBZ) occurs during larger Z_{DR} in the ML (~ 0-4 dB) when pristine, non-aggregated ice falls through it. The increase in Z_H in the ML during the increase in maximum Z_{DR} in the ML indicates the oblateness of particles increases as they become water coated through melting.

5) RELIABLE K_{DP} MEASUREMENTS IN THE ML

Another feature of this investigation is the reliable estimation of K_{DP} in the ML, documented for the first time at S band. Statistics of K_{DP} in the ML are important because K_{DP} is expected to be better correlated with precipitation flux than Z_H and Z_{DR}, which are weighted by large wet aggregates, while K_{DP} is more weighted by small melting snowflakes and resulting raindrops and may be directly utilized for rainfall estimation in regions of bright band contamination (Borowska et al. 2011; Trömel et al. 2017). Figure 4.8 presents a composite density scatterplot demonstrating a strong positive correlation

(i.e., 0.63) between maximum K_{DP} (up to 0.22° km^{-1}) and maximum Z_H (-10 to 50 dBZ) in the ML, with the greatest concentration of data occurring for larger K_{DP} ranging between approximately 0 and 0.1° km^{-1} within larger Z_H > 20 dBZ. This strong relationship validates the reliability and confidence in the QVP processing routine implemented for K_{DP} estimation in the ML. Trömel et al. (2017) also observed a strong relationship between K_{DP} and Z_H in the ML for the first time at X band, with a correlation of 0.58. Therefore, it is evident that K_{DP} measurements in the ML can confidently be used to examine ML microphysical processes and in turn optimize future microphysical models.

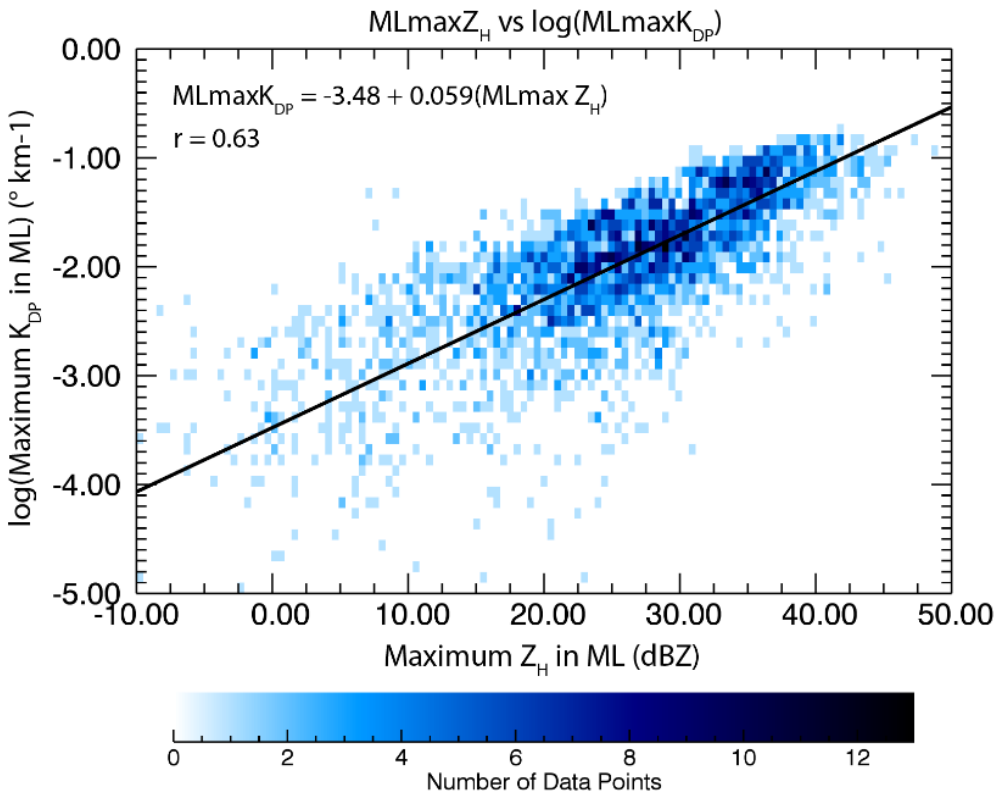

Fig. 4.8: Composite density scatterplot featuring a strong positive correlation (r = 0.63) between maximum Z_H in the ML (dBZ) and log(maximum K_{DP} in the ML;° km^{-1}) for the 33 QVP ML events (at S band). These results reveal that K_{DP} in the ML can be reliably measured.

6) ML STATISTICS VALUABLE FOR PVPR AND QPE

Figures 4.9 and 4.10 reveal statistics that are valuable for developing a PVPR technique that can help improve representation of ML microphysics in NWP models and also improve polarimetric QPE in rain. In Fig. 4.9a, a very strong correlation (i.e., 0.96) between maximum Z_H in the ML and Z_H in rain (i.e., 0.3 km below the bottom of the ML) is presented, with larger maximum Z_H in the ML of -10 to 50 dBZ occurring with larger Z_H in rain up to 40 dBZ. The majority of the data points occur for maximum Z_H in the ML between 10 and 40 dBZ and Z_H in rain between 10 and 30 dBZ. Trömel et al. (2017) also observed strong correlation (i.e., 0.94) between these variables at X band (e.g., Fig. 3 in Trömel et al. 2017). Expectedly, the strong correlation between these variables indicates that Z_H measurements in the ML can be confidently used to estimate precipitation intensity near the surface. Furthermore, in Fig. 4.9b, a strong correlation (i.e., 0.88) exists between Z_H in snow (i.e., 0.3 km above the ML top) and Z_H in rain, with larger values of Z_H above the ML occurring during larger Z_H below the ML. Also, the greatest densities of data points occur between approximately 10 and 30 dBZ. These results suggest that larger measurements of Z_H above the ML can indicate greater Z_H near the surface. Essentially, a higher concentration of snowflakes just above the ML can lead to more snowflakes falling into the ML and thus a higher concentration of raindrops falling below.

Figure 4.10 illustrates statistical correlations of the ML that are particularly important for developing a PVPR technique to mitigate the impact of ML contamination on QPE. Fig. 4.10a reveals that negative correlation occurs between minimum ρ_{hv} in the ML and the corresponding enhancement of Z_H (i.e., $\Delta Z_H = Z_{Hmax} - Z_{Hrain}$). Greater

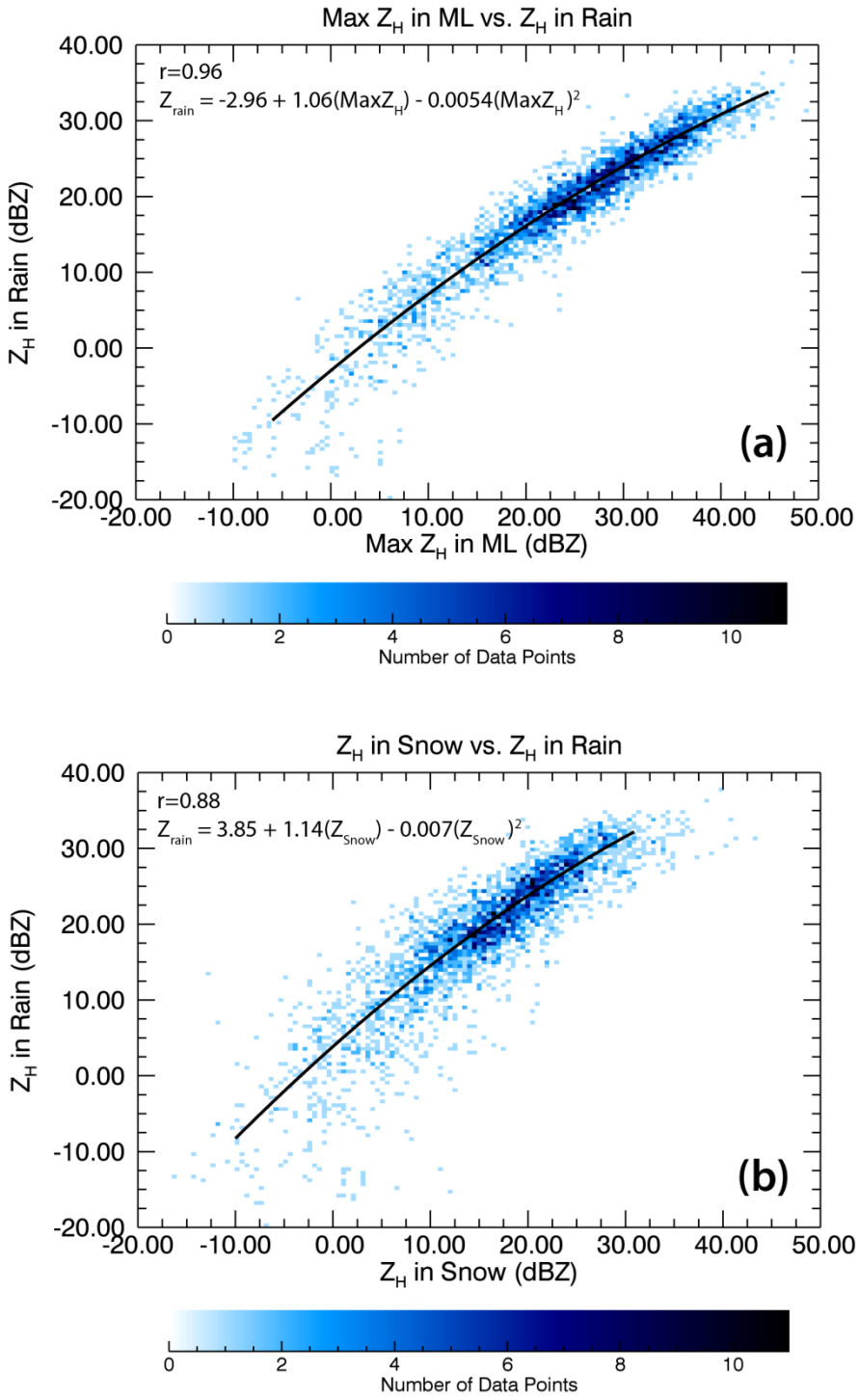

Fig. 4.9: Composite density scatterplots of a) maximum Z_H in the ML vs. Z_H in rain (dBZ) and b) maximum Z_H in snow vs. Z_H in rain (dBZ), for the 33 QVP ML events. Correlations between the variables are indicated in each panel. Note: Z_H in rain = Z_H at 0.3 km below ML bottom and Z_H in snow = Z_H at 0.3 km above ML top.

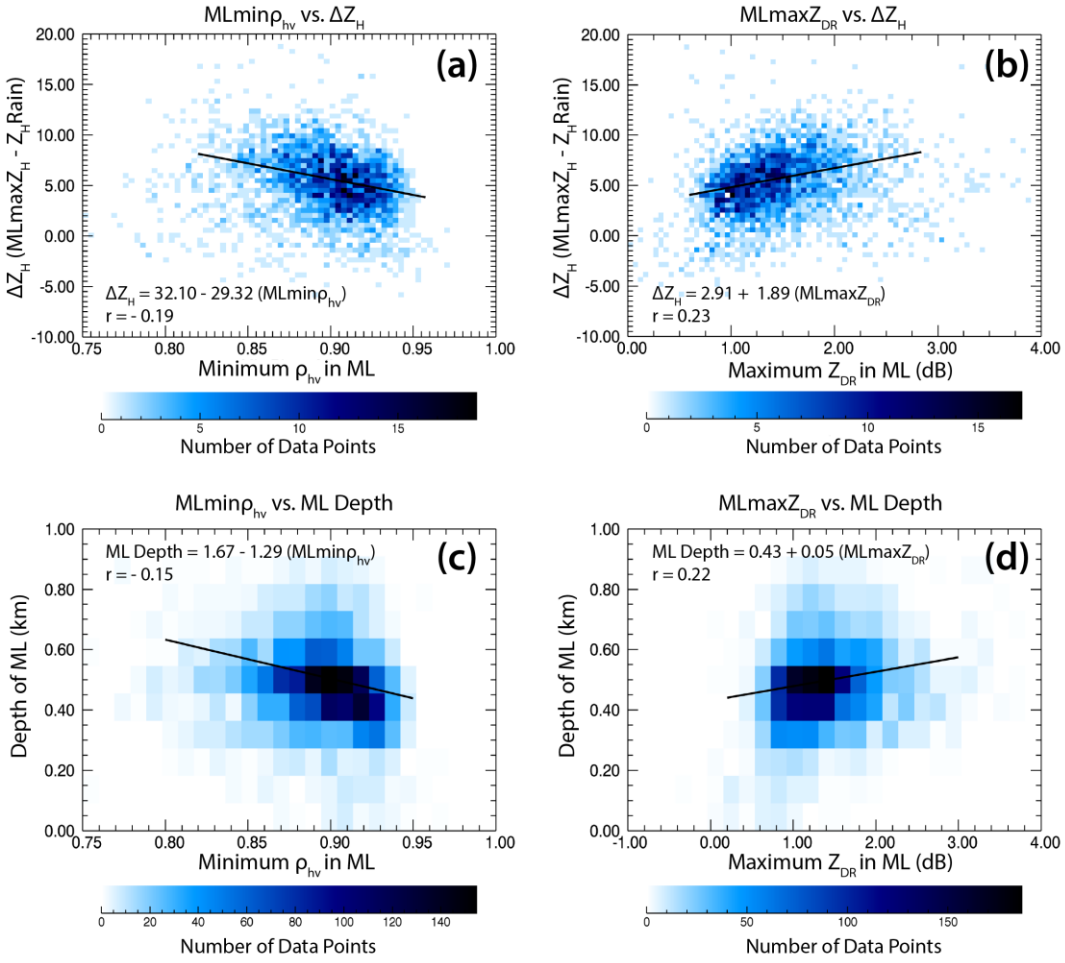

Fig. 4.10: Composite density scatterplots of a) minimum ρ_{hv} in the ML vs. ΔZ_H (dBZ), b) maximum Z_{DR} in the ML (dB) vs. ΔZ_H, c) minimum ρ_{hv} in the ML vs. ML depth (km), and d) maximum Z_{DR} in the ML vs. ML depth, for the 33 QVP ML events. Note: ΔZ_H = (maximum Z_H in the ML) – (Z_H in rain).

differences between Z_{Hmax} in the ML and Z_{Hrain} are generally associated with lower minimum ρ_{hv} in the ML, which bolsters the results of Trömel et al. (2017) at X band. Also, in Fig. 4.10b, a positive correlation exists between maximum Z_{DR} in the ML and ΔZ_H, with greater Z_{DR} in the ML generally occurring alongside greater ΔZ_H. The depth of the ML (i.e., difference between height of ML top and height of ML bottom) is also

negatively correlated with minimum ρ_{hv} in the ML, with greater ML depths generally occurring during lower minimum ρ_{hv} in the ML (Fig. 4.10c). This supports the strong correlation (i.e., -0.52) between minimum ρ_{hv} in the ML and ML thickness observed by Trömel et al. (2017; their Fig. 5). However, since they define ML thickness as the difference between the heights of the Z_H and Z_{DR} maxima, this may explain the discrepancy in correlations between their study and the present study. Lastly, Fig. 4.10d illustrates low correlation between ML depth and maximum Z_{DR} in the ML, with larger Z_{DR} in the ML generally occurring during larger ML depths. Overall, these polarimetric statistics in the ML provide important information on microphysical properties within and near the ML and how they relate to the behavior of precipitation at the surface, which can ultimately help improve the accuracy of polarimetric QPE in rain.

4. Discussion

The QVP polarimetric statistics presented in Section 3 are valuable for advancing understanding of the relation of polarimetric signatures in the ML to the underlying physical processes of precipitation formation and evolution throughout the depth of a cloud. It is important to note the main differences between this study, which examines polarimetric characteristics of the ML at S band, and that of Trömel et al. (2017), which presented polarimetric characteristics of the ML at X band. The studies also differ in that the dataset examined by Trömel et al. (2017) was obtained in different a climatic regime than that presented here, which can impact the depth of precipitation, ice supersaturations, and resultant microphysical processes. We also attempt to provide more in-depth

discussions of the methodology used to detect the top and bottom of the ML, the computation and physical interpretation of the large δs observed at S band in the ML, and microphysical processes occurring in regions of low Z_H in the ML.

As described previously, using our polarimetric model of the ML, distinct polarimetric indications of a ML are frequently detected in regions of low Z_H, where a well-defined ML is indiscernible using conventional Z_H data alone (e.g., at ~0000-0300 UTC in Fig. 4.1, but also observed in many other events). The polarimetric signatures in these regions provide insight into the types of crystals and ice microphysical processes occurring within and above the ML during these periods. Large Z_{DR} (up to 4 dB), remarkably large δ (up to 145°), low K_{DP} (near 0° km^{-1}), and very low ρ_{hv} (down to 0.8) associated with the low Z_H (-10 to 20 dBZ) in the ML likely indicate partial melting of pristine, non-aggregated crystals with very anisotropic shapes and higher densities than isometric-type ice (e.g., Schrom and Kumjian 2016; Griffin et al. 2018). In particular, the low Z_H, low K_{DP}, and high Z_{DR} (e.g., Fig. 4.1) suggest the concentration of ice particles is low and that pristine crystals dominate, resulting in a narrow particle spectrum and a lack of aggregation. This is attributed to Z_{DR} being dependent on particle shape, density, and orientation and being independent of number concentration. Since Z_{DR} represents the ratio of reflectivity factors at horizontal and vertical polarizations, denser and non-spherical oblate pristine crystals with very low aspect ratios, such as dendrites, plates or needles, therefore produce larger Z_{DR}. K_{DP} is dependent on particle shape, density, orientation, as well as number concentration; hence the K_{DP} is low within the low concentration of crystals. These signatures suggest the generation of small, but oblate, pristine crystals

within the DGL above, which then fall into the ML without being aggregated and then evaporate before reaching the surface, as typically evidenced by low Z_H, Z_{DR}, and K_{DP} beneath the ML (e.g., at ~0000-0300 UTC in Fig. 4.1, and at 0000-0130 UTC and 1200-1500 UTC in Fig. 4.11; Griffin et al. 2018). Thus, polarimetric observations in the ML can shed light on the microphysical origin and evolution of crystals as they evolve throughout the depth of the cloud.

On the same note, other strong microphysically-driven connections between polarimetric signatures in the ML and DGL, as well as temperature at the top of the cloud have been observed. For example, enhanced K_{DP} in the ML (up to 0.22° km^{-1}) was frequently found to be associated with enhanced K_{DP} in the DGL during: 1) taller and colder cloud tops, 2) enhanced Z_{DR} and reduced ρ_{hv} in the ML (relative to adjacent times), and 3) sagging of the ML toward the surface (e.g., during ~0600 to 0730 UTC in Fig. 4.1 and during ~2 to 4 UTC in Fig. 4.11). Also, the enhanced K_{DP} in the DGL would sometimes extend down to the ML, indicating enhanced concentration of isometric-type ice above the ML (e.g., ~0600 to 0730 UTC in Fig. 4.1). Figure 4.12 illustrates the strong positive correlation (i.e., r = 0.60) observed between maximum K_{DP} in the DGL and maximum K_{DP} in the ML for all events listed in Table 4.1. Enhanced K_{DP} in the ML is also found to occur during enhanced Z_H in the ML, which is illustrated by the strong linear correlation found between K_{DP} and Z_H in the ML (Fig. 4.8). This is attributed to a greater concentration of isometric-type ice particles above the ML (often indicated by enhanced K_{DP} in the DGL during taller and colder cloud tops; Griffin et al. 2018), which are nucleated at the top of colder clouds and then eventually fall into and become water coated

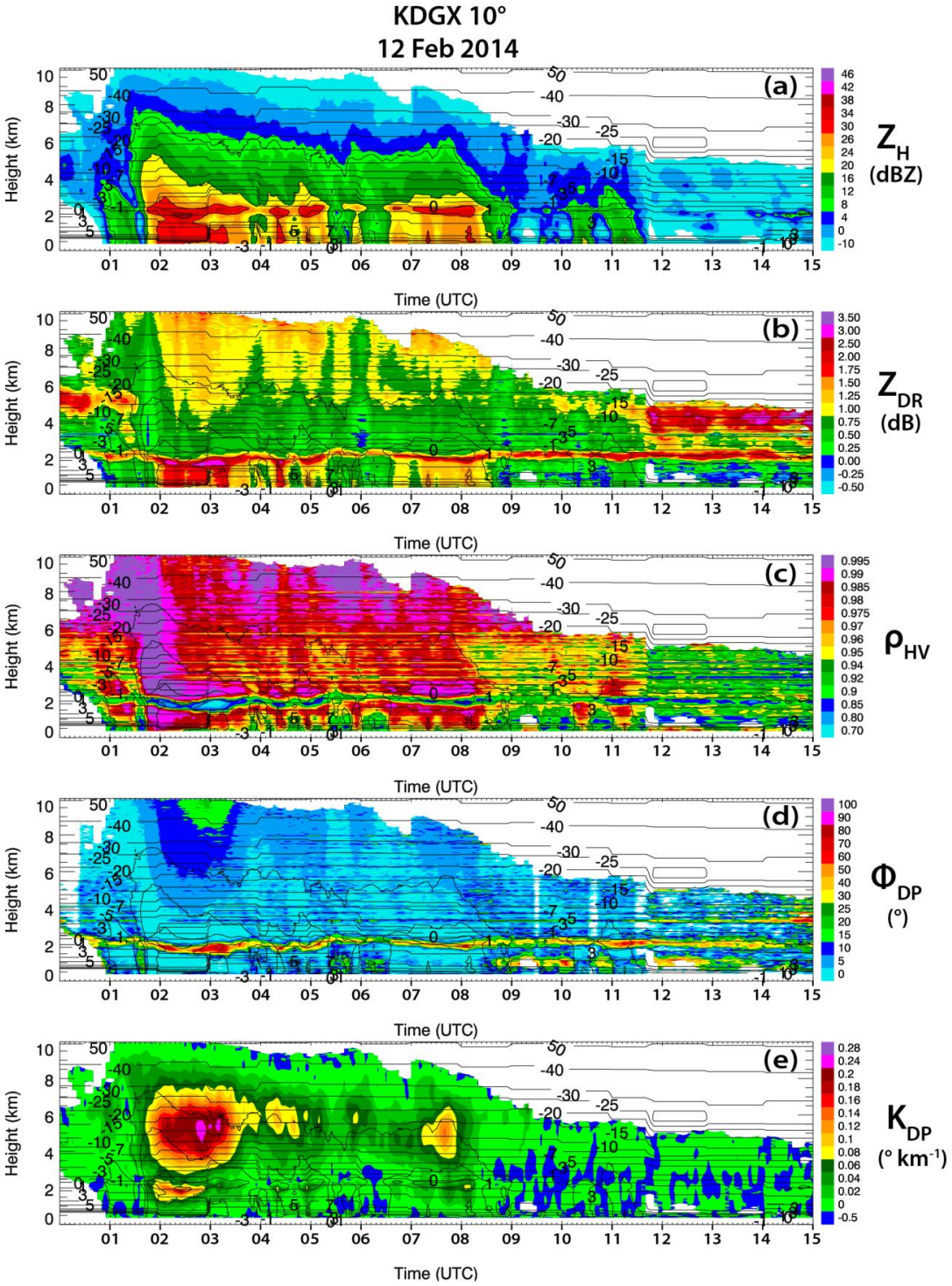

Fig. 4.11: QVPs of a) Z_H (dBZ), b) Z_{DR} (dB), c) ρ_{hv}, d) Φ_{DP} (°), and e) K_{DP} (° km^{-1}) for KDGX from 0006 through 1500 UTC on 12 Feb 2014, at 10° elevation. Contours of HRRR model wet-bulb temperature (°C) are overlaid in each plot. Also, Z_H is contoured at 10, 20, 30, and 40 dBZ.

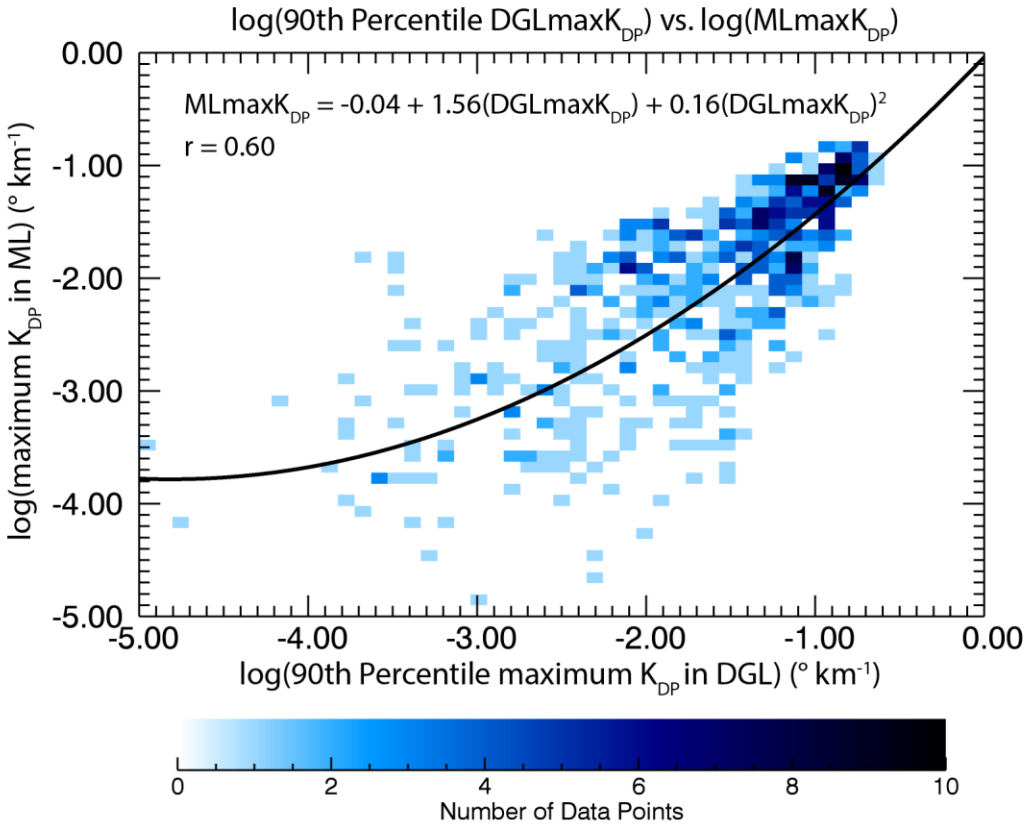

Fig. 4.12: Composite density scatterplot featuring a strong positive correlation (r = 0.60 for a quadratic fit) between log(90th percentile maximum K_{DP} in the DGL) (° km^{-1}) and log(maximum K_{DP} in the ML) for the 33 QVP ML events (at S band).

in the ML. Also, deeper clouds provide greater potential for ice growth and increased ice water content above the ML, enhancing precipitation intensity. These observations are consistent with the recent findings of Carlin (2018), who used a one-dimensional spectral bin model of melting snow (i.e., 1D-MS) to investigate the relation between polarimetric characteristics of modeled MLs and the maximum diabatic cooling rates within them. They discovered that K_{DP} is strongly correlated with diabatic cooling rate due to melting of particles in the ML, which can lead to a dip in ML height. This suggests that accurate K_{DP} measurements can be used to retrieve maximum cooling rate within the ML. Carlin (2018)

also discusses other microphysical processes that could cause sagging bright band signatures, including riming, aggregation, and increased precipitation intensity and the cooling that ensues. In another study, Kumjian et al. (2016) investigate dips in MLs and document that denser, more isometric ice falling into the ML can cause sagging of bright bands, which is significant since rimed particles above the ML can indicate supercooled liquid water that can cause hazardous aircraft icing. In general, the ability to use QVPs to reliably estimate K_{DP} in the ML for the first time (e.g., Trömel et al. 2017; Griffin et al. 2018) combined with the understanding of how K_{DP} can be used to estimate ML cooling rates allows for potential improvement to Z_H-based ML cooling rate estimation methods (e.g., Carlin 2018) and a better understanding of the causes of bright band sagging.

Quantification of polarimetric variables in and above the ML not only provide details of the complexity of ML microphysics and what they reveal about ice processes above, but can also be used to relate elevated microphysical processes to precipitation characteristics near the surface, helping to better inform numerical weather prediction models. For example, since K_{DP} in the ML is strongly correlated with Z_H in the ML (e.g., Fig. 4.8) and Z_H in the ML is strongly correlated with Z_H in rain (e.g., Fig. 4.9a), reliable K_{DP} measurements in the ML can be used to improve estimation of Z_H in rain, leading to improvements in existing polarimetric QPE algorithms. Furthermore, measurements of δ in the ML give important information on the non-Rayleigh or resonance scattering characteristics of large particles (e.g., Ryzhkov et al. 2016), thereby providing valuable information on the dominant particle sizes within the ML. For example, during periods of large δ in the ML, a minimal degree of riming is expected aloft, since δ is likely

proportional to the maximal size of snow falling through the ML and unrimed snow produces much larger δ than rimed snow (e.g., Trömel et al. 2014). Furthermore, relationships between δ and Z_{DR} have been suggested in the literature (e.g., Otto and Russchenberg 2011; Schneebeli and Berne 2012; Trömel et al. 2013), as they both depend on particle size. Since Z_{DR} in the ML is strongly correlated with Z_{DR} in rain (e.g., Fig. 4.6) and Z_{DR} is proportional to the D_m of hydrometeors, observations of Z_{DR} in the ML can potentially be used to estimate D_m in rain. Z_{DR} and δ enhancements in the ML can therefore help identify and predict changes in hydrometeor sizes and drop size distributions at the surface.

5. Summary

This study implements quasi-vertical profiles (QVPs) obtained from a large-scale database of U.S. WSR-88D S-band radar data to document the polarimetric characteristics of the ML in 33 cold-season precipitation events with high vertical resolution and improved statistical accuracy. A polarimetric technique to define the top and bottom of the ML is first introduced. The heights of the ML top and ML bottom are determined using ρ_{hv} and δ thresholds and then compared to those found by Fabry and Zawadski (1995) who use a reflectivity-based curvature method. The curvature and polarimetric methods compare well everywhere except within regions of low Z_H, where the FZ95 curvature method is not able to detect MLs. Using the QVPs, statistical relationships are developed to gain insight into the evolution of microphysical processes above, within, and below the

ML, leading to a statistical polarimetric model of the ML that reveals characteristics that reflectivity data alone are not able to provide, particularly in regions of weak Z_H.

A significant and repetitive feature of the events studied is the occurrence of two ML regimes. Regions of higher Z_H distinctly indicate the presence and location of a ML collocated with enhanced Z_{DR}, reduced ρ_{hv} and enhanced δ while at other times a well-defined ML is difficult to discern using Z_H alone (e.g., Fig. 1). During the periods of weak Z_H (i.e., < 20 dBZ), the ML is only identifiable in the polarimetric imagery where a distinct ML signature is clearly evident in the Z_{DR}, ρ_{hv}, and Φ_{DP} fields. Here, a very low concentration of pristine crystals is believed to prevent aggregation. Therefore when the crystals melt, there is little-to-no associated bright band signature in the Z_H imagery. For $Z_H \geq 20$ dBZ, a strong positive relationship between maximum Z_{DR} in the ML and Z_{DR} in rain exists, with higher Z_{DR} in the ML occurring during higher Z_{DR} in rain. This is potentially valuable for improving future rainfall estimation in bright band regions, particularly at more distant ranges from the radar where ML contamination of the radar beam is most common. Furthermore, a non-monotonic dependence of Z_{DR} on Z_H in the ML is observed. The evidence of very large Z_{DR} (up to 4 dB) and δ (up to 145°) associated with lower Z_H (-10 to 20 dBZ) is documented when pristine, non-aggregated ice falls through the ML. When Z_H in the ML is large (i.e., > 20 dBZ), a stronger relationship between Z_H and Z_{DR} in the ML is observed, as ice particles and aggregates become more oblate as they melt.

Some of the most remarkable features of the polarimetric QVP data are the very large values of δ in the ML at S band, exceeding 100° with maximum values up to 145°.

The large δ is well correlated with Z_{DR} and ρ_{hv} in the ML and is observed not only within enhanced Z_H, but even in regions of weak Z_H, when a ML signature would not be detected using conventional Z_H data alone. Larger Z_{DR} and lower ρ_{hv} in the ML generally occur with larger δ, indicating efficient aggregation above the ML and larger-sized partially melted snowflakes in the ML. We also present the first reliable QVP observations of K_{DP} in MLs at S band, which reveal strong positive correlation (i.e., r = 0.63) between maximum K_{DP} and maximum Z_H in the ML. This provides valuable evidence of the reliability and confidence in the QVP processing routine implemented for K_{DP} estimation in the ML.

Results also indicate strong positive correlation (i.e., 0.88 and 0.96, respectively) between Z_H in rain (i.e., 0.3 km below ML) and Z_H in snow (i.e., 0.3 km above ML) and between Z_H in rain and maximum Z_H in the ML. Expectedly, this indicates that Z_H measurements in and above the ML can be confidently used to estimate precipitation intensity near the surface. Also, negative correlation occurs between minimum ρ_{hv} in the ML and the corresponding enhancement of Z_H (i.e., $\Delta Z_H = Z_{Hmax} - Z_{Hrain}$), with greater ΔZ_H generally associated with lower minimum ρ_{hv} in the ML. Positive correlation exists between maximum Z_{DR} in the ML and ΔZ_H, with greater Z_{DR} in the ML generally occurring during greater ΔZ_H. Also, greater ML depths generally occur during lower minimum ρ_{hv} in the ML. These ML statistics are particularly important for developing a PVPR technique to mitigate the impact of ML contamination on polarimetric QPE.

Lastly, a microphysically-driven connection has been found between polarimetric signatures in the ML and aloft in the DGL and the temperature at the top of the cloud.

Observations of high K_{DP} in the ML is typically associated with sagging bright bands during colder cloud top temperatures, enhanced concentration of isometric-type crystals above the ML, and enhanced K_{DP} in the dendritic growth layer (DGL; between -10 and -20°C). Also, a strong positive correlation (i.e., 0.60) between K_{DP} in the DGL and K_{DP} in the ML is observed. Overall, the results of this analysis provides a next step toward advancing understanding of ML microphysical processes in cold season precipitation, and demonstrates the value and reliability of QVPs in detecting key features in ML regions of clouds. Considering that polarimetric radar variables in the ML are poorly represented in numerical weather prediction models, we believe that statistical analyses of polarimetric signatures in and near the ML such as those presented here have the potential to lead to improved model parameterizations, as well as a better general understanding of microphysical processes above, within, and beneath the ML and how they are related to the behavior of precipitation at the surface.

Chapter 5: Summary and Future Work

With the completion of the upgrade of the WSR-88D radar network to polarimetric capabilities in 2013, a wealth of dual-polarization radar data became available for regions of the country never before sampled by polarimetric radar. To investigate the value of these data in inferring different microphysical processes in winter storms, a large-scale database was compiled to record polarimetric and surface precipitation type observations in a variety of winter precipitation events. These data exhibit several recurring polarimetric signatures. It is important to understand what these signatures reveal about precipitation physics since better physical interpretations of polarimetric observations can help to improve understanding of precipitation formation and evolution throughout the depth of a cloud, as well as to better inform NWP models and forecasts through optimizing assimilation of polarimetric radar data.

This dissertation contributes to these efforts by first investigating the evolution and nature of intriguing polarimetric signatures observed during the historic 8-9 February 2013 Northeast blizzard, and examining them in light of the thermodynamic environment within which they developed and the apparent microphysical processes that were active when they appeared. Polarimetric data (from the S-band KOKX radar) were analyzed alongside RAP model wet-bulb temperature analyses, as well as surface precipitation type observations from both mPING and the NWS Forecast Office in Upton, New York, for interpretation of the polarimetric signatures. The storm exhibited unique polarimetric signatures, some of which have never before been documented for a winter system. Reflectivity values were unusually large, reaching magnitudes >50 dBZ and reaching as high as 60 dBZ in shallow

regions of heavy wet snow near the surface. The 0°C transition line was exceptionally distinct in the polarimetric imagery, providing detail that was often unmatched by the numerical model output. During this event, the polarimetric observations were critical for accurately assigning the transition from liquid to frozen precipitation, illustrating how dual-polarization radar data could be a potentially valuable tool for forecasters when nowcasting transitional winter precipitation. Other features observed include differential attenuation of magnitudes typical of melting hail, depolarization streaks that provide evidence of electrification, nonuniform beamfilling, a "snow flare" signature, and localized downward excursions of the ML collocated with observed transitions in surface precipitation types. Also, in agreement with previous studies, widespread elevated depositional growth layers, located at temperatures near the model-predicted -15°C isotherm, appear to be correlated with increased snowfall and large reflectivity factors near the surface.

A more climatological and quantitative analysis was then conducted using a new QVP methodology to investigate the microphysical evolution and significance of polarimetric signatures and their statistical correlations observed in a selection of winter events. QVPs of transitional stratiform and pure snow precipitation are analyzed at high elevation angles (i.e., 9.9°–19.5°) using WSR-88D S-band data, alongside their corresponding environmental thermodynamic HRRR model analyses. QVPs of K_{DP} and Z_{DR} are implemented to demonstrate their value in interpreting elevated ice processes. The radar data are examined in light of the thermodynamic environment within which they

developed to help deduce their relation to CTT and to identify the types of crystals potentially present throughout the depth of the cloud.

Several repetitive polarimetric signatures are observed in the Z_{DR} and K_{DP} QVPs, in the DGL and at the tops of clouds. The most striking feature is maximum Z_{DR} (up to 6 dB) in the DGL that occurs near the edge of the -10-dBZ Z_H contour within low K_{DP} and during shallower and warmer cloud tops, while maximum K_{DP} (up to 0.3° km^{-1}) in the DGL occurs within low Z_{DR} and during taller and colder cloud tops. Essentially, Z_{DR} and K_{DP} in the DGL are anticorrelated and depend on CTT. Analyses also show correlations indicating larger Z_{DR} within lower Z_H in the DGL and larger K_{DP} within greater Z_H in the DGL. The QVP results can be attributed to distinct polarimetric radar characteristics of isometric (I type) and dendritic (D type) ice particles. The regions of high Z_{DR} are likely dominated by growth of a mixture of highly oblate dendrites and/or hexagonal plates, or prolate needles. Regions of high K_{DP} are expected to be overwhelmed with snow aggregates and crystals with irregular or nearly spherical shapes, seeded at cloud tops. QVP data are also analyzed and compared to in situ microphysical measurements collected by Williams et al. (2013). These datasets verify the ability of the QVP to detect the presence of hexagonal plate crystals within the DGL, demonstrating the reliability of QVPs in evaluating ice microphysics in the upper regions of winter clouds.

QVPs are also implemented to document the polarimetric characteristics of the ML in 33 cold-season winter events. A polarimetric technique to define the top and bottom of the ML using ρ_{hv} and δ thresholds is first introduced. The heights are compared to those found by Fabry and Zawadski (1995) who use a reflectivity-based curvature method. The

curvature and polarimetric methods compare well everywhere except within regions of low Z_H, where the FZ95 curvature method is not able to detect MLs. Using the QVPs, statistical relationships are then developed to gain insight into the evolution of microphysical processes above, within, and below the ML, leading to a statistical polarimetric model of the ML that reveals characteristics that reflectivity data alone are not able to provide, particularly in regions of weak Z_H. A repetitive feature of the QVP ML cases is the occurrence of two ML regimes. Regions of higher Z_H distinctly indicate the presence and location of a ML collocated with enhanced Z_{DR}, reduced ρ_{hv} and enhanced δ while at other times a well-defined ML is difficult to discern using Z_H alone. During these periods of weak Z_H (i.e., < 20 dBZ), the ML is only identifiable in the polarimetric imagery where a distinct ML signature is clearly evident in the Z_{DR}, ρ_{hv}, and Φ_{DP} fields. Here, a low concentration of dendritic-type crystals prevents aggregation, precluding an associated bright band signature in the Z_H imagery.

Results also reveal strong positive correlation between Z_H in rain (i.e., 0.3 km below ML) and Z_H in snow (i.e., 0.3 km above ML), Z_H in rain and maximum Z_H in the ML, and between maximum Z_{DR} in the ML and Z_{DR} in rain. This is potentially valuable for improving future rainfall estimation in bright band regions. Furthermore, a non-monotonic dependence of Z_{DR} on Z_H in the ML is observed; the evidence of very large Z_{DR} (up to 4 dB) and δ (up to 145°) associated with lower Z_H (-10 to 20 dBZ) in the ML is documented when pristine, non-aggregated ice falls through it. During larger Z_H in the ML (i.e., > 20 dBZ), a stronger relationship is apparent as larger Z_H generally coincides with increasing Z_{DR} in the ML, as ice particles and aggregates become more oblate as they melt.

Some of the most remarkable features of the polarimetric QVP ML data are the very large values of δ in the ML at S band, exceeding 100° with maximum values up to 145°. The large δ is well correlated with Z_{DR} and ρ_{hv} in the ML and is observed within enhanced Z_H as well as in regions of weak Z_H, when a ML signature would not be detected using conventional Z_H data alone. Larger Z_{DR} and lower ρ_{hv} in the ML generally occur with larger δ, indicating efficient aggregation above the ML and larger-sized partially melted snowflakes in the ML. The first reliable QVP observations of K_{DP} in MLs documented at S band are also presented, exhibiting strong positive correlation (i.e., 0.63) between maximum K_{DP} and maximum Z_H in the ML. High K_{DP} in the ML typically occurs during sagging bright bands during colder cloud top temperatures, enhanced concentration of isometric-type crystals above the ML, and enhanced K_{DP} in the DGL.

Lastly, negative correlation occurs between maximum Z_{DR} and minimum ρ_{hv} in the ML and between minimum ρ_{hv} in the ML and the corresponding enhancement of Z_H (i.e., $\Delta Z_H = Z_{Hmax} - Z_{Hrain}$). Positive correlation exists between maximum Z_{DR} in the ML and ΔZ_H, with greater Z_{DR} in the ML generally occurring during greater ΔZ_H. Also, greater ML depths generally occur during lower minimum ρ_{hv} in the ML. Quantifying these dependencies is crucial for implementation of a PVPR technique to mitigate the impact of ML contamination on QPE. Overall, considering ML microphysics are poorly represented in NWP models, statistical analyses of polarimetric signatures in and near the ML can help improve parameterization and understanding of microphysical processes above, within, and beneath the ML as well as how they relate to the behavior of precipitation at the surface.

The results of this dissertation provide a next step toward advancing understanding of microphysics in winter clouds and precipitation, and demonstrate the value and reliability of QVPs in detecting key features both in the ML and upper regions of clouds. Future investigations could extend these results to examine MLs and polarimetric indicators of microphysical processes within mesoscale convective systems to diagnose similarities or dissimilarities to that of winter systems. Also, future work is needed to examine in more detail the statistics of Z_{DR} in the DGL and their dependency on ice supersaturation within winter events. Recent statistical analyses of polarimetric DGL data in Germany (personal communication with Alexander Ryzhkov in collaboration with Silke Trömel at the University of Bonn) reveal shallower cold season clouds that seldom reach homogeneous nucleation and exhibit comparatively lower Z_{DR} (typically ~ 2 dB) in the DGL, suggesting dendrites and hexagonal plates in Germany may not become as large as those observed in this study. Relative humidity in the U.S. may differ considerably from that in other countries and may be potentially related to the types of ice present in the DGL. It will be useful to determine whether or not maximum Z_{DR} in the DGL is always positively correlated with ice supersaturation, to better understand any climatological differences in polarimetric DGL statistics.

Ultimately, the findings in this book will help research meteorologists better understand how to utilize polarimetry for hydrometeor identification, to better understand the temporal evolution of polarimetric signatures in different temperature regimes and how they relate to precipitation at the surface, as well as how to optimize parameterization of storm microphysics in numerical models through improved assimilation of polarimetric

radar data. The results of this investigation will also benefit operational meteorologists in warning the public of hazardous winter weather conditions in a more timely and accurate manner. Polarimetry undoubtedly offers a wealth of information that will provide further opportunities for research in the years to come.

References

Andrić, J., M. R. Kumjian, D. S. Zrnić, J. M. Straka, and V. M. Melnikov, 2013: Polarimetric signatures above the melting layer in winter storms: An observational and modeling study. *J. Appl. Meteor. Climatol.,* **52,** 682–700, doi:10.1175/JAMC-D-12-028.1.

Associated Press, cited 2014: Northeast slowly recovering from blizzard. [Available online at http://bigstory.ap.org/article/northeast-trying-get-back-track-after-storm.]

Bailey, M. P., and J. Hallett, 2009: A comprehensive habit diagram for atmospheric ice crystals: Confirmation from the laboratory, AIRS II, and other field studies. *J. Atmos. Sci.,* **66,** 2888–2899, doi:10.1175/2009JAS2883.1.

Balakrishnan, N., and D. S. Zrnić, 1990: Use of polarization to characterize precipitation and discriminate large hail. *J. Atmos. Sci.*, **47**, 1525-1540.

Bandera, J. Papatsoris, A. D., Watson P. A., Tan, J., Goddard, J. W., 1998: Method for detecting the extent of the melting layer. *IET Electr. Lett.*, **11**, 2104-2105, doi:10.1049/el:19981462.

Bechini, R., L. Baldini, and V. Chandrasekar, 2013: Polarimetric radar observations in the ice region of precipitating clouds at C-band and X-band radar frequencies. *J. Appl. Meteor. Climatol.,* **52,** 1147–1169, doi:10.1175/JAMC-D-12-055.1.

Benjamin, S., and Coauthors, 2016: A North American hourly assimilation and model forecast cycle: The Rapid Refresh. *Mon. Wea. Rev.,* **144,** 1669–1694, doi:10.1175/MWR-D-15-0242.1.

Blumberg, W. G., K. T. Halbert, T. A. Supinie, P. T. Marsh, R. L. Thompson, and J. A. Hart, 2017: SHARPpy: An open-source sounding analysis toolkit for the atmospheric sciences. *Bull. Amer. Meteor. Soc.,* **98,** 1625–1636, https://doi.org/10.1175/BAMS-D-15-00309.1.

Borowska, L., Zrnic, D., Ryzhkov, A., Zhang, P., and Simmer, C., 2011: Polarimetric estimates of a 1-month accumulation of light rain with a 3-cm wavelength radar. *Journal of hydrometeorology*, **12**, doi:10.1175/2011JHM1339.1.

Brandes, E., and Ikeda, K., 2004: Freezing-level estimation with polarimetric radar. *J. Appl. Meteor.,* **43**, 1541–1553.

Bringi, V. N., and V. Chandrasekar, 2001: *Polarimetric Doppler Weather Radar: Principles and Applications.* Cambridge University Press, 636 pp.

Carlin, J. T., 2018: The use of polarimetric radar data for informing numerical weather prediction models. Ph.D. dissertation, University of Oklahoma, 274 pp.

Changnon, S. A., 2003: Characteristics of ice storms in the United States. *J. Appl. Meteor.*, **42,** 630-639.

Chen, J., and D. Lamb, 1994: The theoretical basis for the parameterization of ice crystal habits: Growth by vapor deposition. *J. Atmos. Sci.,* **51,** 1206–1222, doi:10.1175/1520-0469(1994)051,1206:TTBFTP.2.0.CO;2.

Cifelli, R., N. Doesken, P. Kennedy, L. D. Carey, S. A. Rutledge, C. Gimmestad, and T. Depue, 2005: The Community Collaborative Rain, Hail, and Snow Network: Informal education for scientists and citizens. *Bull. Amer. Meteor. Soc.,* **86,** 1069–1077, doi:10.1175/BAMS-86-8-1069.

Cortinas, J., Jr., 2000: A climatology of freezing rain in the Great Lakes region of North America. *Mon. Wea. Rev.,* **128,** 3574-3588.

Cortinas, J., Jr., B. C. Bernstein, C. C. Robbins, and J. W. Strapp, 2004: An analysis of freezing rain, freezing drizzle, and ice pellets across the United States and Canada: 1976-90. *Wea. Forecasting,* **19,** 377-390.

DeMott, P., and Coauthors, 2010: Predicting global atmospheric ice nuclei distributions and their impacts of climate. *Proc. Natl. Acad. Sci. USA,* **107,** 11 217–11 222, doi:10.1073/pnas.0910818107.

Doviak, R. J., and D. S. Zrnić, 1993: *Doppler Radar and Weather Observations.* 2nd ed. Academic Press, 562 pp.

Durden, S. L., A. Kitiyakara, I. Eastwood, A. B. Tanner, Z. S. Haddad, F. K. Li, W. J. Wilson, 1997: ARMAR observations of the melting layer during TOGA COARE. *IEEE Trans. Geosci. Remote Sens.,* **35**, 1453-1456.

Elmore, K. L., Z. L. Flamig, V. Lakshmanan, B. T. Kaney, V. Farmer, and L. P. Rothfusz, 2014: mPING: Crowd-sourcing weather reports for research. *Bull. Amer. Meteor. Soc.,* **95,** 1335–1342, doi:10.1175/BAMS-D-13-00014.1.

Fabry, F., and I. Zawadzki, 1995: Long-term radar operations of the melting layer of precipitation and their interpretation. *J. Atmos. Sci.,* **52,** 838-851.

Field, P., R. Hogan, P. Brown, A. Illingworth, T. Choularton, P. Kaye, E. Hirst, and R. Greenway, 2004: Simultaneous radar and aircraft observations of mixed-phase cloud at the 100m scale. *Quart. J. Roy. Meteor. Soc.,* **130A,** 1877–1904, doi:10.1256/qj.03.102.

Findeisen, W., 1940: The formation of the 0°C isothermal layer and fractocumulus under nimbostratus. *Meteor. Z.,* **6,** 882–888.

Forbes, G. S., R. A. Anthes, and D. W. Thompson, 1987: Synoptic and mesoscale aspects of an Appalachian ice storm associated with cold-air damming. *Mon. Wea. Rev.,* **115,** 564-591.

Fridlind, A. M., X. Li, D. Wu, M. van Lier-Walqui, A.S. Ackerman, W.-K. Tao, G.M. McFarquhar, W. Wu, X. Dong, J. Wang, A. Ryzhkov, P. Zhang, M.R. Poellot, A. Neumann, and J.M. Tomlinson, 2017: Derivation of aerosol profiles for MC3E convection studies and use in simulations of the 20 May squall line case. *Atmos. Chem. Phys.*, **17**, 5947-5972, doi:10.5194/acp-17-5947-2017.

Ganetis, S. A., B. A. Colle, M. J. Sienkiewicz, D. M. Schultz, P. L. Heinselman, and D. R. Novak, 2013: Evolution of an intense mesoscale snowband during the 8–9 February 2013 Northeast U.S. blizzard. *15th Conf. on Mesoscale Processes*, Portland, OR, Amer. Meteor. Soc., P16.5. [Available online at https://ams.confex.com/ams/15MESO/webprogram/Paper228054.html.]

Giangrande, S. E., J. M. Krause, and A. V. Ryzhkov, 2008: Automated designation of the melting layer with a polarimetric prototype of the WSR-88D radar. *J. Appl. Meteor. Climatol.,* **47**, 1354-1364.

Giangrande, S., T. Toto, A. Bansemer, M. Kumjian, S. Mishra, and A. Ryzhkov, 2016: Insights into riming and aggregation processes as revealed by aircraft, radar, and disdrometer observations for a 27 April 2011 widespread precipitation event. *J. Geophys. Res. Atmos.,* **121,** 5846–5863, doi:10.1002/2015JD024537.

Griffin, E. M., T. J. Schuur, A. V. Ryzhkov, H. D. Reeves, and J. C. Picca, 2014: A polarimetric and microphysical investigation of the northeast blizzard of 8–9 February 2013. *Wea. Forecasting,* **29,** 1271–1294, doi:10.1175/WAF-D-14-00056.1.

Griffin, E. M., T. J. Schuur, and A. V. Ryzhkov, 2018: A polarimetric analysis of ice microphysical processes in snow, using quasi-vertical profiles. *J. Appl. Meteor. Climatol.,* **57,** 31–50, doi:10.1175/JAMC-D-17-0033.1.

Griffin, E. M., T. J. Schuur, and A. V. Ryzhkov, 2019: A polarimetric radar analysis of ice microphysical processes in melting layers of winter storms using S-band quasi-vertical profiles. Submitted for publication.

Hendry, A., G. McCormick, and B. Barge, 1976: The degree of common orientations of hydrometeors observed by polarization diversity radars. *J. Appl. Meteor.,* **15,** 633–640, doi:10.1175/1520-0450(1976)015,0633:TDOCOO.2.0.CO;2.

Hendry, A., Y. Antar, and G. McCormick, 1987: On the relationship between the degree of preferred orientation in precipitation and dual-polarization radar echo characteristics. *Radio Sci.*, **22,** 37–50, doi:10.1029/RS022i001p00037.

Herzegh, P. H., and A. R. Jameson, 1992: Observing precipitation through dual-polarization radar measurements. *Bull. Amer. Meteor. Soc.,* **73,** 1365–1374, doi:10.1175/1520-0477(1992)073,1365:OPTDPR.2.0.CO;2.

Hickman, B. S., S. Trömel, A. V. Ryzhkov, and C. Simmer, 2017: Radar-driven temperature nudging for nowcasting winter precipitation. Extended abstract, 38th Conference on Radar Meteorology, 28 August – 1 September 2017, Chicago, Illinois, USA.

Hogan, R., P. Field, A. Illingworth, R. Cotton, and T. Choularton, 2002: Properties of embedded convection in warm-frontal mixed-phase cloud from aircraft and polarimetric radar. *Quart. J. Roy. Meteor. Soc.,* **128,** 451–476, doi:10.1256/003590002321042054.

Hogan, R., L. Tian, P. Brown, C. Westbrook, A. Heymsfield, and J. Eastment, 2012: Radar scattering from ice aggregates using the horizontally aligned oblate spheroid approximation. *J. Appl. Meteor. Climatol.*, **51,** 655–671, doi:10.1175/JAMC-D-11-074.1.

Hubbert, J. C., and V. N. Bringi, 2000: The effects of three-body scattering on differential reflectivity signatures. *J. Atmos. Oceanic Technol.,* **17,** 51–61, doi:10.1175/1520-0426(2000)017,0051:TEOTBS.2.0.CO;2.

Hubbert, J. C., S. M. Ellis, M. Dixon, and G. Meymaris, 2010a: Modeling, error analysis, and evaluation of dual-polarization variables obtained from simultaneous horizontal and vertical polarization transmit radar. Part I: Modeling and antenna errors. *J. Atmos. Oceanic Technol.,* **27,** 1583–1598, doi:10.1175/2010JTECHA1336.1.

Hubbert, J. C., S. M. Ellis, M. Dixon, and G. Meymaris, 2010b: Modeling, error analysis, and evaluation of dual-polarization variables obtained from simultaneous horizontal and vertical polarization transmit radar. Part II: Experimental data. *J. Atmos. Oceanic Technol.,* **27,** 1599–1607, doi:10.1175/2010JTECHA1337.1.

Ivic, I., C. Curtis, and S. Torres, 2013: Radial-based noise power estimation for weather radars. *J. Atmos. Oceanic Technol.,* **30,** 2737–2753, doi:10.1175/JTECH-D-13-00008.1.

Kain, J. S., S. M. Goss, and M. E. Baldwin, 2000: The melting effect as a factor in precipitation-type forecasting. *Wea. Forecasting*, **15,** 700–714, doi:10.1175/1520 0434(2000)015,0700:TMEAAF.2.0.CO;2.

Kaltenboeck, R., and A. Ryzhkov, 2017: A freezing rain storm explored with a C-band polarimetric weather radar using the QVP methodology. *Meteor. Z.,* **26,** 207–222, doi:10.1127/metz/2016/0807.

Kalogiros, J., Anagnostou, M. N., Anagnostou, E., Montopoli, M., Picciotti, E., Marzano, F. S., 2013: Correction of polarimetric radar reflectivity measurements and rainfall estimates for apparent vertical profile in stratiform rain. *J. Appl. Meteor. Climatol.,* **52**, 1170–1186, doi:10.1175/JAMC-D-12-0140.1.

Kennedy, P. C., and S. A. Rutledge, 2011: S-band dual-polarization radar observations of winter storms. *J. Appl. Meteor. Climatol.,* **50,** 844–858, doi:10.1175/2010JAMC2558.1.

Korolev, A., and G. Isaac, 2003: Roundness and aspect ratio of particles in ice clouds. *J. Atmos. Sci.,* **60,** 1795–1808, doi:10.1175/1520-0469(2003)060,1795:RAAROP.2.0.CO;2.

Korolev, A., and G. Isaac, and J. Hallett, 2000: Ice particle habits in stratiform clouds. Quart. *J. Roy. Meteor. Soc.,* **126,** 2873–2902, doi:10.1002/qj.49712656913.

Korolev, A., and G. Isaac, S. Cober, J. Strapp, and J. Hallett, 2003: Microphysical characterization of mixed-phase clouds. *J. Roy. Meteor. Soc.,* **129,** 39–65, doi:10.1256/qj.01.204.

Kumjian, M. R., 2013a: Principles and applications of dual-polarization weather radar. Part I: Description of the polarimetric radar variables. *J. Oper. Meteor.,* **1,** 226–242, doi:10.15191/nwajom.2013.0119.

Kumjian, M. R., 2013b: Principles and applications of dual-polarization weather radar. Part II: Warm and cold season applications. *J. Oper. Meteor.,* **1,** 243–264, doi:10.15191/nwajom.2013.0120.

Kumjian, M. R., 2013c: Principles and applications of dual-polarization weather radar. Part III: Artifacts. *J. Oper. Meteor.,* **1,** 265–274, doi:10.15191/nwajom.2013.0121.

Kumjian, M. R., and A. V. Ryzhkov, 2008: Polarimetric signatures in supercell thunderstorms. *J. Appl. Meteor. Climatol.,* **47**, 1940–1961.

Kumjian, M. R., and K. A. Lombardo, 2017: Insights into the evolving microphysical and kinematic structure of northeastern U.S. winter storms from dual-polarization Doppler radar. *Mon. Wea. Rev.,* **145,** 1033–1061, https://doi.org/10.1175/MWR-D-15-0451.1.

Kumjian, M. R., J. C. Picca, S. M. Ganson, A. V. Ryzhkov, and D. S. Zrnić, 2010: Three-body scattering signatures in polarimetric radar data. NOAA/NSSL Rep., 12 pp. [Available online at https://www.nssl.noaa.gov/publications/wsr88d_reports/FINAL_TBSS.doc.]

Kumjian, M. R., H. D. Reeves, and A. V. Ryzhkov, 2011: Polarimetric signatures in winter storms. NOAA/NSSL Rep., 27 pp. [Available online at http://www.nssl.noaa.gov/publications/wsr88d_reports/FINAL2011-Tsk2bPolSigWinter.pdf.]

Kumjian, M., S. Ganson, and A. Ryzhkov, 2012: Freezing of raindrops in deep convective updrafts: A microphysical and polarimetric model. *J. Atmos. Sci.,* **69,** 3471-3490.

Kumjian, M. R., A. V. Ryzhkov, H. D. Reeves, and T. J. Schuur, 2013: A dual-polarization radar signature of hydrometeor refreezing in winter storms. *J. Appl. Meteor. Climatol.,* **52,** 2549–2566, doi:10.1175/JAMC-D-12-0311.1.

Kumjian, M. R., S. A. Rutledge, R. M. Rasmussen, P. C. Kennedy, and M. Dixon, 2014: High-resolution polarimetric radar observations of snow-generating cells. *J. Appl. Meteor. Climatol.,* **53,** 1636–1658, doi:10.1175/JAMC-D-13-0312.1.

Kumjian, M. R., S. Mishra, S. E. Giangrande, T. Toto, A. V. Ryzhkov, and A. Bansemer, 2016: Polarimetric radar and aircraft observations of saggy bright bands during MC3E, *J. Geophys. Res. Atmos.,* **121**, 3584-3607, doi:10.1002/2015JD024446.

Lo, K., and R. Passarelli, 1982: The growth of snow in winter storms: An airborne observational study. *J. Atmos. Sci.,* **39,** 697–706, doi:10.1175/1520-0469(1982)039,0697:TGOSIW.2.0.CO;2.

Martner, B. E., R. M. Rauber, R. M. Rasmussen, E. T. Prater, and M. K. Ramamurthy, 1992: Impacts of a destructive and well-observed cross-country winter storm. *Bull. Amer. Meteor. Soc.,* **73,** 169-172.

Matrosov, S., A. Heymsfield, and Z. Wang, 2005a: Dual-frequency radar ratio of nonspherical atmospheric hydrometeors. *Geophys. Res. Lett.,* **32,** L13816, doi:10.1029/2005GL023210.

Matrosov, S., R. Reinking, and I. Djalalova, 2005b: Inferring fall attitudes of pristine dendritic crystals from polarimetric radar data. *J. Atmos. Sci.,* **62,** 241–250, doi:10.1175/JAS-3356.1.

Matrosov, S. Y., Clar, K. A., Kingsmill, D. E., 2007: A polarimetric radar approach to identify rain, melting layer, and snow regions for applying corrections to vertical profiles of reflectivity. *J. Appl. Meteor. Climatol.,* **46**, 154–166.

Melnikov, A., 2012: Differential phase upon scattering by Rayleigh particles. 7th European Conference on Radar in Meteorology and Hydrology, Toulouse, France.

Melnikov, V., and J. Straka, 2013: Axis ratios and flutter angles of cloud ice particles: Retrievals from radar data. *J. Atmos. Oceanic Technol.,* **30,** 1691–1703, doi:10.1175/JTECH-D-12-00212.1.

Melnikov, A., V. Melnikov, and A. V. Ryzhkov, 2005: On the differential phase in the melting layer. 33rd Conference on Radar Meteorol., Albuquerque, NM, AMS.

Moisseev, D., S. Lautaportti, J. Tyynela, and S. Lim, 2015: Dualpolarization radar signatures in snowstorms: Role of snowflake aggregation. *J. Geophys. Res. Atmos.,* **120,** 12 644–12 665, doi:10.1002/2015JD023884.

NART, cited 2014: News from NOAA in the North Atlantic. North Atlantic Regional Team Newsletter. [Available online at http://www.regions.noaa.gov/north-atlantic/wp-content/uploads/2013/03/NOAA_NART_Spring_2013_newsletter_FINAL.pdf.]

NWA, cited 2014: Update on the February 8–9, 2013 nor'easter/southern New England blizzard. National Weather Association. [Available online at http://www.nwas.org/archive/2013/WinterStorm2013.]

NWS, 2014a: One for the history books, February 11-13, 2014. Peachtree City, GA, Weather Forecast Office, https://www.weather.gov/ffc/20140212_winterstorm.
NWS, 2014b: Winter storm of February 12-13, 2014. Birmingham, AL, Weather Forecast Office, https://www.weather.gov/bmx/winter_02122014.

NWS, 2016: Public information statement: Spotter reports. National Weather Service Raw Text Product, New York, NY, https://mesonet.agron.iastate.edu/wx/afos/p.php?pil5PNSOKX&e5201601232204.

Oraltay, R. G., and J. Hallett, 2005: The melting layer: A laboratory investigation of ice particle melt and evaporation near 0°C. *J. Appl. Meteor.,* **44,** 206–220, doi:10.1175/JAM2194.1.

Otto, T., and H. W. J. Russchenberg, 2011: Estimation of specific differential phase and differential backscatter phase from polarimetric weather radar measurements of rain. *IEEE Geosci. Resmote Sens. Lett.,* **8,** 988-922.

Park, H. S., A. V. Ryzhkov, D. S. Zrnić, and K.-E. Kim, 2009: The hydrometeor classification algorithm for the polarimetric WSR-88D: Description and application to an MCS. *Wea. Forecasting,* **24,** 730–748, doi:10.1175/2008WAF2222205.1.

Picca, J., and A. Ryzhkov, 2012: A dual-wavelength polarimetric analysis of the 16 May 2010 Oklahoma City extreme hailstorm. *Mon. Wea. Rev.,* **140,** 1385–1403, doi:10.1175/MWR-D-11-00112.1.

Picca, J., D. M. Schultz, B. A. Colle, S. Ganetis, D. R. Novak, and M. Sienkiewicz, 2014: The value of dual-polarization radar in diagnosing the complex microphysical evolution of an intense snowband. *Bull. Amer. Meteor. Soc.*, doi:10.1175/BAMS-D-13-00258.1.

Rauber, R. M., and Coauthors, 2014: Stability and charging characteristics of the comma head region of continental winter cyclones. *J. Atmos. Sci.*, **71,** 1559–1582, doi:10.1175/JAS-D-13-0253.1.

Rogers, R. R., and M. K. Yau, 1989: *A Short Course in Cloud Physics.* 3rd ed. Butterworth-Heinemann, 290 pp.

Ryzhkov, A. V., 2007: The impact of beam broadening on the quality of radar polarimetric data. *J. Atmos. Oceanic Technol.*, **24,** 729–744, doi:10.1175/JTECH2003.1.

Ryzhkov, A. V., and D. S. Zrnić, 1995: Precipitation and attenuation measurements at a 10-cm wavelength. *J. Appl. Meteor.*, **34,** 2121–2134, doi:10.1175/1520-0450(1995)034,2120:PAAMAA.2.0.CO;2.

Ryzhkov, A. V., and D. S. Zrnić, 1998: Discrimination between rain and snow with a polarimetric radar. *J. Appl.Meteor.*, **37,** 1228–1240, doi:10.1175/1520-0450(1998)037,1228:DBRASW.2.0.CO;2.

Ryzhkov, A. V., and D. S. Zrnić, 2007: Depolarization in ice crystals and its effect on radar polarimetric measurements. *J. Atmos. Oceanic Technol.*, **24,** 1256–1267, doi:10.1175/JTECH2034.1.

Ryzhkov, A. V., and D. S. Zrnić, and B. A. Gordon, 1998: Polarimetric method for ice water content determination. *J. Appl. Meteor.*, **37,** 125–134, doi:10.1175/1520-0450(1998)037,0125:PMFIWC.2.0.CO;2.

Ryzhkov, A. V., S. E. Giangrande, and T. J. Schuur, 2005: Rainfall estimation with a polarimetric prototype of WSR-88D. *J. Appl. Meteor.*, **44,** 502–515, doi:10.1175/JAM2213.1.

Ryzhkov, A. V., H. Reeves, T. Schuur, M. Kumjian, and D. Zrnić, 2011: Investigations of polarimetric radar signatures in winter storms and their relation to aircraft icing and freezing rain. *35th Conf. on Radar Meteorology,* Pittsburgh, PA, Amer. Meteor. Soc., P13.197. [Available online at https://ams.confex.com/ams/35Radar/webprogram/Paper191245.html.]

Ryzhkov, A. V., M. Kumjian, S. Ganson, and P. Zhang, 2013: Polarimetric radar characteristics of melting hail. Part II: Practical implications. *J. Appl. Meteor. Climatol.*, **52,** 2871–2886, doi:10.1175/JAMC-D-13-074.1.

Ryzhkov, A. V., P. Zhang, H. D. Reeves, M. R. Kumjian, T. Tschallener, S. Tromel, and C. Simmer, 2016: Quasi-vertical profiles—A new way to look at polarimetric radar data. *J. Atmos. Oceanic Technol.,* **33,** 551–562, doi:10.1175/JTECH-D-15-0020.1.

Ryzhkov, A., P. Bukovcic, A. Murphy, P. Zhang, and G. McFarquhar, 2018: Ice microphysical retrievals using polarimetric radar data. *10th European Conference on Radar in Meteorology and Hydrology*, 1 – 6 July, The Netherlands, # 40. Available online at: projects.knmi.nl/erad2018/ERAD2018_extended_abstract_040.pdf.

Scharfenberg, K. A., D. J. Miller, T. J. Schuur, P. T. Schlatter, S. E. Giangrande, V. M. Melnikov, D. W. Burgess, D. L. Andra, M. P. Foster, and J. M. Krause, 2005: The joint polarization experiment: Polarimetric radar in forecasting and warning decision making. *Wea. Forecasting*, **20**, 775-788.

Schneebeli, M., and Berne, 2012: An extended Kalman filter framework for polarimetric X-band weather radar data processing. *J. Atmos. Oceanic Technol.*, **29,** 711-730.

Schrom, R. S., and M. R. Kumjian, 2016: Connecting microphysical processes in Colorado winter storms with vertical profiles of radar observations. *J. Appl. Meteor. Climatol.,* **55,** 1771–1787, doi:10.1175/JAMC-D-15-0338.1.

Schrom, R. S., M. R. Kumjian, and Y. Lu, 2015: Polarimetric radar signatures of dendritic growth zones within Colorado winter storms. *J. Appl. Meteor. Climatol.,* **54,** 2365–2388, doi:10.1175/JAMC-D-15-0004.1.

Schuur, T., J., P. Heinselman, K. Scharfenberg, A. Ryzhkov, D. Zrnić, V. Melnikov, and J. Krause, 2003: Overview of the Joint Polarization Experiment (JPOLE), Report of the National Severe Storms Laboratory, Norman, Oklahoma, 73069, 39 pp.

Schuur, T. J., H.-S. Park, A. V. Ryzhkov, and H. D. Reeves, 2012: Classification of precipitation types during transitional winter weather using the RUC model and polarimetric radar retrievals. *J. Appl. Meteor. And Climatol.,* **53**, 763-779.

Sheridan, L., J. Harrington, D. Lamb, and K. Sulia, 2009: Influence of ice crystal aspect ratio on the evolution of ice size spectra during vapor depositional growth. *J. Atmos. Sci.,* **66,** 3732–3743, doi:10.1175/2009JAS3113.1.

Sinclair, V., D. Moisseev, and A. von Lerber, 2016: How dual-polarization radar observations can be used to verify model representation of secondary ice. *J. Geophys. Res. Atmos.,* **121,** 10 954–10 970, doi:10.1002/2016JD025381.

Smith, T. L., S. G. Benjamin, J. M. Brown, S. Weygandt, T. Smirnova, and B. Schwartz, 2008: Convection forecasts from the hourly updated, 3-km High Resolution Rapid Refresh

(HRRR) model. *24th Conf. on Severe Local Storms*, Savannah, GA, Amer. Meteor. Soc., 11.1, https://ams.confex.com/ams/pdfpapers/142055.pdf.

Stewart, R. E., 1984: Deep isothermal layers within precipitation bands over southern Ontario. *J. Geophys. Res.*, **89,** 2567–2572, doi:10.1029/JD089iD02p02567.

Stewart, R. E., J. D. Marwitz, J. C. Pace, and R. E. Carbone, 1984: Characteristics through the melting layer of stratiform clouds. *J. Atmos. Sci.,* **41,** 3227–3237, doi:10.1175/1520-0469(1984)041,3227:CTTMLO.2.0.CO;2.

Stewart, R. E., 1992: Precipitation types in the transition region of winter storms. *Bull. Amer. Meteor. Soc.*, **73**, 287-296.

Straka, J. M., D. S. Zrnić, and A. V. Ryzhkov, 2000: Bulk hydrometeor classification and quantification using polarimetric radar data: Synthesis of relations. *J. Appl. Meteor.,* **39,** 1341–1372, doi:10.1175/1520-0450(2000)039,1341:BHCAQU.2.0.CO;2.

Szeto, K. K., C. A. Lin, and R. E. Stewart, 1988: Mesoscale circulations forced by melting snow. Part I: Basic simulations and dynamics. *J. Atmos. Sci.,* **45,** 1629–1641, doi:10.1175/1520-0469(1988)045,1629:MCFBMS.2.0.CO;2.

Tabary, P., Le Henaff, A., Vulpiani, G., Parent-du-Châtelet, J., Gourley, J.J., 2006: Melting layer characterization and identification with a C-band dual-polarization radar: a long-term analysis. In: Proceedings of 4th European Radar Conf., Barcelona, 18–22 September.

Tobin, D. M., and M. R., Kumjian, 2017: Polarimetric Radar and Surface-Based Precipitation-Type Observations of Ice Pellet to freezing rain transitions. *Wea. Forecasting,* **32,** 2065-2082.

Trömel, S., M. R. Kumjian, A. V. Ryzhkov, C. Simmer, and M. Diederich, 2013: Backscatter differential phase – Estimation and variability, *J. Appl. Meteor.,* **52**, 2529-2548.

Trömel, S., A. Ryzhkov, P. Zhang, and C. Simmer, 2014: Investigations of backscatter differential phase in the melting layer. *J. Appl. Meteor. Climatol.,* **53,** 2344–2359, doi:10.1175/JAMC-D-14-0050.1.

Trömel, S., A. Ryzhkov, B. Hickman, C. Simmer, 2017: Climatology of the vertical profiles of polarimetric radar variables at X band in stratiform clouds. Extended abstract, 38th Conference on Radar Meteorology, 28 August – 1 September 2017, Chicago, Illinois, USA, Amer. Meteor. Soc.,. [Available online at https://ams.confex.com/ams/38RADAR/webprogram/Paper320485.html].

Vivekanandan, J., V. N. Bringi, M. Hagen, and P. Meischner, 1994: Polarimetric radar studies of atmospheric ice particles. *IEEE Trans. Geosci. Remote Sens.*, **32,** 1–10, doi:10.1109/36.285183.

Vivekanandan, J., D. S. Zrnić, S. M. Ellis, R. Oye, A. V. Ryzhkov, and J. M. Straka, 1999: Cloud microphysics retrieval using S-band dual-polarization radar measurements. *Bull. Amer. Meteor. Soc.*, **80**, 381-388.

Wexler, R. R., J. R. Reed, and J. Honig, 1954: Atmospheric cooling by melting snow. *Bull. Amer. Meteor. Soc.*, **35,** 48–51.

Williams, E. R., D. Smalley, M. Donovan, R. Hallowell, M. Wolde, M. Bastian, A. Korolev, and R. Evaristo, 2013: Validation of NEXRAD radar differential reflectivity measurements in snowstorms with airborne microphysical measurements: Evidence for hexagonal flat plate crystals. *36th Conf. on Radar Meteorology*, Breckenridge, CO, Amer. Meteor. Soc., 15A.6, https://ams.confex.com/ams/36Radar/webprogram/Manuscript/Paper228791/Williams_36RADAR_15A6.pdf.

Williams, E. R., and Coauthors, 2015: Measurements of differential reflectivity in snowstorms and warm season stratiform systems. *J. Appl. Meteor. Climatol.*, **54,** 573–595, doi:10.1175/JAMC-D-14-0020.1.

Wolde, M., and G. Vali, 2001: Polarimetric signatures from ice crystals observed at 95 GHz in winter clouds. Part I: Dependence on crystal form. *J. Atmos. Sci.*, **58,** 828–841, doi:10.1175/1520-0469(2001)058,0828:PSFICO.2.0.CO;2.

Wolfensberger, D., Scipion, D., and Berne, A., 2015: Detection and characterization of the melting layer based on polarimetric radar scans, *Q. J .Roy. Meteor. Soc.*, **142**, 108–124.

Zrnić, D. S., 1987: Three-body scattering produces precipitation signature of special diagnostic value. *Radio Sci.*, **22,** 76–86, doi:10.1029/RS022i001p00076.

Zrnić, D. S., and A. V. Ryzhkov, 1999: Polarimetry for weather surveillance radars. *Bull. Amer. Meteor. Soc.*, **80,** 389–406, doi:10.1175/1520-0477(1999)080,0389:PFWSR.2.0.CO;2.

Zrnić, D. S., N. Balakrishnan, C. L. Ziegler, V. N. Bringi, K. Aydin, T. Matejka, 1993: Polarimetric signatures in the stratiform region of a mesoscale convective system. *J. Applied Meteor.*, **32,** 678-693.

Zrnić, D. S., G. Zhang, V. Melnikov, and J. Andric, 2010: Three-body scattering and hail size. *J. Appl. Meteor. Climatol.*, **49,** 687–700, doi:10.1175/2009JAMC2300.1.